Quantum transport in HgTe topological insulator nanostructures

Dissertation

zur Erlangung des Doktorgrades
der Naturwissenschaften (Dr. rer. nat.)
der Fakultät für Physik
der Universität Regensburg

vorgelegt von

Johannes Ziegler

aus Nürnberg

im Jahr 2018

Promotionsgesuch eingereicht am: 5.10.2018

Die Arbeit wurde angeleitet von: Prof. Dr. Dieter Weiss

Prüfungsausschuss: Vorsitzender: Prof. Dr. K. Richter
1. Gutachter: Prof. Dr. D. Weiss
2. Gutachter: Prof. Dr. D. Bougeard
weiterer Prüfer: Prof. Dr. S. D. Ganichev

Contents

1 Introduction

The search for stable and controllable quantum states for use in quantum computing has been a long standing problem. Popular systems that have been and are still being investigated for such states, called qubits, are single atom ion traps [1] or nitrogen vacancies in diamonds [2], spin-qubits in quantum points [3] and superconducting qubits in superconducting quantum interference devices (SQUIDs) [4]. A crucial parameter for the stability of qubits is the decoherence time of the quantum states, i.e. how long a state can retain its phase information before being perturbed by external influences.

The discovery of materials with topologically non-trivial phases [5–7] in the last decades has brought further candidates into focus. The concept of topological phases, pioneered in 1973 by Kosterlitz and Thouless [8], classifies systems that cannot be transformed into one another into distinct groups. Topological insulators (TIs) can lead to a novel type of qubits with topological protection against external perturbations, namely topological qubits. At the root of this effort is the search for Majorana quasi-particles, which are predicted to exist in a number of semiconductor/superconductor systems [9–11]. A feature of Majoranas is that they are their own anti-particle, which means they must have zero energy [12, 13]. A pair of such Majorana zero modes, each localized with spatial separation from the other, is expected to have unusually long decoherence times [14–16]. Signatures have been found in ferromagnetic atomic chains [17], TI-based Josephson junctions [18], and spin-orbit coupled nanowires [19], among others. Another system where they are predicted to exist are topological nanowires with proximity-induced superconductivity [20].

Topological insulators were first verified experimentally in HgTe quantum wells [7, 21]. The unique properties of TIs manifest as protected boundary states with Dirac-like dispersion — one-dimensional edge channels in two-dimensional topological insulators (2DTI) made from inverted HgTe quantum wells [22] and two-dimensional surface states in three-dimensional topological insulators (3DTI) from strained HgTe thin films [23]. In both cases, the topological states exist around an insulating bulk and feature spin-momentum locking, where the spin of the electron has a fixed relation with its direction of movement. This results in

reduced backscattering. In this thesis, ultra-low temperature studies of the properties of topological states (TSS) in 2D and 3DTIs via transport experiments in magnetic fields are reported.

Based on previous works on the quantum Hall effect (QHE) in strained HgTe [24, 25], the surface states in macroscopic devices, produced with an optimized wet-chemical etching process, are studied. The transition to nanostructures is then conducted utilising Aharonov-Bohm (AB) rings and antidot superlattices. The Aharonov-Bohm ring in strained HgTe is studied in low- and high-field regimes and gives insight into the viability of studying phase-coherent effects in strained HgTe. Antidot superlattices in HgTe quantum wells are probed for signatures of the helical edge channels.

A central goal is to gain a better understanding of topological surface states in HgTe-based 3DTIs, especially topological nanowires. Research in recent years has confirmed surface transport in Bi_2Te_3, Bi_2Se_3, $(Bi_{1.33}Sb_{0.67})Se_3$, and dry-physically etched HgTe nanowires [26–29], with only Ref. [30] providing signatures of the topological origin in Bi_2Se_3 nanowires. The latter was achieved by probing protected modes at the Dirac point of the 1D subband structure. The location of the Dirac point in strained HgTe and many other TIs makes this impossible, so that a novel approach has to be found. This is achieved by comparing experimental data to a simple electrostatical model, which verifies the topological nature of the surface states and its preservation in gated nanowires. Experiments in out-of-plane field configurations and on nanowire ensembles investigate further aspects of the unique 1D band structure.

The thesis is structured in the following way:

- Chapter 1 lays out the motivation and structure of this thesis.
- Chapter 2 covers the concepts of topological invariants and topological insulators. The realization of 2D and 3D topological insulators from HgTe is explained.
- The theoretical basics of magnetotransport effects investigated in later chapters are introduced in Chapter 3. This includes the Hall and quantum Hall effects in two-dimensional electron and hole systems (2DES/2DHS). Relevant phenomena in mesoscopic systems are commensurate oscillations and quantum interference effects like Aharonov-Bohm and Aharonov-Alt'shuler-Spivak (AAS) oscillations. In the final section, the 1D band structure of topological nanowires and their transport properties are reviewed.
- In Chapter 4, the experimental methods are discussed. This includes the wafer material, an optimized wet-chemical etching process and the experimental cryostat and electronic setups.

- Chapter 5 covers experiments on macroscopic strained HgTe Hall bars. This includes a discussion of the QHE in strained HgTe in Sec. 5.1 and the description of coexisting n- and p-type Landau fans in Sec. 5.2.
- In Chapter 6, the results from a 3D Aharonov-Bohm ring and an antidot lattices in HgTe quantum wells are discussed.
- Chapter 7 discusses a variety of experiments with topological nanowires based on the 3DTI, strained HgTe. The phase coherence length l_ϕ is extracted to gain an understanding of the present transport regime. Magnetoconductance and subband-induced oscillations are investigated in Sec. 7.3 and 7.4 to prove the topological nature of surface states. The analysis requires quantitative comparison with a simple electrostatic model which is why a thorough discussion of possible errors follows in Sec. 7.5. The main results from theoretical investigations by R. Kozlovsky *et al.* [31], that were part of this collaborative effort, are summarized in Sec. 7.6. Further experiments on nanowire ensembles in Sec. 7.7 and single nanowires in out-of-plane magnetic field configurations in Sec. 7.8 shed additional light on this unique system. Finally, the attempts to show a quantized conductance in miniaturized nanowire constrictions are presented in Sec. 7.9.
- A summary of attained results is given in Chapter 8.

2

Topological insulators

Topological insulators are most prominently described as a material with an insulating bulk and conducting boundary states, which manifest as edge states in two or surface states in three dimensions. The origin of such states is found in the topologically non-trivial band structure with inverted s- and p-type bands. In this simple picture, the bands must cross at the interface between materials with non-trivial and trivial band ordering. The energy gap of the insulating bulk must therefore close and conducting states emerge at the edges of a TI. Although HgTe is a semimetal in its bulk form, it can be made into a two- or three-dimensional topological insulator.

This chapter will cover the classification and origin of topological boundary states in HgTe TIs. First, an introduction into the concept of topology in solid-state physics will be given by discussing the Chern invariant, and topological classification of systems with the $\mathbb{Z}_2$ invariant (Sec. 2.1). Then, the properties of bulk HgTe are presented, followed by a discussion of HgTe-based 2D and 3D topological insulators along with their respective edge and surface states (Sec. 2.2).

2.1 Topological invariants

Topological insulators are set apart from other materials by the non-trivial topology of their band structure. A classification into trivial and topological materials is based on topological invariants. The topic of topology in condensed-matter physics is too comprehensive to be described in detail in this work. The following sections are therefore only a summary of the main concept. For comprehensive material on the matter, see textbooks by S.-Q. Shen [32] or M. Franz and L. W. Molenkamp [33].

2.1.1 Berry's phase and Chern invariant

Electronic states of solid-state systems are described by Bloch waves $\Psi_{n,\boldsymbol{k}}(\boldsymbol{r}) = e^{\mathrm{i}\boldsymbol{k}\boldsymbol{r}}|u_{n,\boldsymbol{k}}(\boldsymbol{r})\rangle$, which are the eigenfunctions of a translational invariant Hamiltonian $H(\boldsymbol{r})$. Here, $\boldsymbol{k}$ is the crystal momentum, $\boldsymbol{r}$ the spatial coordinate and $u_{n,\boldsymbol{k}}(\boldsymbol{r})$ are the energy eigenstates of the corresponding $\boldsymbol{k}$-dependent Hamiltonian $H(\boldsymbol{k})$ and carry information on the n-th energy band in k-space. The choice of the phase of an eigenstate $|u_{n,\boldsymbol{k}}\rangle$ is arbitrary. In most cases, only the relative phases are physically relevant. In quantum mechanics, the physical phase of such an eigenstate changes under adiabatic processes. The phase acquired from cyclical evolution of a parameter of the Hamiltonian is called the geometric phase, or Berry phase. It depends on the geometrical properties of the Bloch wave functions and is defined as

$$\gamma_c = \int_S \Omega_n(\boldsymbol{k})\mathrm{d}^2\boldsymbol{k}, \tag{2.1}$$

where $\boldsymbol{\Omega_n} = \nabla_{\boldsymbol{k}} \times i\langle u_{n,\boldsymbol{k}}|\nabla_{\boldsymbol{k}}|u_{n,\boldsymbol{k}}\rangle$ is the Berry curvature and S the surface enclosed by the closed loop ∂S in $\boldsymbol{k}$-space [34].

In the band theory of solid state systems, band structures with different topology can be classified by an invariant called the Chern number $c \in \mathbb{Z}$. The Chern number of the n-th band is defined as

$$c_n = \frac{1}{2\pi}\int_{\mathrm{BZ}} \Omega_n(\boldsymbol{k})\mathrm{d}^2\boldsymbol{k}, \tag{2.2}$$

where $\Omega_n(\boldsymbol{k})$ is the Berry curvature of the n-th band, which contains information on the geometrical properties of the phase of the Bloch wave functions in k-space. An important property is that the integral is an integer multiple of 2π, so that c_n becomes an integer. The total Chern number c of a system is given by the sum over all bands

$$c = \sum_{n=1}^{N} c_n. \tag{2.3}$$

The Chern number c of a Hamiltonian is invariant under any smooth transformations applied to the Hamiltonian where the energy gap is not closed. Systems with topologically distinct Hamiltonians cannot be smoothly transformed into one another. Typically a transition — such as closing the gap — is required.

An example of a Chern number in a real world system is the filling factor ν in the Quantum Hall effect (QHE). Discovered in 1980 by K. von Klitzing *et al.* [35], the QHE occurs when a 2DES (or 2DHS) is subjected to a strong magnetic field perpendicular to its plane. Under these conditions, the Hall conductance σ_{xy} quantizes and is given by integer multiples of e^2/h, where e is the elementary charge and h Planck's constant. In the context of Chern numbers, σ_{xy} can be

written as the integral of the Berry curvature Ω_{k_x,k_y} over the full Brillouin zone BZ [36]:

$$\sigma_{xy} = \frac{e^2}{\hbar} \int_{BZ} \frac{\mathrm{d}^2\boldsymbol{k}}{(2\pi)^2} \Omega_{k_x,k_y} = \nu \frac{e^2}{h}. \tag{2.4}$$

This means that the filling factor ν is equal to the Chern number and that each quantized plateau represents a distinct topological phase.

The QHE will be discussed in more detail in Sec. 3.1, however one of its main features is that current is carried by edge states, which follow the border of the sample in one direction. Such states are called chiral. The existence of these states at the interface between two gapped systems with different topological invariants is a fundamental consequence of their topological classification. And for each transition between topologically distinct systems, an edge state must exist.

2.1.2 $\mathbb{Z}_2$ invariant and bulk boundary correspondence

The topological states in the QHE are only accessible at large magnetic fields when time-reversal symmetry is broken. Topologically non-trivial states were presumed to exist only under large fields up until the prediction of a quantized Hall state in the absence of an external magnetic field on a graphene-like lattice by Haldane [37] in 1988. The discovery of graphene by Geim *et al.* in 2004 [38] led to further work by C. Kane and E. Mele [5, 6], who predicted the quantum spin Hall effect (QSHE) in a graphene model and classified this 2D time-reversal symmetric system with a topological invariant ν, called the $\mathbb{Z}_2$ invariant.

The key to understanding the $\mathbb{Z}_2$ invariant and topologically protected states is the time reversal symmetry. In quantum mechanics, time reversal symmetry is represented as an anti-unitary operator Θ. For spin-$1/2$ particles it has the property $\Theta^2 = -1$ [39]. This crucially entails the Kramer's theorem, which states that all eigenstates of a time-reversal symmetric Hamiltonian are two-fold degenerate. In the absence of spin-orbit interaction, the required degeneracy is simply the spin-degeneracy. In systems with spin-orbit interaction, Kramer states have to fulfil the condition $\Theta|k,\uparrow\rangle = |-k,\downarrow\rangle$. The resulting states are called helical. Helical states with equal spin direction move in the same direction and states with opposite spin move in opposite directions, often referred to as spin-momentum locking. Another important property of these states is that backscattering between them is only possible with scattering processes that flip the spin. Otherwise transport is non-dissipative.

The $\mathbb{Z}_2$-invariant ν can take one of two possible values, 0 or 1. In other words a time-reversal symmetric Hamiltonian can fall into one of two different topological

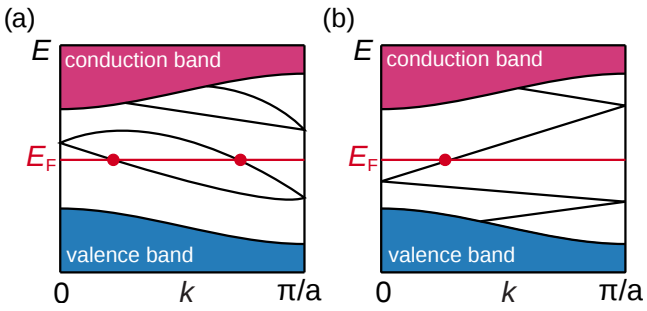

Figure 2.1: Schematic band structures with two Kramer's degenerate points at $k = 0$ and π/a for (a) even and (b) odd number of surface states crossing the Fermi energy E_F (adapted from [23, 40]). An odd number leads to topologically protected boundary states.

phases. This can be understood with the help of the following argument [40]. Figure 2.1 shows two different schematic band structures of time reversal invariant insulators as a function of k. Only half of the Brillouin zone is shown, because time reversal symmetry requires the other half to be an identical mirror image. The bulk conduction and valence bands are shown as red and blue shaded areas. In the gap, a Θ-invariant Hamiltonian may have boundary states, shown here as black lines. Kramer's theorem requires states at time reversal symmetric k-points ($k = 0$ and π/a) to be degenerate. Away from these high-symmetry points, spin-orbit interaction splits the spin-degeneracy. The bands connecting the degenerate points can be arranged in two different ways. They can connect pairwise [Fig. 2.1(a)], in which case an even number of states exist at the Fermi energy E_F at all times. The states can be pushed out of the gap by smooth transformations, so that there are no longer any boundary states and the system is topologically trivial. This situation is characterized by $\nu = 0$. In the second case, shown in Fig. 2.1(b), the Θ invariant k-points are still degenerate, but there is always an odd number of intersections of boundary states with the Fermi energy E_F. The boundary states can no longer be pushed out of the gap. In other words, time reversal symmetry protects the band crossing from being gapped. The system is therefore characterized as non-trivial with $\nu = 1$. Several, mathematically more rigorous methods to determine the $\mathbb{Z}_2$ invariant from the band structure exist. Detailed descriptions for the respective systems can be found in Refs. [6, 32, 33, 40].

For 3D systems, the above description can be expanded in an analogous way that results in a classification with four $\mathbb{Z}_2$ invariants $(\nu_0; \nu_1, \nu_2, \nu_3)$ [23, 41]. A detailed discussion is found in Ref. [39]. The symmetric Kramer's points become 2D Dirac points and the invariants are again defined by the number of such points enclosed by the Fermi surface. The invariants are zero, i.e. trivial, for an even number and topological for an odd number. A distinction is made between weak and strong topological insulators, where $\nu_0 = 0$ with any other non-zero invariant defines a weak topological insulator. Such a system can be regarded as a stack of multiple 2D topological insulators with boundary states, which are not robust against disorder [32]. Strong topological insulators are defined by $\nu_0 = 1$ and have

topologically-protected metallic surface states. Their properties will be discussed in more detail in Sec. 2.2.2.

In a simpler picture, the boundary states can be explained as a consequence of the inverted band order, that is a characteristic feature of TIs. Conventional semiconductors have a band order where the s-type conduction band (CB) lies above the p-type valence band (VB). This order is reversed in TIs. The gap needs to close at the interface for a smooth connection of the bands. Consequently, there are always states present at the interface between a topologically non-trivial and a trivial material. This is called the bulk-boundary correspondence. The next chapter will discuss how band inversion comes about in HgTe and what properties the boundary states have.

2.2 Properties of HgTe-based topological insulators

In its bulk form, the material HgTe is a semimetal with a Zincblende structure and a lattice constant of $a = 0.646\,\mathrm{nm}$. It is intrinsically p-doped due to Hg vacancies, but can be doped with In, or Ga (for n-doping) and Zn, or Cu (for p-doping) [42]. The bonds in HgTe are relatively weak, which result in a low hardness compared to III-V semiconductors, like GaAs. and make its surface prone to scratching. This also imposes a temperature limit for fabrication processes, which will be discussed in Cha. 4.

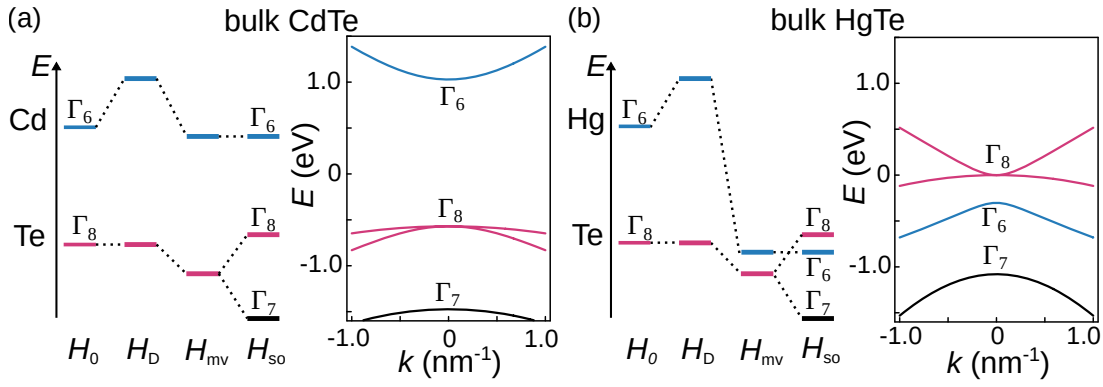

Figure 2.2: Band structure of CdTe and HgTe. (a) Schematic illustration of energy corrections from Darwin (H_D), mass-velocity (H_mv) and spin-orbit terms (H_so) to the Γ_6- and Γ_8-bands (left, adapted from [43]) and the resulting band structure around the Γ-point for bulk CdTe (right, adapted from [22]). (b) The same is shown for bulk HgTe, where the strong correction in the mass-velocity and the spin-orbit terms, H_mv and H_so, result in an inverted band order of the Γ_6 and Γ_8 bands.

The high atomic mass of Hg leads to significant relativistic corrections to the energy levels. Figure 2.2 shows the corrections to the energy levels of the initial system H_0 and band structures around the Γ-point for (a) CdTe and (b) HgTe. While the Darwin term H_D, mass-velocity term H_{mv}, and spin-orbit H_{so} terms lead to some corrections for CdTe, the band ordering is not affected. The s-type Γ_6 band lies above the Γ_8 band in the corresponding band structure, as is the case for most semiconductors. The major difference in HgTe, shown in Fig. 2.2(b), is the large correction from the mass-velocity term H_{mv} to the Γ_6 band, which results in an inversion of the s-type Γ_6 and p-type Γ_8 bands [22]. To make the topological edge and surface states of 2D and 3D topological insulators[1] accessible to transport experiments, a band gap needs to be opened. This can be achieved by two methods: confinement and strain.

2.2.1 $Cd_xHg_{1-x}Te$/HgTe quantum wells

In $Cd_xHg_{1-x}Te$/HgTe quantum wells, the confinement to 2D induces a band gap, thus forming a 2DTI [22]. The confinement leads to the creation of subbands, which stem from the bulk Γ_8 and Γ_6 bands. The respectively lowest subbands are called E_1 and H_1. The size of the gap depends on the quantum well thickness d, as shown in Fig. 2.3. With decreasing quantum well thickness d, the E_1 band is shifted to higher energies while the H_1 band is shifted to lower energies. The

[1]The transition between 2D and 3D behaviour occurs at a HgTe layer thickness of roughly 20 nm [44].

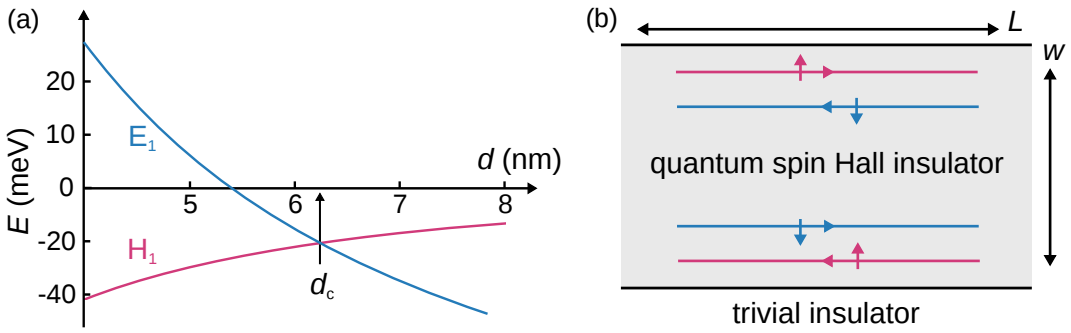

Figure 2.3: Band gap and quantum spin Hall effect in HgTe quantum wells. (a) The band gap is shown as a function of quantum well thickness d (adapted from [22]). The E_1 and H_1 subbands cross at d_c, resulting in inverted band structures for $d > d_c$ and non-inverted for $d < d_c$. Values from $d_c = 6.3$ to 6.6 nm have been reported in literature [7, 45, 46]. (b) Sketch of helical edge states in a quantum spin Hall insulator of width w and length L (adapted from [40]). States with opposite spin propagate in opposite directions on each edge. States with the same spin have opposite directions on opposite edges.

bands cross at a critical thickness d_c. The calculations show that for $d < d_c$ the inverted band ordering is lost and the trivial case is restored. The transition between topological and trivial systems is predicted to occur at $d_c = 6.3\,\text{nm}$ [22]. Inverted quantum wells ($d > d_c$) are quantum spin Hall (QSH) insulators and classified by a non-trivial $\mathbb{Z}_2$ invariant.

The QSH state is defined by two 1D helical modes per sample edge. The channels are spin-polarized, with opposite spin propagating in opposite directions [see Fig. 2.5(b)]. The states are topologically protected from backscattering off non-magnetic impurities due to spin-momentum locking, and as such each channel has a conductance of e^2/h. In an ideal system, the quantum spin Hall effect (QSHE) is characterized by a conductance of $G = 2\,e^2/h$ regardless of length or width [5]. This was first observed experimentally in Hall bars made from $Cd_xHg_{1-x}Te$/HgTe quantum wells [7] and later also in InAs/GaSb quantum wells [47].

2.2.2 Strained HgTe

In HgTe thin films, strain opens an energy gap and creates a 3D topological insulator [48, 49]. This is implemented experimentally by growing the HgTe layer on a CdTe substrate. CdTe has a lattice constant of $a = 0.648\,\text{nm}$. The resulting lattice mismatch between the two materials of 0.3 % leads to strain[2] in the HgTe thin film and causes a gap to open between the degenerate Γ_8 bands that stem from light hole (LH) and heavy hole (HH) bands of the trivial CdTe band structure. This allows access to topological surface states connecting the Γ_6 and Γ_8 bands. The size of the transport gap at the Γ-point is on the order of 15 to 20 meV [51, 52]. While the induced strain is expected to relax for a film thickness

[2]More specifically: tensile strain as the lattice constant of CdTe is larger. Compressive strain is expected to create a Weyl semimetal [50].

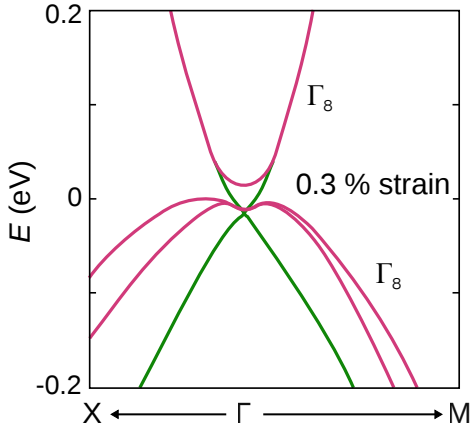

Figure 2.4: Sketch of the HgTe thin film band structure along the XΓ and ΓM directions for 0.3 % strain. (adapted from [53]). The strain induces a gap between the Γ_8 bands (red) and splits the degeneracy of the p-type bands. Inside the gap only topological surface states (green) are present. The Dirac point of the surface states is situated below the VB edge and therefore not accessible in transport measurements.

of 150 to 200 nm [54], it has been shown experimentally that 80 nm films are fully strained [55].

The strain opens a gap in the bulk Γ_8-bands and gives rise to surface states, shown in green in Fig. 2.4. The surface states are present throughout the band structure of strained HgTe, so that in the conduction band two species of electrons will coexist. Accordingly, Dirac electrons and bulk holes are present in the valence band. The surface states of such a 3DTI conductor can be regarded as an arrangement of connected 2DESs on the top, bottom and side surfaces. Depending on the Fermi energy position, the surface can also be a 2DHS and the bulk can be either insulating or conducting. A precise description is found in the supplementary of Ref. [25]. While the bulk states have the conventional quadratic dispersion relation and twofold spin-degeneracy, the properties of the surface states are unique as a result from their topologically non-trivial origin.

Figure 2.5(b) shows their linear energy dispersion relation and spin texture. This requires a description with the Dirac equation. Each point in the circular Fermi surface is occupied by a single spin. States with opposite momenta $\boldsymbol{k}$ and $-\boldsymbol{k}$ must have opposite spin, due to the requirements of time reversal symmetry discussed in Sec. 2.1.2. This is often referred to as spin-momentum locking. Consequently, the spin must rotate for a closed loop of the electron around the Fermi surface, which leads to a Berry phase of π [56, 57]. This non-trivial Berry phase has implications for magnetotransport effects, such as the quantum Hall effect or the Aharonov-Bohm effect in nanowires and will be discussed in the respective chapters.

It should be noted, that the dispersion relation of the topological surface states in strained HgTe is not purely linear, but has a small quadratic contribution that arises from the hybridization with bulk hole states. This can be seen from

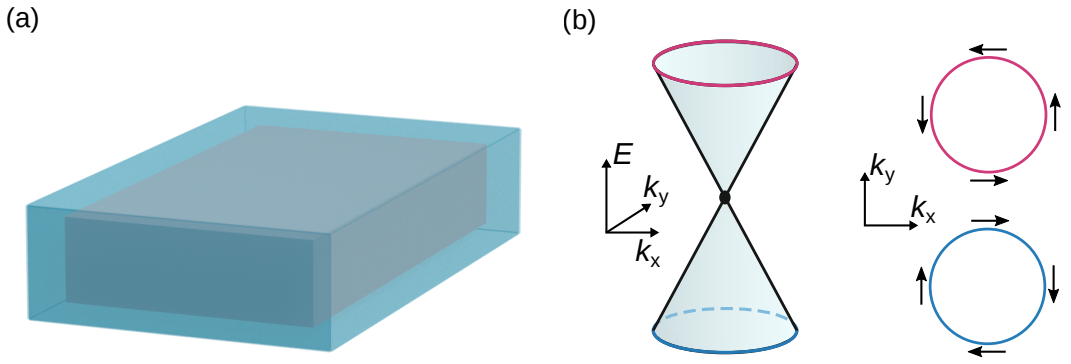

Figure 2.5: Topological surface states of a 3D topological insulator. (a) The surface states (blue) wrap around an insulating bulk (grey). (b) The surface states ideally have a linear dispersion in the form of a Dirac cone. The spin is locked to the momentum $\boldsymbol{k}$.

band structure calculations in Fig. 2.4 by Wu et al. [53] and in Ref. [55]. Similar properties are known from other 3DTIs, such as Bi_2Te_2Se [58, 59]. An accurate description requires a quadratic correction to the Dirac equation [32]. However, the parabolic component of the surface bands is expected to have only minor influences on the transport behaviour of the Dirac-like surface states. One example is a small perturbation to the Landau level energy spectrum of Dirac electrons discussed in Ref. [58].

3

Theoretical background

First experimental proof of a TI was obtained in transport measurements of the quantized conductance of a QSH insulator [7]. Numerous verifications of other TI systems followed via ARPES[1] experiments, compare Refs. [60–62]. Transport has nonetheless remained an important tool to probe topological states, e.g. in Refs. [24, 54, 63]. The fundamentals of relevant transport effects are discussed in this chapter. Magnetotransport in 2D systems is covered in Sec. 3.1, quantum interference effects in mesoscopic systems in Sec. 3.2, and the properties of devices with a 1D subband structure in Sec. 3.3. In the latter, special focus is given to the subband structure of topological nanowires as described in Ref. [64].

3.1 Magnetotransport in two dimensions

Two-dimensional electron gases have been extensively investigated in Si-MOSFET devices [65], high-mobility AlGaAs/GaAs heterostructures [66], and in recent years, in graphene [67]. In 2DTIs, the bulk states form a classical 2DES or 2DHS, while in 3DTIs the surface states have a Dirac-like dispersion. The fundamental transport effects, used to characterize 2D systems are described in this section for the electronic case.

3.1.1 Hall effect

Diffusive transport can be described by the Drude model [68], which considers the movement of non-interacting electrons accelerated by an electric field $\boldsymbol{E}$. Elastic and inelastic scattering processes with crystal atoms or impurities restore them to thermal equilibrium. When an external magnetic field $\boldsymbol{B}$ is applied perpendicular

[1] **A**ngular **r**esolved **p**hoto **e**mission **s**pectroscopy

to the 2DES plane, the Lorentz force leads to an additional component in the electric field so that Ohm's law needs to be written as

$$\boldsymbol{E} = \boldsymbol{\rho j} = \begin{pmatrix} \rho_{xx} & \rho_{xy} \\ \rho_{yx} & \rho_{yy} \end{pmatrix} \boldsymbol{j}, \tag{3.1}$$

with $\boldsymbol{\rho}$ the resistivity tensor and $\boldsymbol{j}$ the current density. Due to reasons of symmetry $\rho_{xx} = \rho_{yy}$ and $\rho_{xy} = -\rho_{yx}$. The equation of motion is given by

$$\frac{m^* \boldsymbol{v}_d}{\tau} = -e(\boldsymbol{E} + \boldsymbol{v_d} \times \boldsymbol{B}), \tag{3.2}$$

where m^* is the effective mass, $\boldsymbol{v}_d$ is the drift velocity, and τ the momentum relaxation time. Together with the relation $\boldsymbol{j} = en_s\boldsymbol{v}_d$, the components of $\boldsymbol{\rho}$ are

$$\rho_{xx} = \frac{m^*}{n_s e^2 \tau} = \frac{1}{e n_s \mu} \text{ and } \rho_{xy} = \frac{-B}{n_s e}. \tag{3.3}$$

Here, n_s is the charge carrier density, μ the electron mobility, and B the magnitude of the perpendicular magnetic field. From tensor inversion, the corresponding conductivities σ_{xx} and σ_{xy} follow as

$$\sigma_{xx} = \frac{\sigma}{1 + (\omega_c \tau)^2} \text{ and } \sigma_{xy} = \frac{\omega_c \tau \sigma}{1 + (\omega_c \tau)^2}, \tag{3.4}$$

where $\sigma = n_s e\tau/m^*$ is the Drude conductivity without a magnetic field and $\omega_c = eB/m^*$ the cyclotron frequency. The components of the resistivity are obtained experimentally by measuring longitudinal and transverse voltage drops in a Hall bar with uniform current flow:

$$\rho_{xx} = \rho_{yy} = \frac{U_{xx}}{I}\frac{W}{L} \text{ and } \rho_{xy} = R_{xy} = \frac{U_{xy}}{I}. \tag{3.5}$$

w and L are the width and length of the Hall bar. The Hall resistance R_{xy} is directly proportional to B and allows extraction of the charge carrier density n_s. The mobility μ can then be inferred from the charge carrier density n_s and the zero-field resistivity ρ_{xx}.

3.1.2 Landau quantization

In large magnetic fields, the Drude model is no longer appropriate. For magnetic fields where $\omega_c\tau > 1$, electrons perform multiple cyclotron orbits before being scattered, so that they interfere with themselves. The quantum mechanical treatment shows that the constant density of states of two-dimensional systems splits into Landau levels. The sequence of Landau levels depends on the dispersion relation of the charge carriers, with distinctly different energy spectra for conventional parabolic and linear bands.

Parabolic bands

The Hamiltonian for the Schrödinger problem of electrons in a parabolic band and an external magnetic field $\boldsymbol{B} = \nabla \times \boldsymbol{A}$ is given by

$$H = \frac{(\boldsymbol{p} + |e|\boldsymbol{A})^2}{2m^*} + V(z), \tag{3.6}$$

with momentum $\boldsymbol{p}$, vector potential $\boldsymbol{A}$ and the confinement potential $V(z)$. Detailed solutions of the problem can be found in Ref. [69] and other textbooks. The resulting energy spectrum of the system is given by

$$E_n^{\text{quadr}} = \hbar\omega_c \left(n + \frac{1}{2}\right), \tag{3.7}$$

where $n = 0, 1, 2, 3, ...$ is the Landau level index. The energy levels are equidistant with an energy spacing of $\hbar\omega_c$ [see Fig. 3.1] and the lowest Landau level has a finite energy of $E_0 = \hbar\omega_c/2$. Each Landau level is highly degenerate. The degeneracy is dependent on the magnetic field, such that the carrier density per Landau level is

$$n_{LL}(B) = g_s \frac{eB}{h}, \tag{3.8}$$

with the spin-degeneracy factor g_s. The filling factor $\nu = n_s/n_{LL}$ gives the number of filled Landau levels in the 2DES. Impurities in the 2DES can lead to a broadening of the ideally δ-peak shaped density of states and gives rise to extended and localized states. The impurities induce potential fluctuations that lift the degeneracy of the Landau levels. Further broadening occurs due to the finite temperature in experiments. At high magnetic fields, the Landau levels of spin-degenerate systems are split because of the Zeeman effect, which is given by an additional term $sg^*\mu_B B$. Here $s = \pm 1/2$ is the spin quantum number, g^* the Landé g-factor and μ_B the Bohr magneton. It should be noted that the Zeeman term is sensitive to the total applied magnetic field, while the Landau quantization depends on the field perpendicular to the 2DES plane. This needs

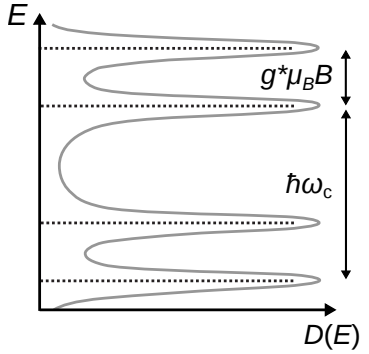

Figure 3.1: Density of states of Landau levels for a conventional 2DES (Fig. adapted from [69]). The levels have a constant energy separation of $\hbar\omega_c$. Zeeman splitting can lift the spin-degeneracy in large magnetic fields. Impurity effects can lead to a broadening of ideal δ-shaped peaks in the density of states.

to be considered when a magnetic field is applied not perpendicular to the sample plane.

Linear bands

In systems with linear dispersion, the massless fermions are described by the Dirac equation [56]. A detailed derivation can be found in Ref. [32]. The energy spectrum no longer consists of equidistant Landau level, but has a square root dependence on the magnetic field given by

$$E_n^{\text{lin}} = \text{sgn}\,(n) v_{\text{F}} \sqrt{2eB\hbar|n| + 1/2}, \tag{3.9}$$

where the Landau index is $n = 0, \pm 1, \pm 2, ..$ and v_{F} denotes the Fermi velocity. The level spacing is no longer equidistant, but has a square-root dependence. In contrast to conventional systems, Landau level energies of massless fermions can have negative Landau indices n. The level with index $n = 0$ has energy $E_{n=0} = 0$ and consists of both electrons and holes.

3.1.3 Integer quantum Hall effect

In experiments, the formation of Landau levels leads to quantized plateaus in the Hall resistance ρ_{xy} for large magnetic fields. This was first discovered in Si-MOSFET structures by von Klitzing *et al.* in 1980 [35]. Corresponding oscillations appear in the longitudinal magnetoresistance ρ_{xx} and are called Shubnikov-de Haas (SdH) oscillations [70]. The plateaus are quantized to

$$\rho_{xy} = \frac{1}{\nu}\frac{h}{e^2} = \frac{R_{\text{K}}}{\nu} \text{ or } \sigma_{xy} = \nu\frac{e^2}{h} \tag{3.10}$$

where $R_{\text{K}} = 25\,812.8074555(59)\,\Omega$ is the von Klitzing constant. The relation of filling factor ν and Landau index n depends on degeneracy factors, such as spin and valley. Furthermore, the quantization is completely independent of the material system and the width w and length L of the Hall bar. The minima of matching SdH oscillations appear precisely at the same magnetic field values as the quantized Hall plateaus. They are periodic in $1/B$ with the i-th plateau located at $B_i = n_s h/i|e|$, which allows the extraction of the charge carrier density n_s. Generally, the SdH oscillations appear below fully quantizing magnetic fields when the constant density of states begins to, but has not yet split into fully discrete Landau levels. At fields where the Hall plateaus are fully formed, the SdH minima approach zero resistance.

The quantized Hall and the zero resistance of the SdH minima can be explained with the edge channel picture. The confinement potential from the finite width

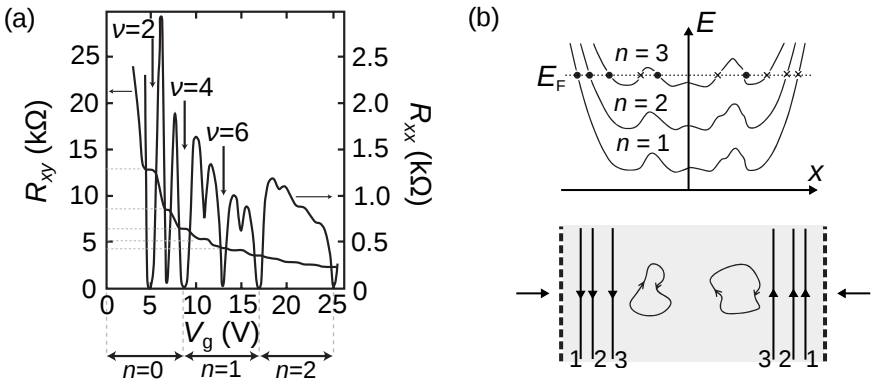

Figure 3.2: Integer quantum Hall effect. (a) The quantized Hall resistance R_{xy} with matching SdH oscillations in R_{xx} as reported by von Klitzing *et al.* in 1980 (adapted from [35]). (b) Landau levels are bent upwards at the sample edges (dashed lines) in the lower panel. Chiral 1D edge channels form at the intersection with the Fermi energy E_F. Potential fluctuations lead to localized states in the sample (adapted from [69]).

w of samples causes Landau levels to bend up towards higher energies, see Fig. 3.2(b). When the Fermi energy E_F is located in between two Landau levels, the points of intersecting Fermi energy E_F and Landau levels are the only conducting states. Transport is then carried by chiral 1D channels along the sample edge, which propagate in opposite directions on opposite edges. Spatial inhomogeneities can lead to localized states i in the sample centre [see Fig. 3.2(b)], which do not contribute to transport. The 1D channels carry the current without energy dissipation, as charge carriers can only scatter forward. Scattering between the edges is suppressed due to the spatial separation. The longitudinal resistance R_{xx} approaches zero. Consequently voltage probes on opposite sides are completely separated electronically, so that a Hall voltage builds up.

With a rising magnetic field strength, the LL spacing $\hbar\omega_c$ as well as the LL degeneracy n_{LL} increase, so that E_F moves through the energy levels. A periodic sequence of QH plateaus and SdH oscillations are the consequence. The effect can of course also be seen for a constant magnetic field and varying Fermi energy E_F. Figure 3.2(a) shows the original measurement from Ref. [35], where E_F was tuned via the topgate potential at a field of $B = 18\,\mathrm{T}$.

3.1.4 Surface quantum Hall effect

The square-root Landau level spectrum of Dirac electrons leads to a half-integer quantum Hall effect that is well-known from graphene [56]. Plateaus in the Hall conductance, along with corresponding Shubnikov-de Haas minima, occur at half-integer filling factors ν. The degeneracy factor of $g_s = 4$ in graphene (spin

degeneracy and valley degeneracy) leads to a Hall conductance of

$$\sigma_{xy} = \frac{4e^2}{h}\left(n + \frac{1}{2}\right). \tag{3.11}$$

In 3D topological insulators, the half-integer quantum Hall effect manifests differently and is referred to as the surface quantum Hall effect. The band structure of topological surface 2DESs only has a single Dirac cone of spin-resolved states per surface, so that the degeneracy factor is $g_s = 1$ and the filling factor and Hall conductance for a single surface are given by $\nu = n + 1/2$ and

$$\sigma_{xy} = \frac{e^2}{h}\left(n + \frac{1}{2}\right) \tag{3.12}$$

respectively. Transport experiments can always only probe the full system of 2DESs wrapped around the 3DTI. In a field configuration, where $\boldsymbol{B}$ points perpendicular to the sample plane, it pierces the top and bottom surfaces only. The total Hall conductance then becomes

$$\sigma_{xy}^{\mathrm{tot}} = \frac{e^2}{h}\left(n_{\mathrm{top}} + \frac{1}{2}\right) + \frac{e^2}{h}\left(n_{\mathrm{bot}} + \frac{1}{2}\right) = \frac{e^2}{h}\left(\nu_{top} + \nu_{bot}\right). \tag{3.13}$$

The total filling factor is given by $\nu = \nu_{top} + \nu_{bot}$. This leads to a sequence of odd integer Hall plateaus for a homogeneous charge carrier density throughout the system and has been observed in strained HgTe thin films [52,54] . In general, the filling factors of the top and bottom surfaces ν_{top} and ν_{bot} are independent of each other and depend only on the local Fermi energy position E_{F}. The sequence of Hall plateaus can therefore take all integer values. The underlying Dirac fermions are spin-resolved, so that the Landau levels do not split due to the Zeeman effect. The Dirac cone is only shifted up or down.

The ballistic edge channels can be visualized in a simple picture, as shown as a toy model in Fig. 3.3 for the case of filling factor $\nu = 1/2 + 3/2 = 2$. Top and bottom surfaces quantize, leaving chiral edge channels along the side surfaces. Detailed calculations by Zhang *et al.* [71] indeed place the wave functions of chiral edge channels on the side surfaces.

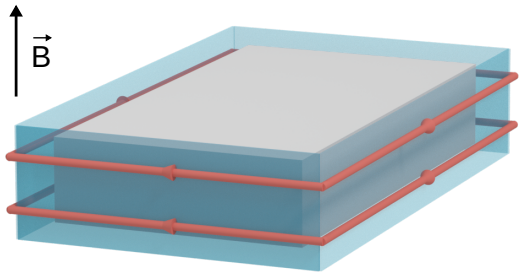

Figure 3.3: Schematic visualization of the half-integer QHE for a 3DTI in perpendicular magnetic field. Surface states (blue) on top and bottom surfaces quantize and lead to ballistic edge channels (red) propagating along on the 3DTI side surfaces. Bulk conduction (grey) depends on Fermi energy E_{F} position.

3.2 Mesoscopic transport

The experimental chapters of this work mainly cover mesoscopic devices in which quantum interference effects are a dominating part of the magnetoresistance. The following chapters will introduce the relevant effects. First, the characteristic lengths that are important for the classification and discussion of ballistic transport are reviewed. The semi-classical commensurable effects in 2D superlattices are quickly summarized in Sec. 3.2.2. And finally Sec. 3.2.3 will introduce quantum interference effects such as the Aharonov-Bohm and Aharonov-Alt'shuler-Spivak effects.

3.2.1 Characteristic lengths

The scales and quantities that characterize mesoscopic transport and are needed for later discussions will be introduced here. More detailed explanations can be found in literature, e.g. in Ref. [72]. The wave-like properties of electrons are described with the de Broglie-wavelength λ. In transport, electrons that carry the current are situated at the Fermi energy E_F, so that the relevant quantity is the Fermi wavelength given by $\lambda_\mathrm{F} = 2\pi/k_\mathrm{F}$. Here, the Fermi wave vector is defined as $k_\mathrm{F} = \sqrt{4\pi n_s/g_s}$. Size quantization in solid-state devices begins when device dimensions become comparable to λ_F. The Fermi wavelengths of electrons in semiconductor systems is on the order of some nanometers.

The elastic mean free path length l_e is defined as the average distance an electron travels between two large-angle elastic scattering events. The average length between two scattering events of arbitrary angles is called the quantum scattering length $l_\mathrm{q} = v_\mathrm{F}\tau_\mathrm{q}$, with the quantum scattering time τ_q. To account for momentum relaxation and accurately describe the resistivity, the scattering angle needs to be considered. This is done by weighting each scattering event with the scattering angle α. The resulting quantity is called the momentum relaxation or Drude scattering time τ. The elastic mean free path can then be given by $l_\mathrm{e} = v_\mathrm{F}\tau$. It can be extracted from experimentally accessible quantities by

$$l_\mathrm{e} = \frac{\hbar}{e}\mu\sqrt{4\pi n_s/g_s}. \tag{3.14}$$

Here, typical values for high-mobility 2DESs are on the order of several micrometers at low temperatures.

Elastic scattering events do not cause a randomisation of the phase of charge carriers. This only occurs in spin-flip events at magnetic impurities or in electron-phonon scattering events. It is therefore useful to introduce the dephasing time τ_ϕ for the discussion of transport effects that rely on the interference of electronic

wave functions. Again, there exists a corresponding phase coherence length l_ϕ, which describes the distance an electron travels before its phase is randomized by scattering events. In mesoscopic devices, transport is considered ballistic when the device size $L \leq l_e$ and phase-coherent when $L \leq l_\phi$.

3.2.2 Mesoscopic 2D superlattices

One and two dimensional superlattices in 2DESs such as GaAs have been investigated since the 1980s [73, 74]. The term mesoscopic superlattice stems from lattice periods a that are much larger than the crystal lattice periods, but comparable to mesoscopic quantities like the Fermi wavelength λ_F and the elastic mean free path l_e. In such nanostructures a whole array of effects can be observed depending on the type of superlattice and modulation. Here, we focus on modulated 2D antidot lattices as shown in Fig. 3.4(a), with periods $\lambda_\mathrm{F} < a < l_e$. This leads to commensurate oscillations in the longitudinal resistivity ρ_{xx} and phase coherent interference effects. Interference effects like the Aharonov-Alt'shuler-Spivak (AAS) oscillations are, however, much more easily observed in hexagonal superlattices and will be discussed in the next chapter.

The most prominent features of antidot superlattices are commensurate oscillations, shown in Fig. 3.4(b), which can be explained in a semi-classical pictures. One can imagine a set of discrete magnetic fields, where charge carriers follow cyclotron trajectories that fit inside the superlattice without scattering. These paths are called commensurate orbits. Charge carriers in such orbits are localized at an antidot, which acts as an artificial scatterer. When localized, electrons do not contribute to transport and the resistivity of the nanostructure increases. For

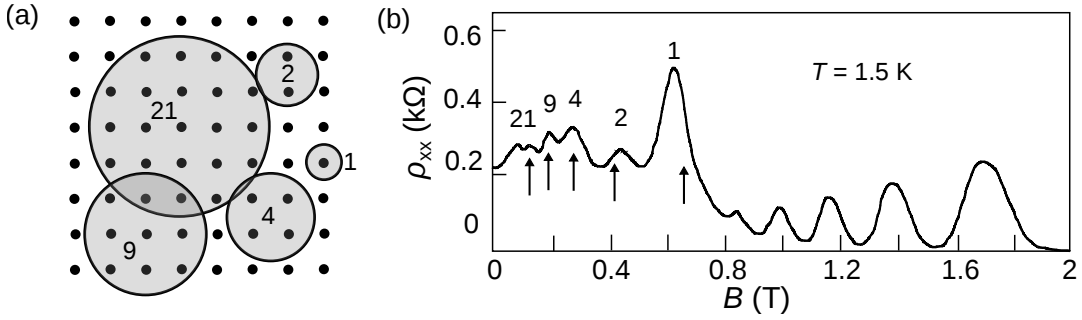

Figure 3.4: Commensurate oscillations in a 2D antidot superlattice. (a) Schematic square antidot lattice with possible orbits around 1, 2, 4, 9, and 21 antidots (adapted from [72]). (b) Peaks in the longitudinal resistivity ρ_{xx} of a modulated high-mobility GaAs 2DES are observed at magnetic fields B where cyclotron orbits match allowed paths in the antidot lattice. At fields $B > 0.8\,\mathrm{T}$ SdH oscillations appear (adapted from [74]).

non-commensurate magnetic fields, electrons are scattered by the antidot potentials. The relation between magnetic field B and cyclotron radius r_c is given by $B = \hbar k_\mathrm{F}/|e|r_c$, where e is the elementary charge. Permitted orbits solely depend on the geometry of the superlattice and the mean free path length l_e. The important quantities are the lattice period a and the antidot diameter d_AD. Cyclotron orbits around 1, 2, 4, 9, 21, ... antidots are possible in principle. However, for a specific sample allowed orbits will depend on the relation of a and d_AD of the antidot lattice. The median cyclotron radii $\bar{r}_c$ of possible orbits are: $\bar{r}_{c,1} = 0.5a$, $\bar{r}_{c,2} = 0.8a$, $\bar{r}_{c,4} = 1.14a$, $\bar{r}_{c,9} = 1.7a$ and $\bar{r}_{c,21} = 2.53a$ [74]. The peak associated with electron orbits around a single antidot is referred to as the fundamental peak, while orbits around multiple antidots are referred to as subharmonics. Higher order subharmonics are suppressed when the orbit circumference becomes larger than the mean free path length l_e. The decrease in resistivity for $B > B_{c,1}$ is caused by orbits with a diameter smaller than $a - d_\mathrm{AD}$. Charge carriers can then drift through the lattice of artificial scatterers unimpeded.

3.2.3 Quantum interference effects

Electrons in condensed-matter systems can show both particle and wave behaviour. An effect that can be described by particle behaviour was discussed in the previous section. Here, the quantum effects stemming from wave-like behaviour are discussed. The quantum properties of charge carriers begin to play a role when device dimensions are on the order of characteristic lengths, such as the elastic mean free path length l_e and the phase coherence length l_ϕ. Magnetic field-induced phase differences lead to constructive or destructive interference and manifest in the Aharonov-Bohm and Aharonov-Alt'shuler-Spivak effects, among others.

Aharonov-Bohm effect

Aharonov and Bohm predicted in 1959 [75], as well as previously Ehrenberg and Siday in 1949 [76], that the partial waves of a charged particle experience a phase shift, when their paths enclose a magnetic flux ϕ. This holds even when the particle waves follow paths where the electric and magnetic fields are zero. The discovery gave credence to the physical significance of the vector potential $\boldsymbol{A}$, which is connected to the magnetic field by $\boldsymbol{B} = \nabla \times \boldsymbol{A}$. Although initially predicted for free electrons in a vacuum, the effect also occurs in electron gases in semiconducting nanostructures [77, 78], most commonly in ring structures as shown in Fig. 3.5.

Two equivalent descriptions exist for the AB effect. The quantum mechanical picture of an electron on a circular orbit, defined by a potential $V(r)$ and an applied magnetic field $\boldsymbol{B}$, can be described by the following Hamiltonian:

$$H = \frac{1}{2m^*}\left(\boldsymbol{p} + e\boldsymbol{A}\right)^2 + V(r). \tag{3.15}$$

The solution can be obtained by rewriting into cylindrical coordinates and neglecting the radial terms [69,75]. The latter is possible due to the geometry with fixed radius r_0, shown in Fig. 3.5. The corresponding eigenenergies for a particle on a circular path $\boldsymbol{s}$ with in a magnetic field are given by

$$E_l = \frac{\hbar^2}{2m^* r_0^2}(l + \frac{\phi}{\phi_0})^2, \tag{3.16}$$

where m^* is the effective mass, $l \in \mathbb{Z}$ the angular momentum quantum number, and $\phi_0 = h/e = 4.135667862(26)\,10^{-15}\,\mathrm{Tm}^2$ the magnetic flux quantum [69]. The energy spectrum for each angular momentum l is quadratic with degenerate states for clockwise and counter-clockwise states. It shows that for each energy, solutions with $k_l = l + \phi/\phi_0$ and $-k_l$, i.e. electrons on clockwise and counter-clockwise paths, must exist. The ϕ_0-periodicity of the system can be seen from the ϕ/ϕ_0-term.

In the picture of particle-waves travelling through the ring structure [see Fig. 3.5(a)], the partial waves of an electron will pick up an additional phase if a magnetic field $\boldsymbol{B}$ is applied perpendicular to the device plane. In contrast to the original predictions in Refs. [75,76], the magnetic field is non-zero in the current path in semiconductor experiments. This is without consequence as the vector potential may be of arbitrary shape. Only the total magnetic flux ϕ passing through the loop is important. The Aharonov-Bohm phase φ_{AB} is given by

$$\varphi_{\mathrm{AB}} = -\frac{|e|}{\hbar}\oint \boldsymbol{A}\cdot \mathrm{d}\boldsymbol{s} = -\frac{|e|}{\hbar}\phi = -2\pi\frac{\phi}{\phi_0}, \tag{3.17}$$

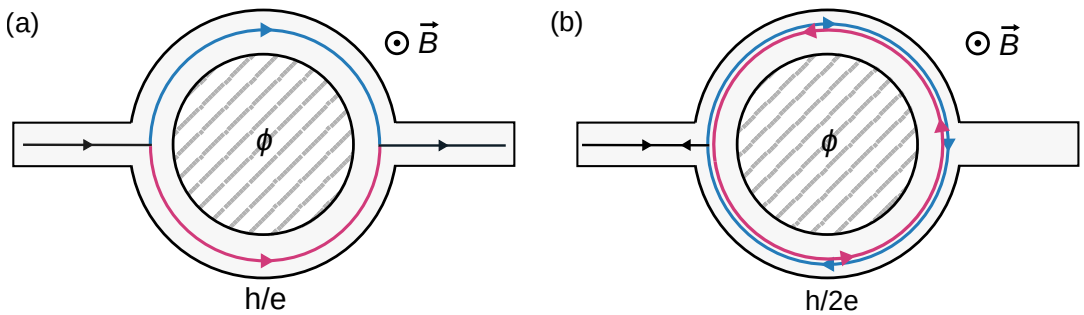

Figure 3.5: Sketch of an Aharonov-Bohm ring used to study interference effects in semiconductors (adapted from [72,79]). Trajectories of partial waves (a) for h/e- and (b) $h/2e$-periodic paths are shown. The paths enclose a magnetic flux ϕ marked by the hatched area.

where $\boldsymbol{s}$ is the circular trajectory [69]. In a homogeneous magnetic field perpendicular to the loop's plane, the magnetic flux is given by

$$\phi = BA, \tag{3.18}$$

where B is the magnitude of the magnetic field and A the area enclosed by the current loop. For both pictures, the connection to the conductance can be seen by taking a look at the transmission probability for an electron passing through the ring. Partial waves of the quantum mechanical particle will have transmission coefficients of t_1 for the top and t_2 for the bottom arm. They are given by:

$$t_1 = a_1 e^{\mathrm{i}\varphi_{\mathrm{AB}}/2} \text{ and } t_2 = a_2 e^{-\mathrm{i}\varphi_{\mathrm{AB}}/2}. \tag{3.19}$$

Here, a_1, a_2 are amplitudes, and $\varphi_{\mathrm{AB}}/2$ is the phase each partial wave picks up while passing the respective ring segment. In quantum mechanics, the total transmission T of two interfering waves is given by

$$T = |t_1 + t_2|^2 = a_1^2 + a_2^2 + 2a_1 a_2 \cos\varphi_{\mathrm{AB}}. \tag{3.20}$$

The terms $a_1^2 + a_2^2$ can be interpreted as the classical transmission probability. The third term comes from the quantum interference and is missing in the classical limit. The total phase difference is given by the AB phase φ_{AB}, so that an oscillating conductance with period $\Delta B = \phi_0/A$ follows from the transmission.

The first experimental observations of h/e-periodic signals in condensed matter systems occurred in a single metallic Au-ring [80] and semiconductor rings [81, 82]. Previously, Sharvin and Sharvin had already observed $h/2e$-periodic oscillations in metallic cylinders [83]. Such higher order oscillations, called Aharonov-Alt'shuler-Spivak oscillations, have a different origin.

Aharonov-Alt'shuler-Spivak effect

In the diffusive regime, where l_ϕ is smaller than the device dimensions other mechanisms play a role. Here, the partial waves follow closed time-reversed paths in clockwise and counter-clockwise direction and interfere at the starting point as shown in Fig. 3.5(b). This means they follow identical paths, which results in the same phase difference for both partial waves. The interference is constructive, which corresponds to enhanced backscattering and leads to a conductance minimum at $B = 0$. The partial waves loop around the entire ring and therefore enclose twice the magnetic flux ϕ. The magnetoconductance becomes $h/2e$-periodic. Such oscillations are called Aharonov-Alt'shuler-Spivak oscillations. Another manifestation of the same principal of interfering clockwise and counter-clockwise paths is weak anti-localization [84]. It occurs for closed paths along randomly distributed scatterers instead of a lithographically defined

current path. Impurities and defects are distributed randomly so that areas of enclosed flux are also distributed randomly and only limited by the phase coherence length l_ϕ. This leads to a positive magnetoresistance, as an increasing magnetic flux through the loops destroy the negative interference conditions.

Ensemble averaging

In ensembles of n diffusive or quasi-ballistic rings connected in series or parallel, h/e-periodic oscillations are suppressed while $h/2e$-periodic oscillations are unaffected [69, 85]. This can be understood by comparing the coherence length l_ϕ to the size of the ensemble. In the case of a few rings n, the total array size will quickly outgrow l_ϕ. In other words, the closed electron trajectories for single elements in the array are coherent in themselves, but not with each other. For the AB effect, the phase at $\phi = 0$ is distributed randomly for eversy ring, so that contributions from different elements in an ensemble will average out. The amplitude of h/e-periodic oscillations diminish with increasing ensemble size n, following an $n^{-1/2}$-law [85,86]. As mentioned above, the phase of AAS oscillations at $\phi = 0$ is fixed due to identical time-reversed paths for each partial wave. Consequently, the contributions from different parts of the ensemble do not cancel out. The amplitude of $h/2e$-oscillations is therefore independent of the ensemble size.

3.3 Transport in one dimension

A large part of experiments in this thesis focuses on topological nanowires and their unique flux-dependent 1D band structure under in-plane magnetic fields. The theoretical description of the Aharonov-Bohm oscillations in this system differs from theory in Sec. 3.2.3, which is why the theoretical fundamentals of the system as well as experimentally detectable signatures are discussed in Sec. 3.3.1. The basic properties of quantum point contacts are summarized in Sec. 3.3.2.

3.3.1 Topological nanowires

A nanowire made from a 3D topological insulator can be viewed as a hollow conducting cylinder with metallic surface states. A sketch of a TI nanowire with a square cross section A is shown in Fig. 3.6(a). A magnetic field B applied along the nanowire axis will lead to periodic magnetoconductance oscillations. Diffusive transport will lead to $h/2e$-periodic oscillations, analogous to early experiments

in diffusive metal cylinders by Sharvin and Sharvin [83]. When transport becomes ballistic, h/e-periodic conductance oscillations are expected. The physical fundamentals for this behaviour are discussed in the following.

In an idealized model, the Dirac-like spin-resolved surface states of a topological nanowire are wrapped on a cylindrical surface as in a carbon nanotube [87–90]. The band structure, and observable effects, are similar. However, a decisive difference between carbon nanotubes and TI nanowires is the presence of a Berry phase in the latter. The consequences were first reported in Ref. [64]. The Dirac cone dispersion of the 2D topological surface states is split into subbands by the 1D confinement, as seen in Fig. 3.6(b). This is described by a Dirac Hamiltonian $H = v_\mathrm{F}\boldsymbol{p} \cdot \boldsymbol{\sigma}$ with an anti-periodic boundary condition for the wave functions Ψ [64]:

$$\Psi(z, s + P) = e^{i2\pi(\phi/\phi_0 + 1/2)}\Psi(z, s). \tag{3.21}$$

Here $\boldsymbol{\sigma}$ are the Pauli matrices, z is the coordinate along the nanowire axis, s the coordinate along the circumference and P the circumference. ϕ/ϕ_0 is the magnetic flux through the wire cross section A, in units of the magnetic flux quantum. The constant shift of $1/2$ stems from the Berry phase present in topological insulators. A spin-$1/2$ particle will rotate by an angle of 2π during an orbit around the perimeter of the wire. The boundary condition therefore needs to be anti-periodic due to the 4π-periodicity of spin. The resulting band structure, shown for three cases in Fig. 3.6(b), is flux-dependent due to the boundary condition. For $\phi/\phi_0 = 0$, the 1D subband structure is gapped with angular momentum degenerate subbands. The total energy of the system is given by

$$E = \hbar v_\mathrm{F}\sqrt{k_z^2 + k_l^2}. \tag{3.22}$$

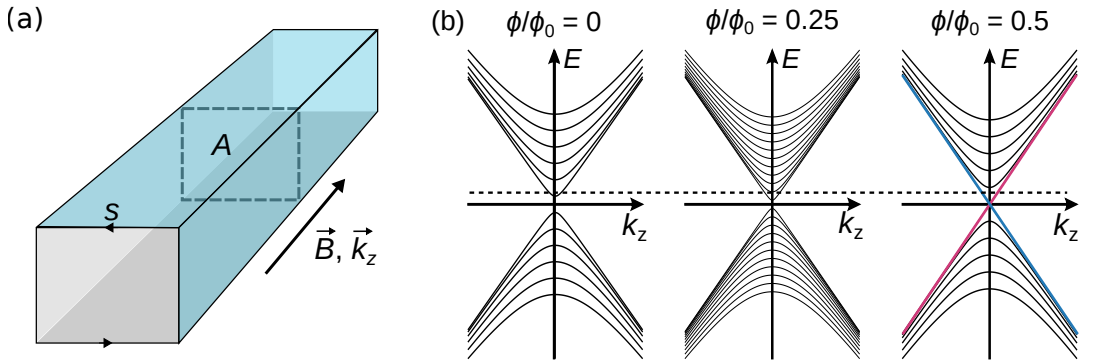

Figure 3.6: (a) Schematic nanowire with cross section A in an external magnetic field $\boldsymbol{B}$ along the nanowire axis. The coordinate s follows the nanowires circumference. (b) Band structure of a topological nanowire for magnetic fluxes of $\phi/\phi_0 = 0, 0.25$, and 0.5. The band structure is h/e-periodic with linear modes at $\phi/\phi_0 = 0.5$ (adapted from [31]).

While the parallel component along k_z simply follows the Dirac dispersion of the surface states due to the free motion of the particle, the component perpendicular to the wire's axis is given by

$$k_l = \Delta k_l \left(l + \frac{1}{2} - \frac{\phi}{\phi_0} \right). \tag{3.23}$$

Here, $\Delta k_l = 2\pi/P$ is the the subband spacing and the $l \in \mathbb{Z}$ angular momentum quantum number. At $\phi/\phi_0 = 0.25$, the angular momentum degenerate bands have split. One band from each pair moves up, the other down so that the gap at $E = 0$ begins to close. At $\phi/\phi_0 = 0.5$, the magnetic flux ϕ cancels the Berry phase contribution entirely. The subbands are again angular-momentum degenerate and the lowest n-type and highest p-type subbands form non-degenerate linear gapless modes. For $\phi/\phi_0 = 1$ and all integer multiples, the zero-field band structure is restored.

The expected experimental features can be understood by simply counting the number of modes. For a Fermi energy E_F near zero, i.e. in the subband gap, increasing the magnetic flux ϕ/ϕ_0 from 0 to 0.5 increases the number of modes by one. The behaviour is periodic in ϕ_0, resulting in periodic magnetoconductance oscillations with minima (maxima) at integer (half-integer) values ϕ/ϕ_0. The same behaviour occurs whenever E_F is located in a minigap between two subbands. For a slightly higher E_F, where a subband is opened [see dashed line Fig. 3.6(b)], the behaviour reverses. At zero flux, two modes contribute, while at $\phi/\phi_0 = 0.5$, only one crosses E_F. This leads to a phase shift in the oscillations. Maxima (minima) are now expected for integer (half-integer) multiples of the flux quantum ϕ_0. This means that in addition to ϕ_0-periodic magnetoconductance oscillations, subband-induced oscillations as a function of Fermi energy E_F with an anti-phase behaviour at integer and half-integer flux quanta are expected. Numerical simulations on such a system with varying degrees of disorder were carried out by Bardarson *et al.* [64]. Figure 3.7 shows the conductance G as a function of Fermi energy E_F for three values of a disorder parameter K_0. The traces

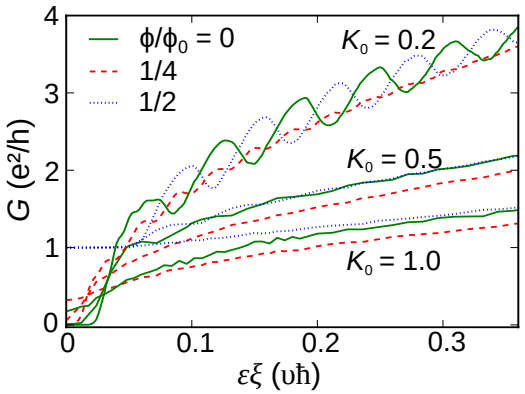

Figure 3.7: Conductance G versus Fermi energy $\epsilon\xi$ of an ideal topological nanowire for three strengths of disorder K_0 (adapted from [64]). A round cross section and homogeneous distribution of E_F is assumed.

for $K_0 = 0.2$ represent a ballistic system with little disorder, where the quantized conductance of $G = e^2/h$ from the perfectly transmitted linear modes at the Dirac point is preserved and the anti-phase subband oscillations are present. Both features are suppressed in the highly-disordered diffusive regime.

In systems were the Dirac point is located within the bulk gap, a quantized conductance of $G = e^2/h$ can be directly observed at $\phi/\phi_0 = 0.5$ due to a perfectly transmitting linear mode. This is a signature of the π-Berry phase and topological surface states and has been observed in $Bi_{1.33}Sb_{0.66}Te_3$ nanowires by Cho et al. [27]. In strained HgTe, the Dirac point is buried in the bulk VB, so that only subbands with higher angular momenta are present in the bulk gap.

When the elastic mean free path length l_e is shorter than the wire length L, transport in the nanowires becomes diffusive. Electrons scatter and paths are no longer coherent, so that the 1D band structure is no longer well defined. The h/e-contributions are suppressed. Instead, $h/2e$-periodic signals, caused by interfering time-reversed paths, dominate. This is analogous to the AAS effect and is simply another manifestation of the principle behind weak anti-localization [91]. The phase switching of AB oscillations with varying gate voltage V_g is not expected in this transport regime.

3.3.2 Quantum point contacts

Transport in a device with a 1D subband structure leads to a quantized conductance when transport is fully ballistic. Tuning the number of occupied subbands in the system, will lead to step-like conductance shown in Fig. 3.8. This was first observed by Wharam et al. [92] and van Wees et al. [93] in point contacts. In their experiments, a high-mobility GaAs/AlGaAs 2DES was constricted to a point contact by locally depleting it with a metallic split-gate [see inset of Fig. 3.8]. The width of the thin conducting region that remains can be controlled with the gate voltage. When transport is fully ballistic and transmission perfect, each subband contributes one conductance quantum so that the conductance is given by the number of occupied subbands N at the Fermi energy E_F [95]:

$$G_c = \frac{g_s e^2}{h} N, \tag{3.24}$$

In Fig. 3.8, a step-like conductance $G(V_\mathrm{g})$ with $2\,e^2/h$ at $B = 0$ is shown. The quantization to $2\,e^2/h$ stems from the spin-degenerate bands in conventional 2DESs. In a spin-resolved systems, such as the spin-helical surface states in 3DTI, a quantization of e^2/h is expected.

A typical effect in quantum point contacts (QPC) is that a small perpendicular magnetic field will stabilize the quantization of the constriction. This is attributed

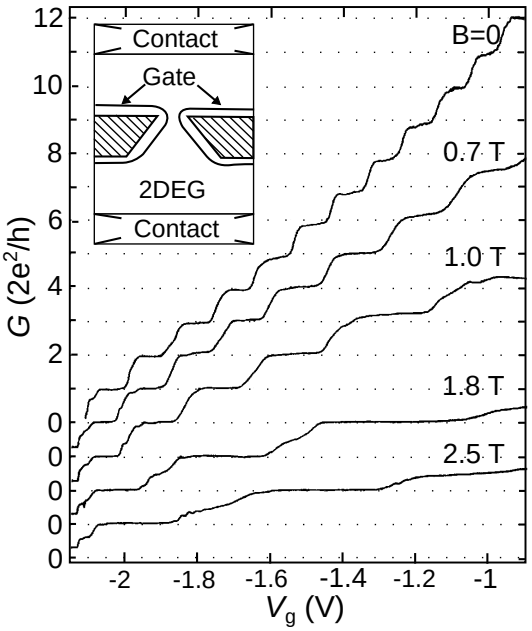

Figure 3.8: Conductance G of a GaAs/AlGaAs split-gate point contact as function of gate voltage for $T = 0.6\,\mathrm{K}$ and several magnetic fields (adapted from [94]). The spin-degenerate 1D subbands in this system lead to steps of $2\,e^2/h$. The inset shows a schematic layout of the design with the depletion region indicated around the split-gate (hatched areas).

to reduced backscattering near or in the QPC [94]. With increasing magnetic fields, the spacing between the 1D subbands becomes larger and with it the width of the conductance steps as seen in Fig. 3.8. At large fields, in the sense that $2r_c < w$ [96], the band structure features spin-split Landau levels. The conductance steps are then quantized to e^2/h.

Point contacts can be pinched off, e.g. by reducing the voltage of the split gate in GaAs/AlGaAs devices until the constriction is depleted entirely. This leads to a potential barrier in the constricted section, which can be overcome by large enough bias voltages. The current-voltage characteristics therefore become highly non-linear [97].

Detailed discussions of the effects introduced in this chapter, can be found in Refs. [69, 72, 98].

4

Experimental methods

The present chapter deals with the methods of nanofabrication and the experimental measurement setup. The material HgTe is prone to damage from mechanical sources, such as scratching, and exposure to high temperatures. These constraints are therefore required to be considered for all fabrication steps. The device fabrication techniques are standard procedures for semiconductor wafer processing in industry and the scientific nanofabrication community [99–102]. The following sections cover the basic concepts with special focus on the optimization of processes to temperature and size limits set by the material and size requirements. A full list of process parameters can be found in App. B.

4.1 Wafer material

Thin films of HgTe can be grown on GaAs or CdTe substrates, while the former are preferred for better availability and financial rationale. GaAs substrates with both (100) and (013) surface orientations are commonly used with a thick MBE-grown CdTe layer. This provides a defect-free virtual substrate for the $Cd_xHg_{1-x}Te$/HgTe heterostructures. Both capped and uncapped wafers of HgTe thin films are possible and have been investigated. Additional buffer and capping layers strongly enhance the quality of the material [51] and protect the top interface throughout fabrication processes. Capped wafers are therefore preferable for transport experiments that don't require interfacing with other materials such as ferromagnets or superconductors.

Most experiments in this work were carried out with devices (Hall bars, ring structures and nanowires) fabricated from capped 80 nm HgTe films. The wafers are prepared with a virtual 4 µm CdTe substrate on (013)-oriented GaAs. The 80 nm HgTe film is sandwiched by two 20 nm thick $Cd_{0.7}Hg_{0.3}Te$ buffer layers to reduce defects at the interfaces and improve the electron mobility μ in the HgTe film. An additional 40 nm CdTe layer acts as the capping layer, as shown in Fig. 4.1(a). Further experiments were carried out with topological nanowire devices built from strained HgTe on a (100)-oriented substrate with an identical

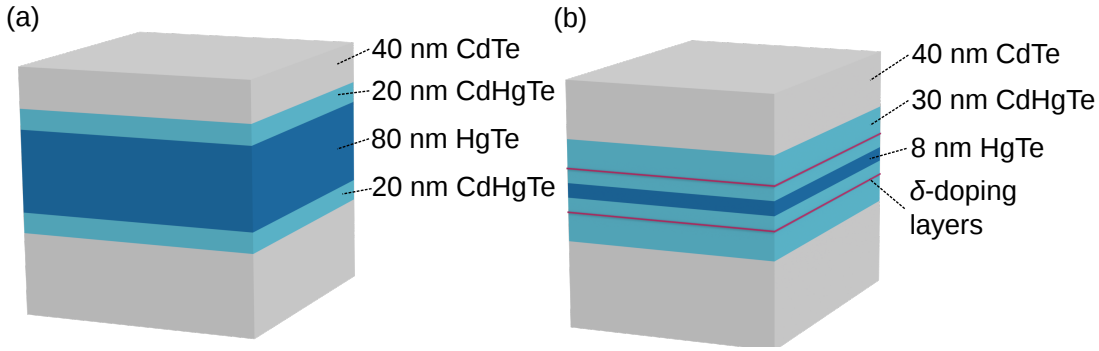

Figure 4.1: Sketches of CdTe/Cd_xHg_{1-x}Te/HgTe stacks grown on GaAs substrates (not shown). (a) For strained HgTe, a 4 µm thick CdTe is grown on (013)-oriented GaAs as a virtual substrate, followed by a $Cd_{0.7}Hg_{0.3}$Te buffer layer. The strained HgTe layer is shown in dark blue. The wafer is topped off by of another $Cd_{0.7}Hg_{0.3}$Te buffer layer and CdTe cap layer. Wafers with 80 and 50 nm HgTe thin films were investigated. (b) HgTe quantum wells are grown on a similar (013)-oriented virtual CdTe substrate. Buffer and cap layer thicknesses are typically 30 to 40 nm thick and include additional δ-doping layers. In this work, materials with quantum well thicknesses of $d = 5.7$ and 8 nm were investigated.

layer sequence. Results are presented in App. A.4. Point contact constrictions, discussed in Sec. 7.9, were fabricated from a wafer with a 50 nm HgTe thin film and otherwise identical stack.

Experiments in Sec. 6.2 investigate devices fabricated from CdTe/HgTe quantum wells with both inverted and trivial band-ordering. All inverted quantum well heterostructures were grown with the same layer sequence of an 8 nm HgTe layer in between two 30 nm CdHgTe buffer layers and a 40 nm CdTe cap layer. The non-inverted heterostructure consists of a 5.7 nm HgTe with 40 nm $Cd_{0.6}Hg_{0.4}$Te

Table 4.1: Details of 2DTI and 3DTI HgTe wafers.

wafer	HgTe (nm)	substrate orientation	CdHgTe buffers (nm)	CdTe cap (nm)	δ-doping
120227	80	(013)	20	40	-
140826	80	(013)	20	40	-
140827	80	(013)	20	40	-
170328	80	(100)	20	40	-
170713	50	(013)	20	40	-
101108	8	(013)	30	40	±10 nm
161027	8	(013)	30	40	±10 nm
170322	5.7	(013)	40	40	±10 nm

buffer layers above and below. The above quantum well heterostructures include symmetrical In-doping layers located 10 nm above and below the quantum well. All quantum wells were grown on (013)-oriented GaAs substrates. Details of all used wafers are listed in Table 4.1.

4.2 Sample fabrication

An essential part of sample preparation is the fabrication of mesas and nanostructures. This requires suitable lithographic processes, etch procedures, and a sample design that takes into account the limits of the respective techniques.

Lithography

All nanopatterned samples were built using both optical and electron beam lithography (EBL). They are based on the same concept: The chip is spin-coated with a resist, which is then exposed to either UV light or an electron beam. The long polymer chains of the resist are broken up into shorter pieces during exposure so that they become soluble in appropriate developers. In this manner, the sample can be covered selectively with resist for further steps such as etching or deposition of oxides and metals. These methods are standard procedures in semiconductor physics and are described in detail for example in Ref. [72].

Optical lithography was carried out with a *Carl Süss MBJ3* system. The process is resolution limited by the wavelength of UV light. Diffraction effects and fabrication limits of optical masks restrict the resolution, meaning that that optical lithography is only suitable for devices larger than roughly 1 µm. EBL processes have to be used for nanostructures. Here, a *Carl Zeiss Auriga* system came to use. The much smaller de Broglie wavelength of electrons means that resolution is limited by other effects such as scattering of electrons in the resist. Structure sizes down to 10 nm are however possible with appropriate etching methods. Another large advantage of EBL over optical lithography is its flexibility. While optical lithography requires a patterned chrome layer on a quartz glass mask, EBL masks are transferred to the resist by a computer controlled electron beam rasterizing across the chip. EBL masks can be flexibly modified from sample to sample with the only trade-off being sizeable time demands for larger structures, on the order of millimetres.

Wet chemical etching process

Previous experiments on strained HgTe thin films were carried out with dry-physically etched samples [29, 103]. The wafer is etched by bombarding it with accelerated heavy ions, which knock atoms from the crystal lattice. This naturally creates defects through heating and ion implantation, and significantly reduces electron mobilities μ. This effect is especially pronounced in nanostructures shown by experiments on HgTe nanowires by S. Weishäupl [29]. For this reason, a wet-chemical etching process was optimized in cooperation with H. Maier for use on HgTe thin films. Later on, more detailed investigations were carried out by M. Pleyer [104], which confirmed the previously determined recipe parameters.

Initial recipes for a solution based on Br_2 and ethylene glycol were adopted from previous work with $Cd_{1-x}Mn_xTe$ quantum wells by C. Betthausen [105, 106]. First tests with HgTe heterostructures showed promising results, however, etch rates were not uniform across the sample and too high for controlled etching depths. Uniformity was improved by using a sample holder where the chip is held perpendicular to the flow direction. The etch solution is assumed to flow over the sample surface more homogeneously. Further improvements to the etch rate could be realized by reducing the Br_2-concentration and lowering the temperature of the etching solution. Adding water to the solution improves the formation of smooth side walls, and reduces the amount of under-etching in the material. The final recipe, applied for all devices in this work, uses a solution of Br_2, ethylene glycol, and DI-water cooled to 0 °C, using a double-walled beaker and a closed circuit cooler. The solution is prepared with a ratio of 0.1 : 100 : 25.

Further tests on nanostructures and macroscopic Hall bars showed that etch pro-

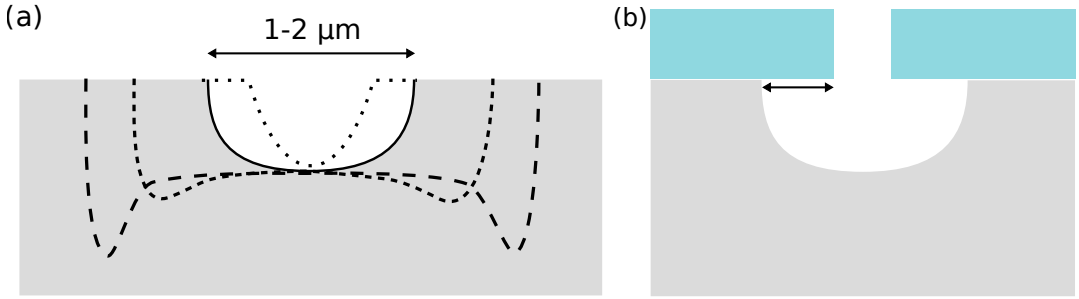

Figure 4.2: Behaviour of the Br_2-based wet etch process is sketched for (a) structures of different sizes and (b) under-etching of the resist (light blue). Structure width influences the side wall angle and the formation of trenches. (b) Visualization of under-etching, which becomes relevant in the fabrication of nanostructures and needs to be considered for the design of digital masks for EBL.

files vary with structure size, as shown schematically in Fig. 4.2(a). For very thin structures, the etching depth is controllable but sides are slanted (dotted line). For very wide structures, additional trenches are formed (dashed lines) while the etched side walls are nearly perpendicular. Such trenches are much deeper than the average etching depth. In a median regime with widths of about 1...2 µm, the side walls remain steep without the disadvantage of additional trenches (solid line). These findings were implemented by basing all nanostructure sample designs on lines of constant width. This choice allows predictable side walls and controllable etch rates throughout the entire nanopatterned section of a sample.

Another unavoidable consequence of wet-chemical etching is under-etching of the resist [see Fig. 4.2]. Due to the isotropic nature of the process, the resist is usually under-etched on the same scale as the total etching depth. The design of commonly used HgTe wafers requires etching to a minimum depth of 100...200 nm. The effect is therefore negligible in the fabrication of macroscopic devices with lengths of tens of micrometres. In nanowires or quantum point contacts this becomes a critical part of the sample design. Furthermore, it was found that under-etching is significantly increased for parts of the sample that are electrically connected to metallized contact pads. The precise mechanism is unknown at this point. The issue was avoided by soldering or metallizing contacts after the final etching step.

Sample design

With all advantages and disadvantages of the methods described above considered, samples are built by first defining a mesa with optical lithography and then etching wet-chemically. The mesa design, shown in Fig. 4.3(a), includes large contact pads to allow soldering of the indium contacts by hand. A mesa design from the A.V. Rzhanov Institute for Semiconductor Physics, Novosibirsk was modified to include two 10 µm long Hall bars to minimize serial resistance contributions from the macroscopic section in experiments with nanowire and point contact constrictions in the quasi-two point geometry. At a width of 50 µm, less than 0.2 squares are added to the signal of any constriction. Typical values for the square resistance in strained HgTe are on the order of 100 to 200 Ω and result in an extra serial resistance of 20 to 40 Ω to the signal. This contribution can be neglected in analysis in light of typical resistances of nanowires, which are on the order of kΩ.

In a second step, nanostructures are defined within a Hall bar [see Fig. 4.3(b)] using low-kV electron beam lithography to prevent unnecessarily high heating of the quantum well. The precise layout is chosen depending on the required type of measurement and structure.

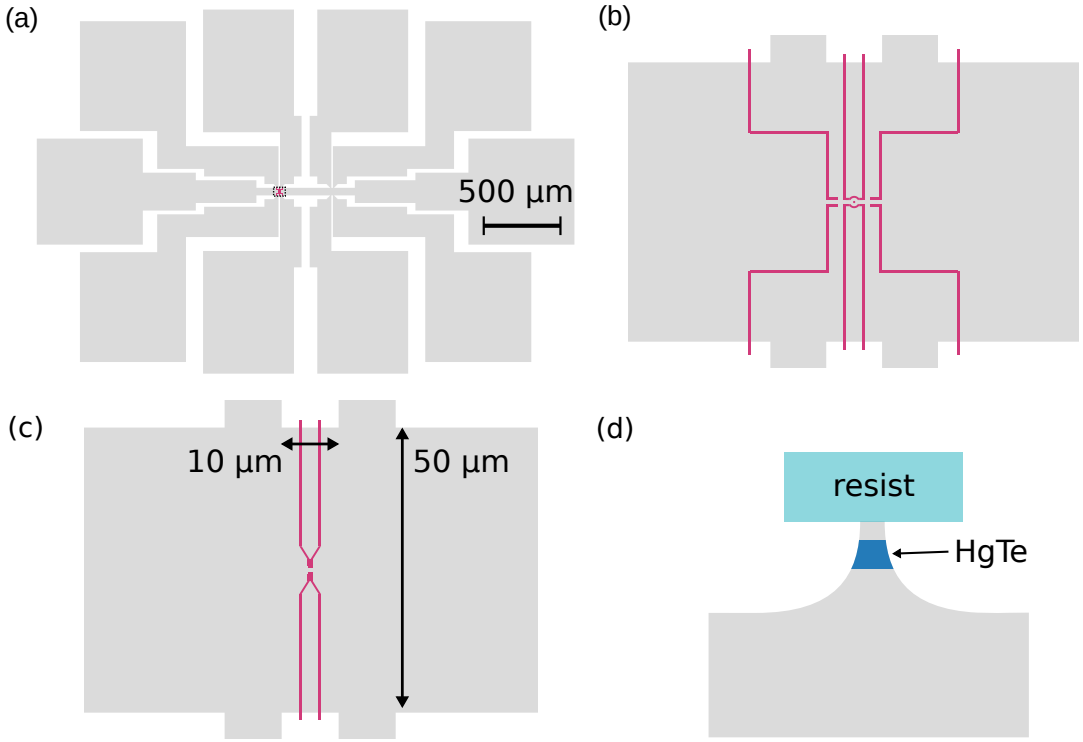

Figure 4.3: Typical design of nanostructured samples. (a) Design of the macroscopic Hall bar mesa that is transferred to the sample via optical lithography. A nanostructure can be written into the marked Hall bar using EBL. (b) Zoom of the black box in (a). Here, the example of an Aharonov-Bohm ring is shown. Other designs, such as the nanowire constriction in (c) are possible. All electronic masks use lines of constant width (red) to achieve a constant etch rate throughout the nanopatterned section. (d) Schematic view of the cross section of a nanowire/point contact constriction after wet-etching. The device width can be controlled with the resist width, while keeping etching parameters constant. For this, the unavoidable, but constant, under-etching from wet-chemical etching needs to be considered.

Nanofabrication

All nanostructures were etched in a design based on lines of constant width [see Fig. 4.3(b) and (c)], which produces trenches of predictable and constant etching depth. While there is a lower limit to the width of trenches that can be etched from the material, the size of the mesa between them is not limited in such a way. This makes the fabrication of very thin nanowires and even point contacts possible. Only their length is limited by the width of the etched trenches. The inevitable under-etching of the resist needs to be taken into account when designing the digital EBL mask for nanostructures. Tests have shown that the width of the remaining mesa w is approximately $w = w_{\mathrm{eLitho}} - 2d_{\mathrm{etch}}$, where w_{eLitho} is the width of the structure as drawn in the electronic mask and d_{etch} the depth of the etched

trenches. This can be attributed to the isotropic wet-chemical process, which also leads to inevitable rounding of the structures. Areas drawn with right angles end up with round corners. The radius of the curvature is roughly d_{etch}. The etched sides behave in the same way. Representative SEM-micrographs (scanning electron microscopy) of the nanostructures are shown at the beginning of the respective chapters about Aharonov-Bohm rings (Sec. 6.1), antidot superlattices (Sec. 6.2), nanowires (Sec. 7.1) and point contact constrictions (Sec. 7.9).

4.3 Topgate stack

Experiments with topological insulators tend to preferentially probe the bulk gap, where surface or edge states are the only conducting states. However, most wafers are either intrinsically n- or p-doped. This makes the usage of topgate electrodes necessary. By applying a voltage, the number of charge carriers in the conducting thin film can be adjusted in the same way as in a field effect transistor. This allows tuning the Fermi energy E_{F} through the bulk gap and into the conduction band in intrinsically p-doped 3D topological insulators. Similarly, n-doped 2D quantum wells can be tuned through the bulk gap into the valence band.

Oxides

The insulating properties of the CdTe cap layer are not sufficient, so that additional oxides need to be deposited. A combination of SiO_2 and Al_2O_3 has become the dielectric stack of choice during this work. The SiO_2 acts as a seed layer and is applied by Plasma Enhanced Chemical Vapor Deposition (PECVD) with an *Oxford Instruments PlasmaLab80Plus* system as a remedy. The Al_2O_3 is grown by Atomic Layer Deposition (ALD) with a *Cambridge NanoTech Savannah 100* system, which deposits the oxide in atomic layers by alternately exposing the sample to trimethylaluminium ($Al_2(CH_3)_6$) and de-ionized water (H_2O). Standard recipes

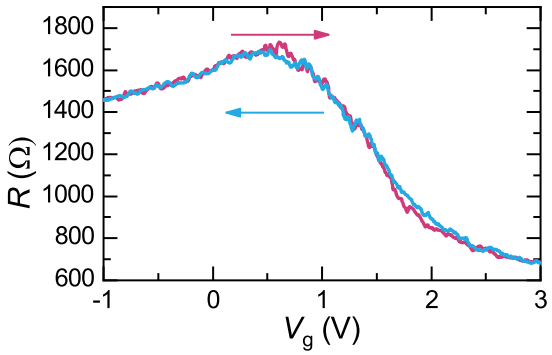

Figure 4.4: Typical gate voltage dependence of the zero-field resistance R of a nanowire. Blue and orange lines represent opposite sweeping directions. A hysteresis is not visible for typical sweeping rates.

for both SiO_2 and Al_2O_3 require temperatures of far above 100 °C to achieve optimal oxide quality. Due to the requirements of HgTe, both PECVD and ALD processes are limited to 80 °C to prevent damage to the material. Growth quality is therefore not optimal, as the process was not intended for use below 90 °C. Side effects can be mitigated by choosing longer waiting (*purge*) times between reactant pulses. The combination of SiO_2 and Al_2O_3 has proven reliable against breakthroughs. The large permittivity of Al_2O_3 ($\epsilon_r = 9.1$) is present even under these growth conditions as shown by a comparison of filling rates to a plate capacitor model in App. A.2. A hysteresis in the gate behaviour is absent, as shown in Fig. 4.4. Samples can be easily tuned to ±5 V, which permits access to VB, bulk gap, and CB in all investigated devices.

Metallization

The topgate stack is finished by depositing a standard metallic electrode, consisting of a 5-10 nm thin layer of titanium and a 100 nm layer of gold. The titanium layer is included to improve adhesion. Before depositing the metals in a *Leybold Univex 450* system by thermal evaporation, the sample is processed with optical lithography. The mask is designed to reduce chance of gate breakthrough by avoiding an overlap of topgate contacts with the mesa. In a final lift-off step, the excess material is removed from the sample. An additional adhesion-promoting sputtering step with argon plasma before metal deposition was left out to prevent degradation of the wafer and oxides.

4.4 Ohmic contacts

The fabrication of ohmic contacts is usually carried out by evaporating metallic pads on outer regions of the mesa. The CdTe cap layer of the Cd_xTe_{1-x}/HgTe systems have a low surface roughness. This is presumably why bonding wires to metallic contact pads has unsatisfactory success rates, as the pads are torn from the sample in the process. Additional pre-sputtering steps, that would increase adhesion of the metallic pads to the sample, lead to degradation of material quality. The method of choice has therefore become to solder contacts with indium by hand[1]. First, the mesa contact is metallized with a soldering iron and indium. The sample is then placed in a chip carrier and bonded next to the indium dabs. Owing to a lack of metallic pads on the chip, the second bond is generally unsuccessful. Instead, the loose end is pushed into the indium with tweezers.

[1]For a detailed set of parameters, see Appendix B.

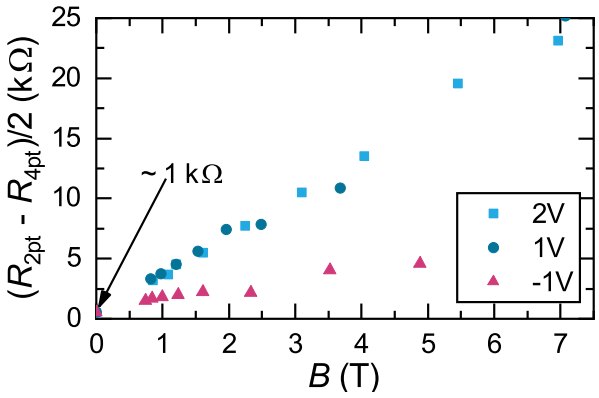

Figure 4.5: The total contact resistance is determined from the difference of two- R_{2pt} and four-point resistance R_{4pt} at quantum Hall plateaus. Data is shown for three gate voltages corresponding to valence band (−1 V), bulk gap (1 V), and CB (2 V) in the commonly used 80 nm wafer.

Contact resistance is reliably below 1 kΩ. However, the sample designs include long ungated leads which together with the low carrier densities of HgTe systems lead to large two-point resistances at high magnetic fields. Figure 4.5 shows the total resistance of a contact and its lead as a function of the magnetic field. The resistance has been measured by applying quantizing magnetic fields in both two- and four-point measurements. The difference in resistance at quantum Hall plateaus gives the total resistance of two contacts and leads, which becomes significant for very high fields and needs to be taken into account for the measurement setup.

4.5 Cryostat

Low-temperatures and high magnetic fields are indispensable for fundamental research on semiconductors and in particular semiconductor nanostructures. For the observation of quantum effects, such as the QHE, temperatures of 4.2 K and lower are needed. For phase-coherent effects, such as Aharonov-Bohm type effects, one needs to cool even below 0.1 K. Experiments under such conditions are now widely accessible due to the discoveries of Dewar vessels [107, 108], the liquification of ^{4}He [109], ^{3}He/^{4}He mixtures for cooling [110, 111] and superconductivity [112] over the course of the last 125 years. The experiments in this thesis were almost exclusively carried out in a wet *Oxford Instruments Kelvinox TLM* dilution refrigerator, schematically shown in Fig. 4.6, with some additional measurements in ^{4}He bath cryostats. The following paragraphs will discuss the principle of a dilution refrigerator. For a more detailed discussion on these topics, see literature by Enss and Hunklinger [113] or Pobell [114].

Wet dilution refrigerator systems use evaporative cooling from liquid helium as a pre-cooling stage at 4.2 K. By pumping it through the 1 K-pot, a second pre-cooling stage at 1.5 K is achieved. The ^{3}He/^{4}He mixture flows into the dilution unit, passes by the ^{4}He bath and 1 K-pot, where it cools to below 2 K and liquefies.

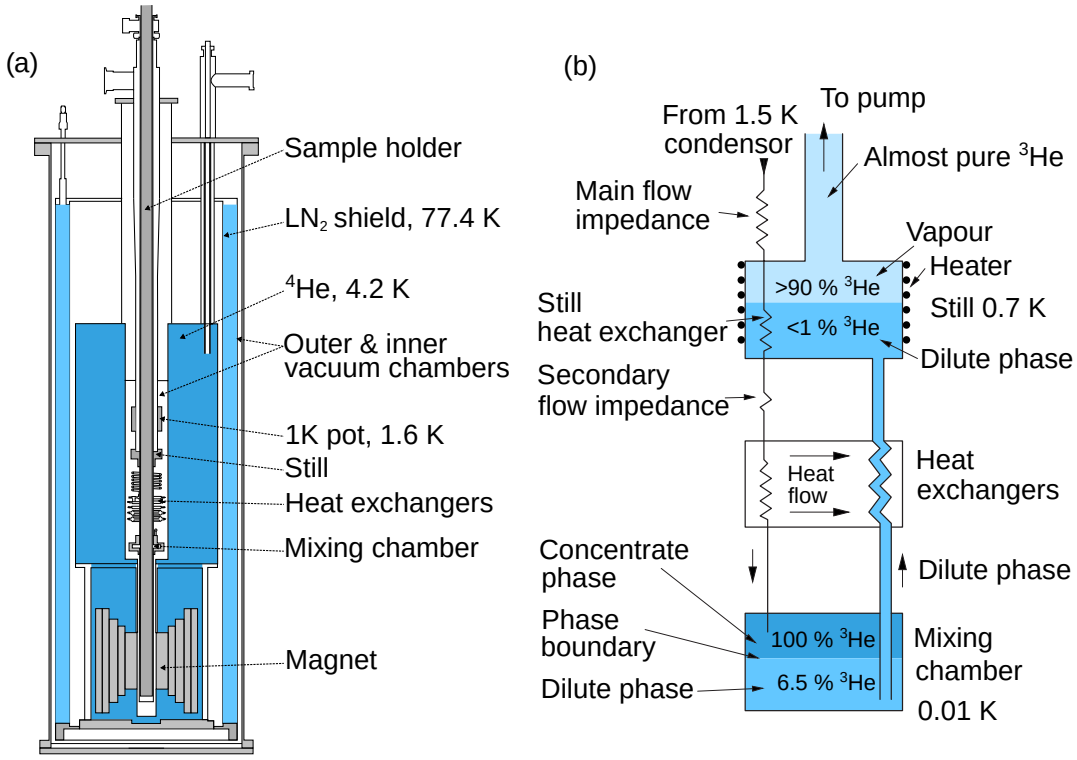

Figure 4.6: (a) Sketch of a wet top-loading dilution refridgerator (adapted from [113]). (b) Principle of operation for the inner circuit of a ^{3}He/^{4}He dilution unit (adapted from [114]).

When the mixture is cooled to below 0.872 K, it separates into two energetically more favourable phases in the mixing chamber — a concentrate and a dilute phase. This is the crucial effect for the operation of a dilution refrigerator. The concentrate phase is pure ^{3}He, whereas the dilute phase is mainly ^{4}He with at least 6.5 % of ^{3}He. The exact ratio depends on temperature and pressure. The mixture is pumped from the mixing chamber to the still by pumps in the closed circuit, where a dilute phase with $< 1\,\%$ ^{3}He forms. By continuously pumping, ^{3}He is drawn out of the dilute phase until it evaporates in the still. The ratio must be above 6.5 %, which is why ^{3}He continually crosses the phase boundary from the concentrate into the dilute phase in the mixing chamber. This transition costs energy, which is taken from the environment and leads to a cooling effect. The cooling power decreases with temperature and the lowest temperature is reached when the cooling power equals external heating. Temperatures down to 1.5 mK have been reported [115]. On the employed *Kelvinox TLM* system, temperatures down to 15 mK can be achieved depending on the sample holder. The upper temperature limit is at 1 K. Experiments at higher temperatures need to be carried out in ^{3}He or ^{4}He bath cryostat.

The *Kelvinox* system is fitted with a superconducting magnet capable of magnet fields up to 19 T. A rotating sample holder, that allows continuous rotation of up to 180 °, makes in- and out-of-plane magnetic field configurations possible within the same temperature cycle. The rotating sample holder includes a switch board just above the sample location. This allows for the installation of small filtering devices before connecting to room temperature equipment, that will be described in the following section.

4.6 Electronics

Measurements were carried out with standard AC lock-in techniques at frequencies of 17 Hz or lower in four-point configurations with *Signal Recovery DSP 7265* lock-ins. In studies of nanostructures, the applied bias current was chosen so that the four-point voltage drop $U_{4\mathrm{pt}} < k_\mathrm{B}T/e$, where k_B is the Boltzmann constant. This condition allows an estimate of when voltage averaging will begin to smear out the subband features in investigated nanostructures. The full setup is shown in Fig. 4.7. A *Yokogawa 7651* voltage source supplied a constant topgate voltage. *Femto DLPVA-100-F-D* pre-amplifiers, with an input resistance of 1 TΩ, were included in the setup to mitigate possible issues caused by high contact resistances at large magnetic fields. Measurements of nanostructures at mK temperatures require special care to prevent heating of the sample from external sources. To prevent high frequency noise on the signal lines, π-filters are included in the setup per default [116]. They effectively act as low-pass filters. With a capacitance of 1.5 nF and typical sample resistances of some kΩ, the cut-off frequency is much larger than the oscillation frequency and does not influence signal transmission. At high magnetic fields, the two-point sample resistance of the investigated HgTe devices rises to ∼MΩ, which can quickly lead to cut-off frequencies on the order of the applied AC signal. This needs to be considered for the choice of the lock-in frequency.

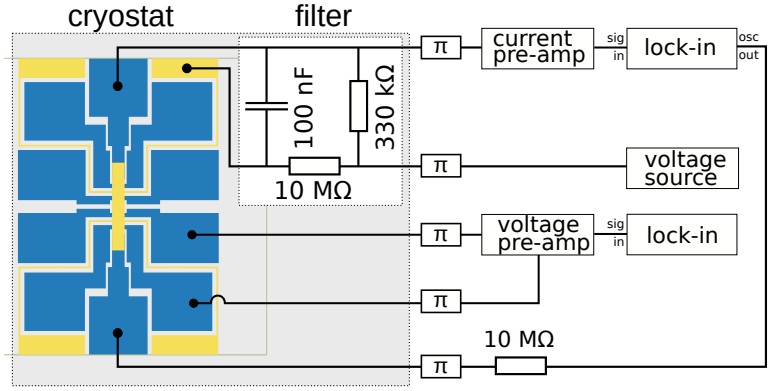

Figure 4.7: Measurement setup for nanostructures susceptible to perturbations of the topgate potential. The standard AC lock-in setup is extended by a cold low-pass filter, π-filters and pre-amplifiers.

The setup has been optimized to prevent noise from ground loops. All measurement devices (lock-in, voltage source, etc.) are insulated from the power line by insulating transformers and configured to not pass the ground potential to input/output jacks where possible. The cryostat is electrically decoupled from pumps and control equipment and the ground potential is defined through a single low-impedance cable. Even with all these optimizations, measurements of nanostructures still proved troublesome because of perturbations of the topgate potential by noise on the signal line. Filtering outside the cryostat did not prove sufficient, so that a filter was built for use in the rotating sample holder directly above the sample (design after Ref. [117]). This way, all high-frequency noise, which couples to the signal line in the sample holder, can be filtered and the DC voltage at the topgate stabilized. The filter, shown in Fig. 4.7, combines a current divider with a low-pass filter. The former is formed with two resistors (330 kΩ and 10 MΩ), which in a first step reduces the amplitude of the high-frequency noise signal. The amplitude is decreased by the ratio of the two resistors. The second component, a low-pass filter formed by the larger resistor and the capacitor, attenuates all signal components above the cut-off frequency $f_c = 1/(2\pi RC)$. With values of 10 MΩ and 100 nF, a time constant of $\tau = 1\,\mathrm{s}$ and a cut-off frequency of $f_c \approx 0.16\,\mathrm{Hz}$ is achieved. Applying a gate voltage leads to a DC current to ground in the discussed setup. This requires an additional current pre-amplifier as the lock-in is unsuited to handle large DC offsets. Moreover, the current across the 330 kΩ resistor causes noticeable heating due to the proximity of the filter to the sample and mixing chamber.[2] In the pictured configuration, heating in the mixing chamber is usually within 2...3 mK for typical gate voltages of $V_\mathrm{g} = \pm 3\,\mathrm{V}$ and a base temperature of $T = 50\,\mathrm{mK}$. The time constant of $\tau = 1\,\mathrm{s}$ also entails a manageable delay of the topgate potential and avoids an artificial hysteresis in V_g-sweeps. The positive effect of the filter on measurements of nanodevices is demonstrated in the context of an 3DTI Aharonov-Bohm ring structure in Sec. 6.1.1.

[2] A smaller resistor would have increased filtering efficiency at the cost of additional heating.

5

Macroscopic devices

The quantum Hall effect is a main pillar for transport characterization of high mobility 2DESs. The majority of systems investigated for this work were fabricated from strained HgTe thin films, which represent a complex combination of such two-dimensional systems. A thorough understanding of the QHE in macroscopic HgTe Hall bars is therefore important for a correct characterization of the material and interpretation of experiments on nanostructures. With this in mind, the QHE in 80 nm strained HgTe was investigated.

5.1 Quantum Hall effect in strained HgTe

A high-resolution Landau fan chart of 80 nm strained HgTe was recorded from a 200 µm wide and 1100 µm long Hall bar. Figure 5.1(a) shows the longitudinal conductivity σ_{xx} at 50 mK for fields up to 12 T. The presented gate voltage range of $V_\mathrm{g} = -3...4\,\mathrm{V}$ corresponds to transport in the CB, bulk gap, and VB regimes. The features confirm previously published studies of magnetotransport in (013)-oriented HgTe thin films [25, 51], with n- and p-type Landau levels that can be traced back to three distinct origins on the V_g-axis and a change of slope of the Landau levels at the transition from gap to conduction band. The latter is distinctly visible around $V_\mathrm{g} = 1.2\,\mathrm{V}$ in Fig. 5.1(b), which shows the low-field section of the data set. The change in slope is caused by an additional contribution from bulk CB states to the total filling rate $\alpha^\mathrm{tot} = \alpha^\mathrm{top}_\mathrm{gap} + \alpha^\mathrm{bot}_\mathrm{gap} + \alpha^\mathrm{bulk}_\mathrm{CB}$. As α^tot is constant, filling rates for top and bottom surfaces decrease. In Fig. 5.1(b), the location of the gap becomes easily recognizable via a V_g-range of lower conductivity, which translates to a darker vertical stripe in the colour map between 0.15 to 1.2 V. In the CB regime ($V_\mathrm{g}^{E_\mathrm{c}} => 1.2\,\mathrm{V}$), an overlay of two Landau level fans is visible. The first stems from TSS, which are present both in the energy gap and the CB regime. The second set appears only for $V_\mathrm{g}^{E_\mathrm{c}} > 1.2\,\mathrm{V}$, and originates from bulk CB states.

This attribution is justified by an analysis of charge carrier densities n_s, using magnetotransport measurements. The densities, extracted from the classical

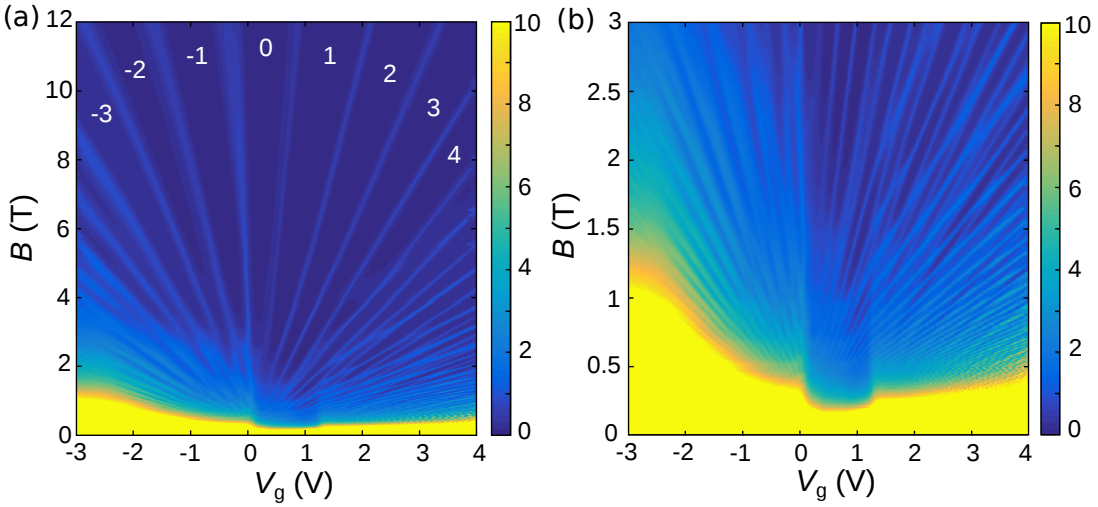

Figure 5.1: Landau fans for the QHE in a macroscopic Hall bar of 80 nm strained HgTe. (a) The conductance σ_{xx} is plotted in units of e^2/h (colour bar) as a function of magnetic field B and gate voltage V_g. Data was recorded up to 12 T and at 50 mK. The integer numbers denote the total filling factor, extracted from σ_{xy} data. The low-field regime up to 3 T is shown in (b). The bulk gap is clearly visible as a (darker) region of lower conductance between 0.15 and 1.20 V.

Hall effect and high-field SdHs, represent the total charge carrier density n_s^tot. Low-field SdHs originate from the top surface only, giving access to n_s^top. This has been confirmed by analysis of quantum oscillations in magnetocapacitance measurements that probe the top surface only [25]. In this way n_s^tot can be separated into n_s^top and n_s^bot, due to $n_s^\mathrm{tot} = n_s^\mathrm{top} + n_s^\mathrm{bot}$, when E_F is located to the bulk gap. Outside the gap, analysis is similar. However, if E_F is located in the CB, the additional conducting channel from bulk electrons prevents an insight beyond the total and top charge carrier densities. In the VB-regime, the coexistence of Dirac electrons and bulk holes leads to non-linear Hall resistances. Analysis of their respective carrier densities requires a two-carrier Drude model. These methods are described in detail in Refs. [25, 51] and [118]. The resulting electrostatic model is described in the supplemental material of Ref. [25]. It has been confirmed by theoretical calculations [119]. Characterisation measurements from the presently discussed Hall bar are presented in App. A.2 and can be viewed representatively for all investigated 80 nm strained HgTe wafers with the standard topgate stack of 30 nm SiO_2 and 100 nm Al_2O_3. Electron mobilities μ_e typically reach values of $400 \cdot 10^3\,\mathrm{cm}^{-2}$, with maximum hole mobilities of 100 to $200 \cdot 10^3\,\mathrm{cm}^{-2}$. The edges of the bulk bands are located approximately at $V_\mathrm{g}^{E_\mathrm{v}} = 0.15$ and $V_\mathrm{g}^{E_\mathrm{c}} = 1.2\,\mathrm{V}$. The mean free path length of electrons l_e is between 2 and 3 µm in the bulk gap.

In Fig. 5.1(a), a Landau gap with an attributed filling factor of $\nu = 0$ is visi-

ble, which is an anticipated feature of the QHE in 3DTIs. It is a consequence of a gap opening in the zero energy Landau level of systems with linear dispersion [56]. Depending on the nature of this state, it may exhibit dissipative edge conduction [120–122] or appear as the result of an insulating state without edge conduction [67]. In the latter case, the longitudinal and transversal resistivities will deviate to large values. Calculation of the Hall conductance via $\sigma_{xy} = \rho_{xy}/(\rho_{xx}^2 + \rho_{xy}^2)$ will give the appearance of a zero Hall plateau, despite the origin being an insulating state. The nature of the presently observed feature requires further investigation.

Another signature feature of the QHE in 3DTIs are missing steps in the Hall plateau sequence. They result from the presence of two quantized surfaces. Depending on the distribution of the charge carrier density, difference sequences can occur. In the homogeneous case, where $n_s^{top} = n_s^{bot}$, both surfaces have the same filling factor, so that the Hall conductance becomes $\sigma_{xy} = (2\nu + 1)e^2/h$. This case has been previously observed, e.g. in strained HgTe [52, 54]. The data obtained from a 50 nm strained HgTe thin film, shown in Fig. 5.2(a), present the inhomogeneous case. Hall magnetoconductance traces $G_{xy}(B)$ are shown for the bulk gap (1...2 V) and the conduction band regime (2...3 V). A detailed characterization, including extraction of $V_g^{E_v}$ and $V_g^{E_c}$ is found in App. A.1. The ratio of charge carrier densities on top and bottom surfaces is 57 %/43 %, which leads to different periodicities in $1/B$. The result are missing plateaus at $G_{xy} = 3, 5,$ and $7\,e^2/h$.

A further possibility for the experimental confirmation of the origin of SdH oscillations in the topological surfaces, with a Dirac-like dispersion and $g_s = 1$, are measurements in tilted fields. In classical 2DESs, the Landau gap depends on

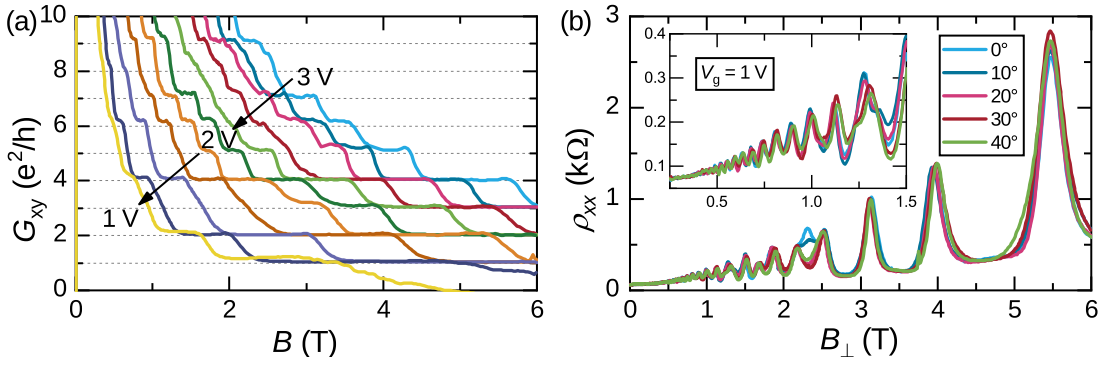

Figure 5.2: (a) Hall conductance G_{xy} as measured in 50 nm strained HgTe for V_g corresponding to the bulk gap and CB. Missing QH plateaus are observed in the bulk gap regime ($V_g < 2$ V). (b) Shubnikov-de Haas oscillations in strained HgTe at various tilt angles and a gate voltage of $V_g = 1.0$ V, shown as a function of the perpendicular field component $B_\perp$. The low-field regime is magnified in the inset.

the magnetic field component perpendicular to the sample plane $B_\perp$, while the Zeeman gap is a function of the total applied magnetic field B. Increasing the tilt angle of such a sample leads to enhanced spin-splitting in SdH oscillations. Fig. 5.2(b) presents magnetoresistance traces as a function of the perpendicular field component $B_\perp$. The angle between magnetic field and the surface normal of the strained HgTe samples was varied from 0 ° to 40 °. As expected, the periodicity of SdH oscillations is unaffected in this representation. Furthermore, the oscillation patterns of the traces show no dependence on the tilt angle, i.e. no spin-splitting appears for higher tilt angles. In a system with spin-degeneracy, a doubling of the periodicity would be expected at lower fields, due to the increased Zeeman-splitting energy. This is not observed in any B-field range, including at the onset of SdH oscillations at $B = 0.5\,\mathrm{T}$. The observations match the expected behaviour for a QHE, and more specifically low-field SdH oscillations, which arise from a topological surface.

5.2 Coexisting n- and p-type Landau levels

Upon closer examination, the high resolution data set, shown in Fig. 5.1, brings to light shifts in the p-conducting Landau fan structure at low-fields. Figure 5.3 presents the second derivative $\partial^2\sigma_{xx}/\partial V_\mathrm{g}^2$ of a cut-out from the region shown in Fig. 5.1(b). Blue regions in the colour plot mark maxima in the SdH oscillation pattern, while the yellow/green areas in between mark minima in σ_{xx}. They correspond to Landau gaps and Landau levels, respectively. Again, the transition from bulk gap to the CB is clearly visible at 1.2 V with the onset of a second set of Landau levels. In the valence band, Landau levels exhibit an unusual behaviour at fields below 1.5 T. At every intersection of the p-type LLs with lines of positive slope, highlighted by red, dashed lines, shifts are observed in the Landau level/gap structure. The same shifts are seen in the Hall signal. These lines are therefore assumed to be a Landau fan stemming from the upper topological surface states. The fan structure connects to the Landau fan of surface states in the bulk energy gap at $V_\mathrm{g}^{E_\mathrm{v}} = 0.15\,\mathrm{V}$, where the slope changes in the same fashion as at the gap-CB transition. Here, bulk VB states become the additional contribution to the constant total filling factor, $\alpha^\mathrm{tot} = \alpha^\mathrm{top}_\mathrm{gap} + \alpha^\mathrm{bot}_\mathrm{gap} + \alpha^\mathrm{bulk}_\mathrm{VB}$.

Overlapping Landau fans are known from two-subband GaAs/AlGaAs 2DESs, where both crossing and anti-crossing Landau levels of the same carrier type have been observed [123–125]. More recently, experimental results were obtained for coexisting n- and p-type Landau levels in an InAs/GaSb quantum wells [126], where avoided crossings were attributed to electron-hole hybridization.

The data confirms that both a 2DES from the surface states and a 2DHS from bulk hole states are present simultaneously in strained HgTe with two indepen-

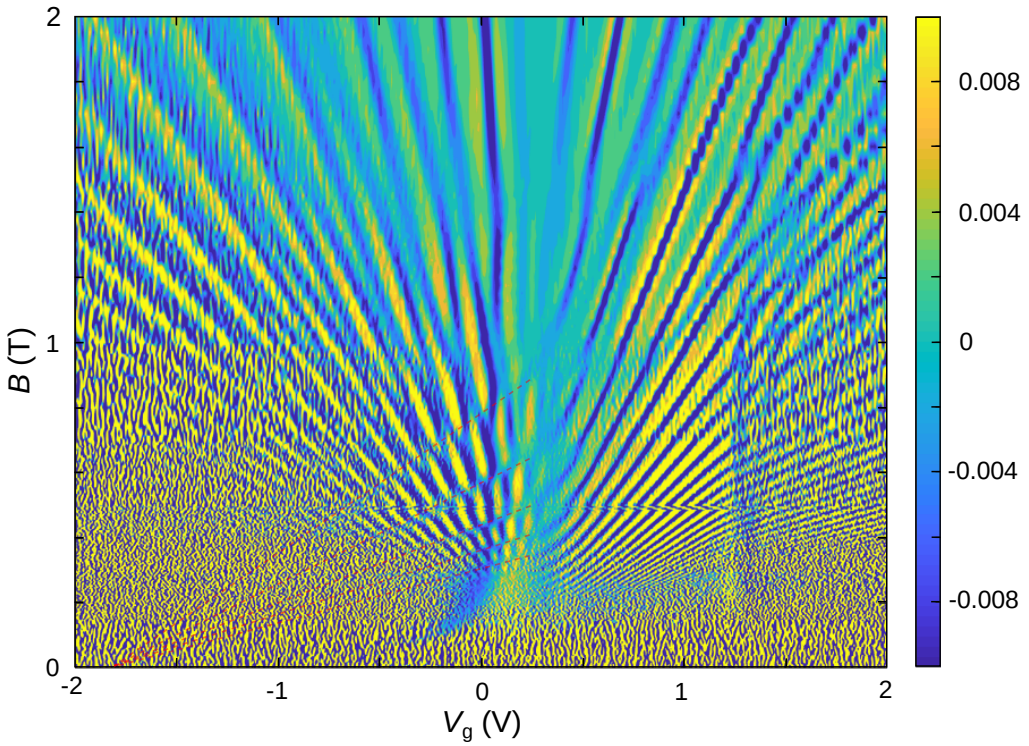

Figure 5.3: Landau fan chart from Fig. 5.1 plotted as second derivative of the conductance $\partial^2\sigma_{xx}/\partial V_{\mathrm{g}}^2$ for $B < 2\,\mathrm{T}$ and $V_g = -2...2\,\mathrm{V}$. The derivative was computed numerically for each V_{g}-trace. An intricate pattern of overlapping Landau fans from bulk and surface electrons is visible in the CB regime ($V_{\mathrm{g}}^{E_{\mathrm{c}}} > 1.2$). In the gap, only the Landau fan from surface electrons are present. In the VB regime ($V_{\mathrm{g}}^{E_{\mathrm{v}}} < 0.3$), the surface state Landau levels (marked by red, dashed lines) intersect with bulk hole Landau levels.

dent Landau level sequences arising from each. The bulk hole states are assumed to form a two-dimensional system below the top interface due to the field effect, as described in the supplemental material of Ref. [25]. The shifts between Landau levels and Landau gaps along diagonal lines in the fan chart, suggests an interplay between both two-dimensional systems.

6
Mesoscopic devices

The transition to wet-etched nanostructures was first made with a 3DTI Aharonov-Bohm ring and antidot-arrays in HgTe quantum wells. The Aharonov-Bohm ring, discussed in Sec. 6.1, was fabricated from 80 nm thick strained HgTe-based 3DTI. In such an AB ring, the surface states form a torus-like surface with openings at the attached leads. Analysing Aharonov-Bohm oscillations gives access to crucial properties of the charge carriers, such as the phase coherence length l_ϕ. An overall idea for the overall feasibility of interference experiments in HgTe nanostructures fabricated with the developed methods can be obtained as well. These low-field measurements are presented in Sec. 6.1.1, while Sec. 6.1.2 discusses experiments in quantizing magnetic fields.

The antidot array, described in Sec. 6.2, was etched into an 8 nm thick HgTe quantum well, which constitutes a 2DTI, with the aim of detecting interfering helical QSH edge states. Around each antidot, a circular edge state should exist, which would pick up a phase when a magnetic field is applied. The goal was to detect the resulting Aharonov-Bohm oscillations. Experiments with these devices also proved to be important for optimizing the setup, which was crucial for the investigation of nanowires in Cha. 7.

6.1 3D topological insulator ring

The Aharonov-Bohm ring, shown in Fig. 6.1, was etched from a capped 80 nm strained HgTe wafer. It was built in a four-point geometry to exclude lead resistances before and after the ring structure. The median radius of the device is $\bar{r} = 435$ nm. The wet-chemical etching process produces slanted sides, which means the inner and outer radii of top and bottom surfaces of the ring structure differ as the cross section widens towards the bottom. The inner radius r_i decreases from 372 nm at the top to 281 nm at the bottom surface, while the outer radius r_a increases from 500 nm to 576 nm. The measurements are taken from the colour gradient in SEM-micrographs. The channel width therefore varies from 130 nm at the top to 295 nm at the bottom surface. The oscillation period for

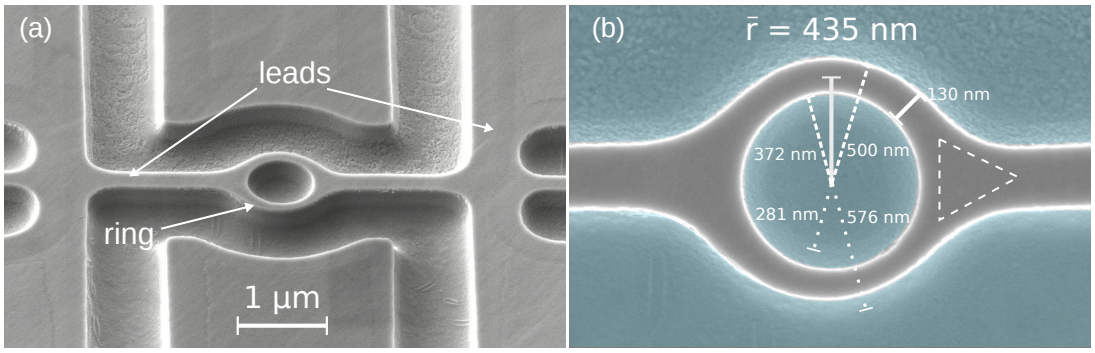

Figure 6.1: SEM-Micrographs of a ring structure in an 80 nm HgTe thin film, where (a) shows the entire nanostructure (ring and leads) at a tilt angle of 50 °. (b) Close-up SEM-micrograph in top-view. Blue sections mark the etched area, the remaining mesa is grey. Slanted side wall from wet-chemical etching lead to varying radii for top (dashed) and bottom (dotted) surfaces. The extent of the bottom surface can be identified from the grey scale gradient.

the mean radius is given by $\Delta B_{h/e} = 7\,\mathrm{mT}$, according to Eq. 3.18. Oscillations are expected for a wide range of periods from 4.3 mT to 15 mT.

6.1.1 Aharonov-Bohm interference

Initial measurements, in out-of-plane magnetic fields, showed oscillatory behaviour matching the expected periodicity. However, a critical feature of phase coherent effects was not present. As shown in Fig. 6.2(a), the magnetotransport curves of

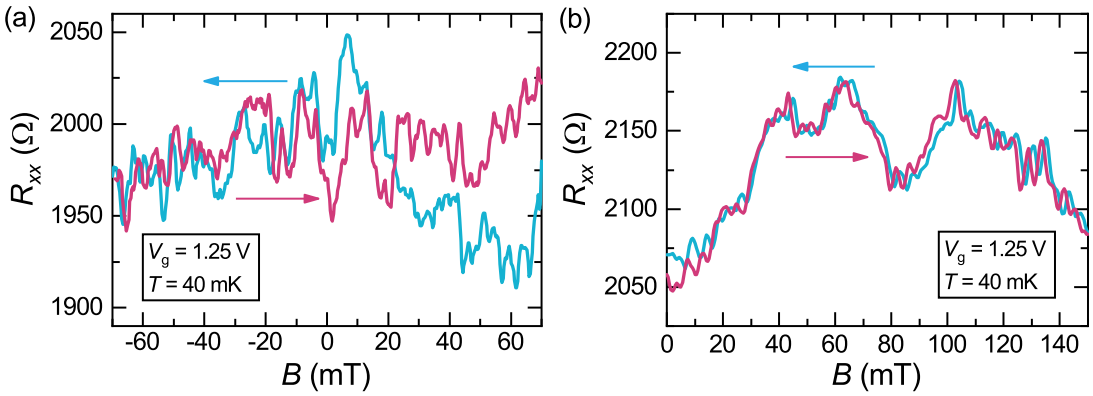

Figure 6.2: Magnetoconductance curves recorded (a) before and (b) after the introduction of a cold low-pass RC-filter. Coloured arrows indicate sweep directions. The filter eliminates fluctuations of the topgate potential and consequently the Fermi level E_F in the nanostructure, making reproducible traces between up- and down-sweeps possible. The circuit diagram is shown in Fig. 4.7.

two subsequent sweeps at fixed gate voltage V_g did not exhibit reproducible oscillations with a fixed phase. However, the traces do show similar features between -40 and -70 mT, which points toward fluctuations of the topgate potential (and thereby E_F) as the source. A first attempt at stabilizing the topgate voltage was made by adding a low-pass filter outside the cryostat. This did not prove sufficient and indicates that high frequency noise couples to the signal lines of the sample holder. Therefore a passive low-pass filter was designed (after Ref. [117]) and installed in the sample holder. The filter is located roughly 30 cm above the sample and cooled to roughly 1 K. For further details on design and principle of the filter, see Cha. 4.6.

Installation of the low-pass filter results in a stable topgate potential. Traces from subsequent up- and down-sweeps exhibit identical oscillations. The small shift of the phase can be attributed to hysteretic behaviour of the superconducting magnet. With this enhancement to the setup, nanodevices can be kept in a fixed state long enough to study oscillations over a large magnetic field range and their dependence on other parameters. Sweeping V_g, and returning to the same value,

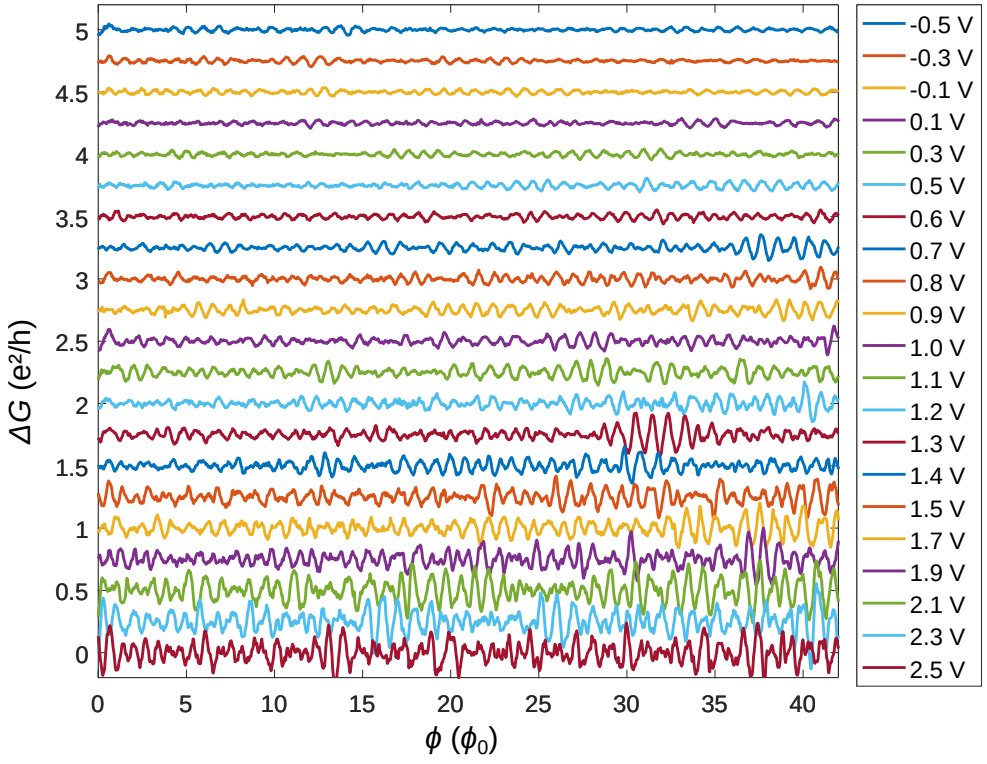

Figure 6.3: The conductance correction ΔG of the ring structure is plotted against the magnetic flux ϕ for a large number of gate voltages V_g. Clear ϕ_0-periodic oscillations are observed throughout the entire investigated V_g-region. The amplitude of the oscillations increases for V_g in the conduction band-region. Curves are offset for clarity.

will still result in a different state and set of oscillations. The difference in the absolute value of R_{xx} between the traces in Figs. 6.2(a) and (b) can be attributed to temperature cycling when installing the filter in the sample holder.

With reproducibility of magnetotransport curves ensured by a stabilized V_g, a detailed study of Aharonov-Bohm oscillations was carried out. Figure 6.3 shows the conductance correction ΔG as a function of the magnetic flux ϕ for gate voltages V_g ranging from conduction ($> 1.5\,\mathrm{V}$) to the valence band ($< 0.5\,\mathrm{V}$). A smooth background is subtracted from the measured conductance, using the method described in Sec. 7.3 and App. C. The traces have strong ϕ_0-periodic behaviour throughout the studied V_g-range with increasing amplitudes and a richer behaviour in the CB. For $V_g \leq 0.5\,\mathrm{V}$, amplitudes are increasingly suppressed, which may be attributed to the coexistence with bulk holes with low mobility. This trend is confirmed by fast Fourier transforms (FFT) of the conductance correction-traces, shown in Fig. 6.4(a) in the form of a colour plot. The spectral weight is centred around $f_B \approx 150\,\mathrm{T}^{-1}$ throughout, with an overall smaller FFT magnitude in the VB and a larger FFT magnitude in the CB. Figure 6.4(b) shows the V_g-average of the data in (a). The main peak centers around a frequency of $f_B = 163\,\mathrm{T}^{-1}$. This corresponds to a radius of $r = 463\,\mathrm{nm}$, which agrees well with the median radius $\bar{r}$ of the structure. Additionally, several side peaks emerge that match various possible closed paths, including the smallest and largest radii of the toroid.

Further measurements were carried out to study the decay of oscillation amplitudes with rising temperature. In ballistic devices, l_ϕ is expected to decay

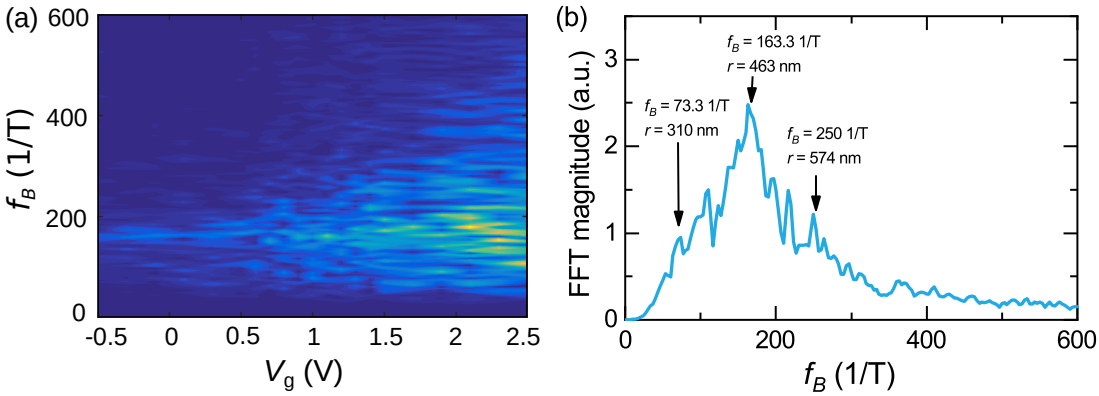

Figure 6.4: FFT analysis of ϕ_0-periodic oscillations. (a) Fast Fourier transforms are computed for all magnetoconductance traces in Fig. 6.3 and shown as a function of V_g and f_B. The FFT magnitude is encoded in the colour scheme, where yellow denotes large values. (b) In the V_g-averaged spectrum, the highest spectral weight corresponds to the median radius $\bar{r}$ with side peaks matching the minimal and maximal radii of the toroid.

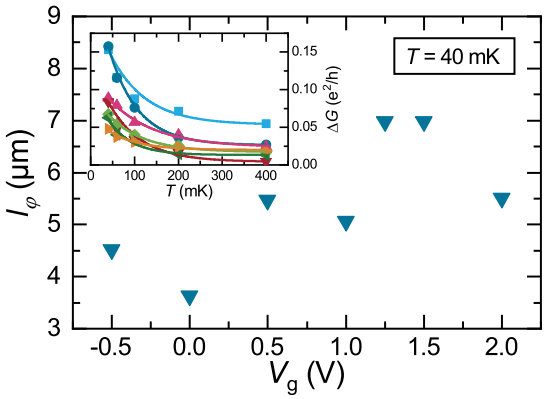

Figure 6.5: The phase coherence length l_ϕ in the 3DTI ring for a number of gate voltages V_g. l_ϕ is extracted from the exponential decay of oscillation amplitudes with rising temperature. Best fits are shown in the inset.

exponentially with rising T,

$$\Delta G \propto exp\left(-\frac{P}{l_\phi(T)}\right). \tag{6.1}$$

l_ϕ is calculated from the exponential decay parameter using the median torus radius $\bar{r}$ and the experimental temperature of 40 mK. Values are shown in Fig. 6.5 and range from 3.5 to 7 µm, but do not show a strong dependency on V_g, which would allow for an attribution to regimes of dominating bulk or surface conduction. Regardless, phase coherence lengths l_ϕ are larger than the device perimeter P even for $V_\mathrm{g} \leq 0$ V, which is associated with the VB. For $V_\mathrm{g} > 1$ V, l_ϕ approaches 7 µm which exceeds the device perimeter by roughly a factor of 2.5.

The complex interplay of a non-ideal cross section, inhomogeneous carrier density distribution due to gating, and possible closed paths with a wide range of radii led to feature rich oscillations and FFT spectrum. The quantum conductance oscillations are too complicated to attribute certain frequencies to specific facets of the toroidal geometry or even higher order $h/2e$-oscillations.

6.1.2 Quantum Hall interference

In fields larger than roughly 0.4 T, the h/e-periodic oscillations begin to disappear as the perpendicular magnetic field quantizes the top and bottom surfaces of the toroid. QH edge channels are expected to form and possibly interfere, given the narrow device dimensions [79].

The experimental data of the 3DTI Aharonov-Bohm ring with its toroidal surface states is shown in Fig. 6.6(a). The traces were recorded at $V_\mathrm{g} = 1.25$ V, which constitutes a Fermi energy position in the bulk energy gap. A number of oscillating signal contributions are visible at the transitions between QH plateaus in R_{xy}. The ring resistance R presents a similar picture, with varying oscillating behaviour superimposed on oscillations. The feature-rich oscillatory behaviour

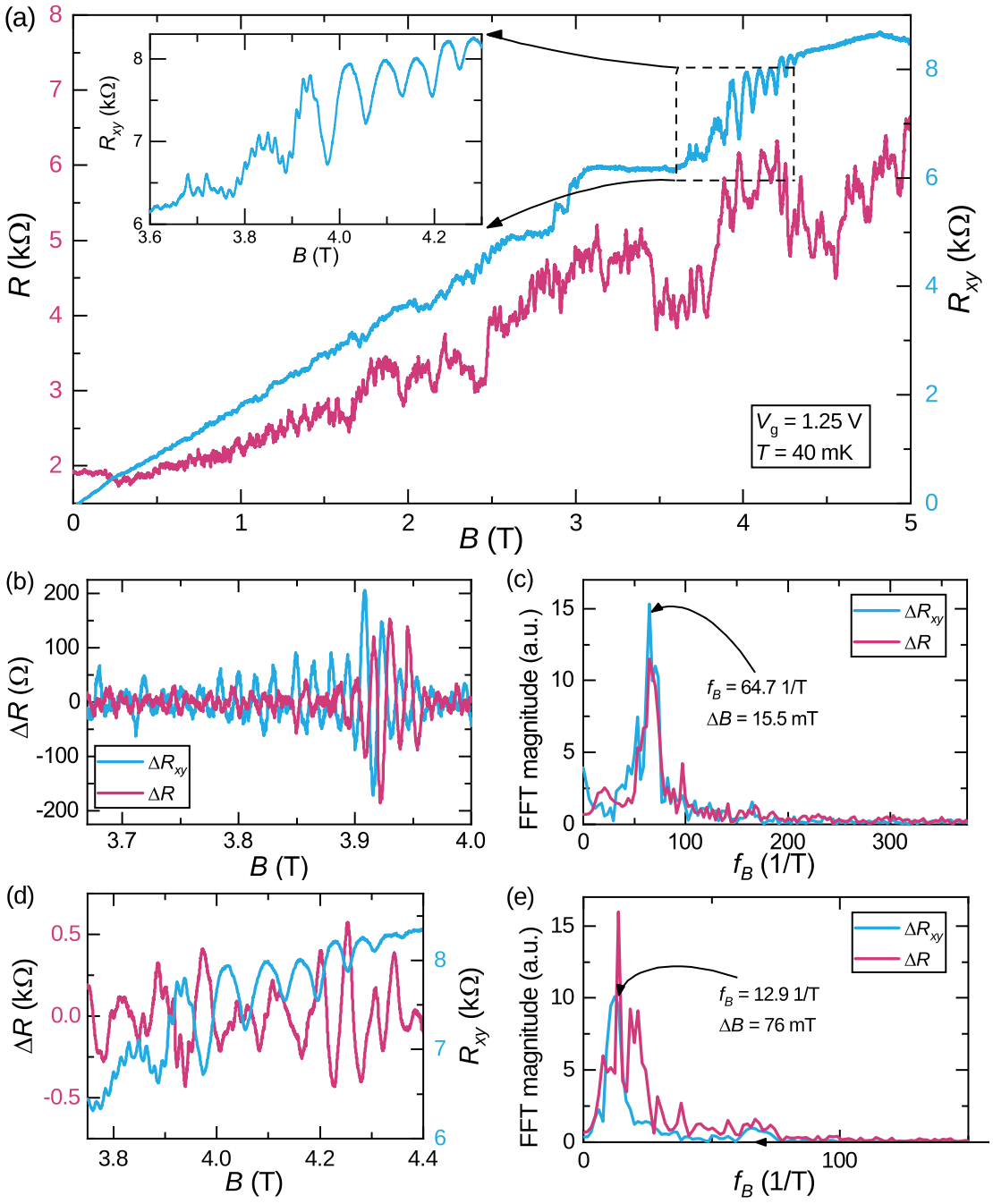

Figure 6.6: Analysis of interfering chiral edge channels in a 3DTI ring. (a) QH measurement of the 3DTI ring structure at $T = 40\,\mathrm{mK}$ and $V_\mathrm{g} = 1.25\,\mathrm{V}$. At the transitions between plateaus oscillations are observed in R_{xy}. The inset magnifies a superposition of oscillations between $\nu = 3$ and $\nu = 4$ plateaus. (b) The high-frequency signal from the inset in (a) is isolated and plotted with the complimentary oscillations in R. The traces show anti-phase behaviour and a matching period. (c) FFT spectra of the traces in (b) verify the matching periodicities. (d), (e) The same analysis is carried it for the oscillations with lower frequency. Ring and Hall resistances, ΔR and R_{xy}, are plotted in (d), and corresponding FFT spectra in (e).

will be discussed in the following using some examples. The first is shown in the inset of (a). Here, the transversal signal exhibits two superimposed interference patterns at the transition between two QH plateaus at $B \approx 4\,\mathrm{T}$. The high-frequency signal is extracted by subtraction of a smooth background and plotted in Fig. 6.6(b). An analogous pattern is observed in R_{ring} and plotted alongside, showing an anti-phase behaviour. The corresponding FFTs, plotted in Fig. 6.6(c), show distinct peaks for a period of $\Delta B = 15.5\,\mathrm{mT}$, which matches h/e-periodic oscillations for a ring with radius $r = 290\,\mathrm{nm}$. This is in good agreement with the inner radius of the bottom surface.

The predominant periodicities in the data are between $\Delta B = 46$ and $76\,\mathrm{mT}$ and are present in both R_{xy} and throughout the observed B-field range in R. An examples of a plateau-to-plateau transition ($\nu = 3$ to 4) near 4 T is extracted from Fig. 6.6(a) and shown in (d) together with the respective FFT spectrum in (e). A frequency peak at $f_B = 12.9\,\mathrm{T}^{-1}$ is found in both signals. An analogous behaviour is observed at the transition from filling factor $\nu = 5$ to 6 at $B = 2.5\,\mathrm{T}$. Here, a frequency of $f_B = 21.7\,\mathrm{T}^{-1}$ is found. These features stem from loops with an enclosed area smaller than the ring, so that their origin must be on a different part of the nanostructure. Possible candidates are the triangular transition regions between ring and leads. The extracted periods match isosceles triangles with $w \times h$ of 410×425 nm for the transition near 4 T and 330×335 nm near 2.5 T, visualized in Fig. 6.1(b). A shift to larger periods ΔB, i.e. smaller frequencies f_B, with higher magnetic fields, is indicative of edge states being pushed to the outer edge of the device. This is in agreement with reports in literature [127]. Another possible source are junctions where the voltage probes intersect with the current path [see Fig. 6.1(a)]. The signals are present in both longitudinal and transversal resistances and the dimensions of the transition regions are a much better fit for the observed periods. An origin of the lower periodic oscillations in Fig. 6.6(d) in the transition regions is therefore likely.

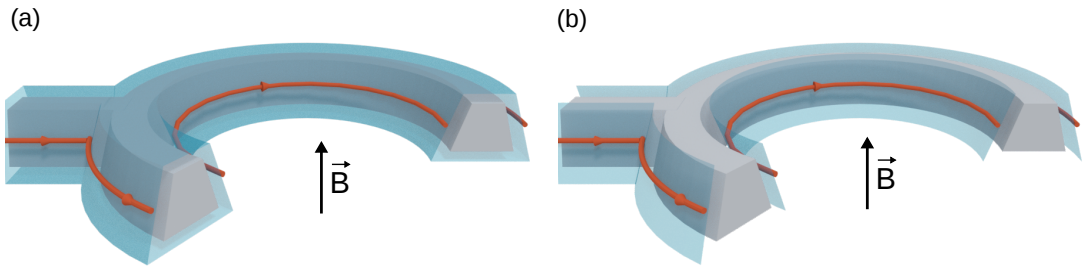

Figure 6.7: Sketch of a 3DTI ring structure in a quantizing magnet field. (a) The Fermi energy coincides with a Landau level. Top and bottom surfaces therefore remain conducting. (b) The Fermi energy sits in a Landau gap, leaving only QH edge channels and side surfaces as conducting states.

AB interference of QH edge channels has been studied in systems such as QPC-based 1D electron interferometers [128] and AB rings of comparable size fabricated from 2DESs. For the latter system, a comprehensive summary was written by G. Timp [129]. The main points of the prevalent picture at high fields can be summarized like this: In low-field experiments, the current in 2DES ring structures is carried by diffusive states. In this regime, backscattering is allowed and consequently the Aharonov-Bohm effect is possible. At larger fields, current in high-mobility 2DESs is carried by QH edge channels. The ballistic edge channels follow the inner and outer perimeter of the device. This means that only the inner channel forms a flux-enclosing loop, which is, however, not connected to the leads. The outer edge channels are connected to the leads and determine transport behaviour, but do not enclose a flux. Backscattering is exponentially suppressed with increasing magnetic fields in ballistic edge channel transport [127]. This in turn suppresses Aharonov-Bohm oscillations in the longitudinal signal in large magnetic fields, because the inner edge channel loop becomes disconnected from the leads.

This picture can be transferred to the 3DTI ring discussed here. In the QH regime, the ballistic edge channels along the inner perimeter of the ring pick up a phase. The resulting conductance correction only contributes to the signal in between QH plateaus, where top and bottom surfaces are conducting. When the Fermi energy E_F is in a Landau gap, the closed loop on the inner surface is disconnected from the leads entirely. This is visualized in Fig. 6.7(a) and (b), respectively. This allows the conclusion that the bulk of nanostructures remains entirely insulating in the case that E_F is in the gap. A loss of strain due to the narrow device dimensions can be excluded.

6.2 Antidot lattice in a 2D topological insulator

Edge channels of a QSH insulator are topologically protected from backscattering, which results in a quantized conductance of $2\,e^2/h$. Other factors can, however, prevent dissipationless transport along the edges. A common picture is that an inhomogeneous Fermi energy position E_F throughout the sample creates so called charge puddles [130]. In these areas, the Fermi energy locally enters a bulk band. The topological edge states are then able to backscatter, which can prevent an ideally quantized conductance of $2\,e^2/h$. This led to the idea of a QSH edge channel interferometer, which would constitute an alternate method of proving edge channels. Initial attempts with physically dry-etched devices proved unsuccessful [131], so that wet-chemically etched antidot lattices in HgTe quantum wells were developed. An example of such an antidot lattice in a HgTe-based 2DTI is shown in Fig. 6.8.

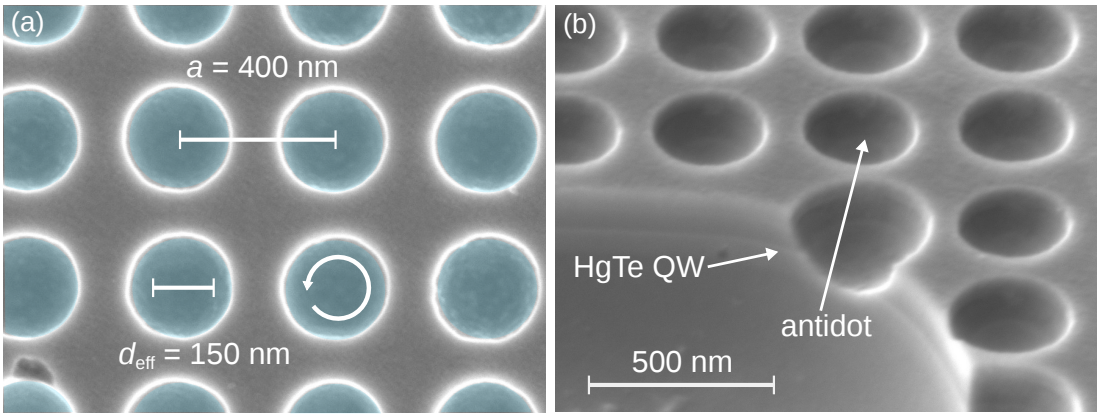

Figure 6.8: SEM-micrographs of an antidot lattice in an 8 nm HgTe quantum well in (a) a top-view and (b) at an angle of 50 °. Blue areas mark the etched antidots. The representative antidot lattice has a period of $a = 400$ nm, with an outer dot diameter of 290 nm. The wet-chemical etching leads to a round antidot profile. The effective diameter d_{eff} of the antidots at quantum well depth is roughly 150 nm, visible from the grey scale shading in the micrographs.

The underlying idea of such a device is to study helical edge channels through interference effects of closed edge channel loops that exist around each antidot. As in the Aharonov-Bohm effect in semiconductors rings (and the previously discussed 3DTI ring nanostructure in Sec. 6.1), a phase is picked up by closed trajectories when a magnetic field is applied perpendicular to the sample plane. In this design, the closed path is given by the QSH edge channels. The circular loops are assumed to connect with each other and the sample edge due to their close proximity. In addition, this method would do without non-local measurements [21] or exactly measuring the predicted quantized conductance of $2\,e^2/h$, which has proven cumbersome to reproduce since first being reported [7]. The antidot lattices are expected to also sport commensurable oscillations when trivial bulk band states are occupied.

Experimentally, the problem was approached by fabricating antidot lattices with 400 and 600 nm lattice constants in inverted and non-inverted HgTe quantum wells. The samples were fabricated on wafers with 8 nm (161027) and 5.7 nm (170322) HgTe layers, with mobilities in the range of $100 \cdot 10^3\,\text{cm}^2/\text{Vs}$ and $30 \cdot 10^3$ cm^2/Vs, respectively. The lower mobility in the 5.7 nm wafer is due to an overall degradation in thinner HgTe quantum wells. Respective mean free path lengths l_e in the two materials are 1 µm and 310 nm at $3 \cdot 10^{11}\,\text{cm}^{-2}$. The non-inverted quantum well has a trivial band structure and is intended as a reference experiment. The samples include standard insulating layers and a metallic topgate. The presented devices are part of a third generation of samples, after dry-etched antidots, measured by M. Otteneder [131], and a second attempt with wet-etched antidots did not show sufficiently clear signs of interferences.

Inverted quantum well

First, the devices in an inverted 8 nm HgTe quantum well will be discussed. The sample consists of a reference Hall bar and two antidot lattices with the mentioned lattice constants. Figure 6.9(a) shows the respective gate traces $\rho_{xx}(V_\mathrm{g})$ and charge carrier densities $n_s(V_\mathrm{g})$. An indication for the position of the gap can be found from the high resistive peaks at $V_\mathrm{g} = -2.3\,\mathrm{V}$ in the reference Hall bar and the 600 nm lattice. The behaviour of the 400 nm lattice is unexpected as the onset of the resistance peak, usually identified with the gap, already begins at $V_\mathrm{g} = 0.75\,\mathrm{V}$. Charge carrier densities n_s were obtained from measurements of the QHE (in the reference Hall bar) and SdH oscillations (in the antidot lattices). Charge carrier densities n_s in all three sections of the sample are in agreement, so that the intrinsic Fermi energy position is not noticeably influenced by the fabrication of antidots. Extrapolation of n_s confirms the gap position at $V_\mathrm{g} \approx -2.3\,\mathrm{V}$. It should be mentioned that the same gap position is found for the 400 nm lattice, which raises questions about the nature of the highly resistive regime.

At higher electron densities, commensurable oscillations are visible in the magnetoresistance of both antidot lattices. In this regime, CB electrons form a trivial spin-degenerate 2DES, so that the standard theory from experiments in GaAs quantum wells [74] is applicable. Figure 6.9(b) shows the magnetoresistance of the 600 nm lattice. The resistance peak shifting from 0.4 T to 0.3 T with lower V_g is identified as the fundamental peak, which corresponds to electron orbits around a single antidot. Higher order peaks are not found and likely suppressed due the limited mean free path length l_e. The presence of commensurate peaks

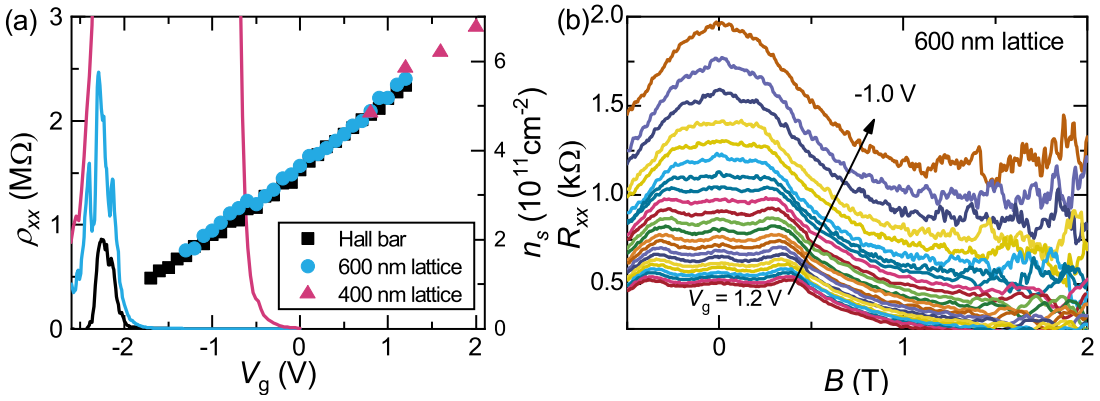

Figure 6.9: (a) Characterisation of antidot lattices and reference Hall bar in an 8 nm HgTe quantum well. The longitudinal resistivity ρ_{xx} and charge carrier density n_s is plotted as a function of gate voltage V_g for the two antidot lattices and the reference Hall bar. n_s was extracted from measurements of the QHE and SdH oscillations. (b) The longitudinal resistance R_{xx} of the 600 nm lattice is shown for gate voltages from $V_\mathrm{g} = -1.0$ to 1.2 V.

show that the periodic potential is well defined. At magnetic fields larger than 1 T, the onset of SdH oscillations is observed. The fundamental peak disappears completely for $V_g < -0.6\,\mathrm{V}$, which corresponds to roughly $2.7 \cdot 10^{11}\mathrm{cm}^{-2}$. In the 400 nm lattice (data not shown), the fundamental peak is suppressed sooner and remains visible only for $V_g > 0.5\,\mathrm{V}$. The charge carrier densities n_s, extracted from the fundamental peak position in both lattices, confirm values plotted in (a), and therefore also the gap position.

As mentioned above, a highly resistive regime is observed for gate voltages V_g associated with the conduction band in the 400 nm lattice. The same trend is visible in the 600 nm lattice, but in a much less pronounced form. The feature appears at increasing carrier densities n_s for decreasing lattice constants a. This makes the constrictions in between antidots a possible source. At low carrier density, these constrictions could be depleted to the point that they exhibit point contact behaviour. With this in mind, the current-voltage characteristics of the 400 nm lattice were investigated. The results are plotted in Fig. 6.10(a) for gate voltages near and inside the highly resistive state. The traces are linear deep in the CB, become strongly non-linear for V_g in the highly resistive regime, and once again flatten when the VB is reached at $V_g = -2.5\,\mathrm{V}$. In addition, QPC-like steps were observed in the longitudinal resistance. This feature was, however, only observed on the first cooldown of the sample and could not be reproduced in consecutive attempts. The steps are not quantized to expected resistance values of $R = h/ne^2$, which can be explained by the large array of point contacts connected in both parallel and series. The path of lowest resistance in such a configuration will therefore always include a number of point contacts in series that lead to

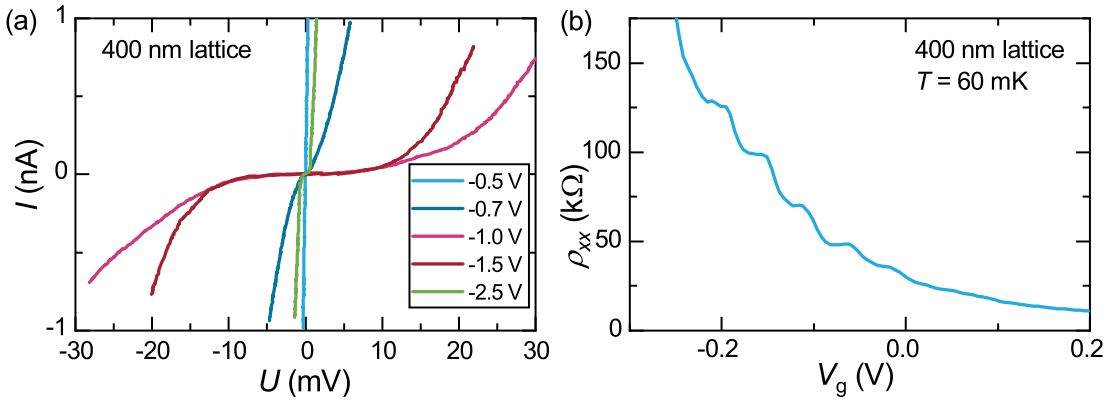

Figure 6.10: Point contact-behaviour in the 400 nm antidot superlattice. (a) Current-voltage characteristics of the antidot lattice for gate voltages on the beginning (−0.5 V, −0.7 V), middle (−1.0 V, −1.5 V) and end (−2.5 V) of the point contact regime. (b) $\rho_{xx}(V_g)$ as measured for a single cooldown only. Quantized steps are visible, but do not match values of quantized conductance. This is attributed to the large number of serial and parallel point contacts in the array.

resistances $> h/e^2$. It is therefore reasonable to conclude that the bottlenecks in the 2DES created by the antidots form a 2D array of point contacts if the charge carrier density n_s is sufficiently depleted by the topgate and the lattice constant a small enough. This interpretation is further corroborated by increases in the resistivity (compared to the reference Hall bar) by factors of 5 in the 600 nm lattice and 75 in the 400 nm lattice.

In search of interference effects, resulting from the chiral edge channels, the magnetoresistance at the onset of the pinch-off was investigated. Results from the 400 nm lattice will be discussed representatively, as the overall behaviour in the larger 600 nm lattice is qualitatively comparable. Traces are plotted in Fig. 6.11(a). At small magnetic fields ($B < 0.75\,\mathrm{T}$), distinct magnetoconductance oscillations with a period of about $\Delta B = 200\,\mathrm{mT}$ are present for all plotted V_g. At higher fields, amplitudes are suppressed and starting from 0.75 T

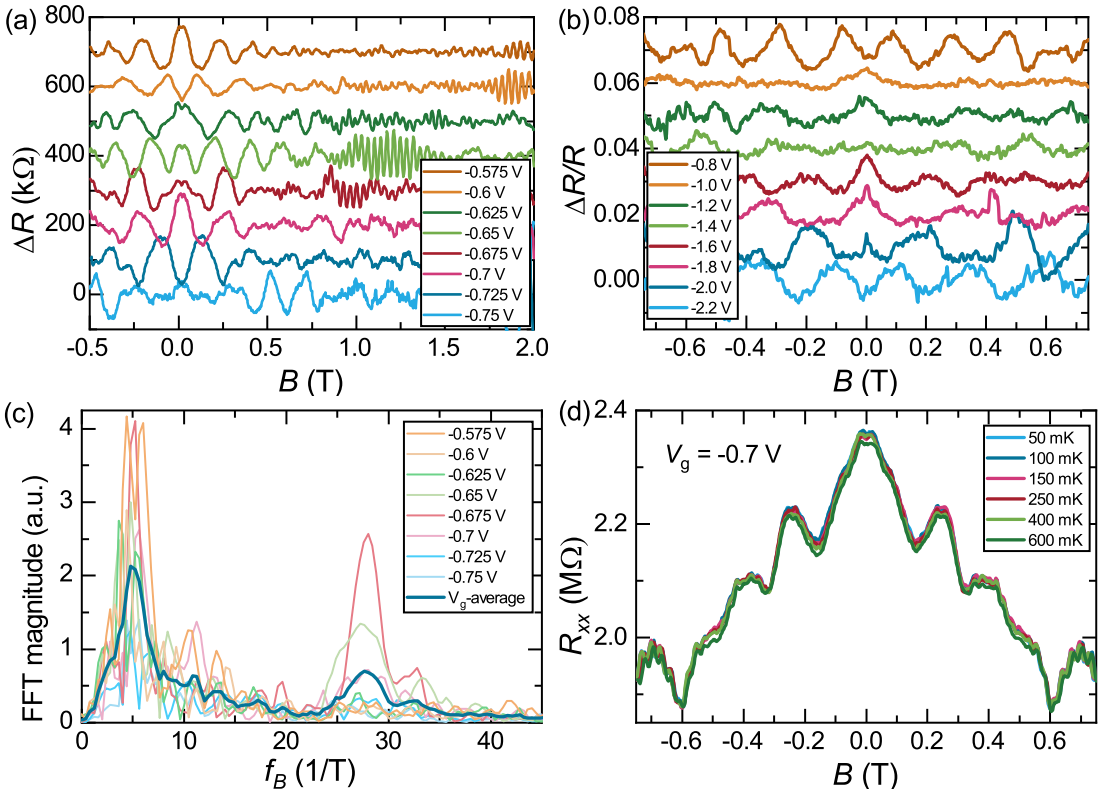

Figure 6.11: Interference effects in a 2DTI antidot lattice with $a = 400\,\mathrm{nm}$. (a) Magnetoresistance at the onset of pinch-off. Traces are offset for clarity. (b) Normalized magnetoresistance $\Delta R/R$ for V_g in the pinched off point contact and bulk gap regimes. (c) FFT spectra of the traces in (a) are shown, including a V_g-averaged trace. The maxima at $f_B = 5\,\mathrm{T}^{-1}$ and $27\,\mathrm{T}^{-1}$ correspond to the low- and high-frequency oscillations in (a). (d) Representative temperature dependence of the magnetoresistance at $V_\mathrm{g} = -0.7\,\mathrm{V}$.

higher frequency signals are visible for a number of gate voltages. The oscillations are present even when point contacts are pinched off ($V_g < -1.0\,V$) and the gap is reached. FFT spectra, calculated from traces in (a), are plotted in Fig. 6.11(c) along with the V_g-averaged spectrum. The two features with frequencies of $f_B = 5\,T^{-1}$ and $27.6\,T^{-1}$ correspond to h/e-periodic oscillations for closed paths around the perimeter of the antidots and around the non-depleted islands of 2DES remaining between each set of four antidots, respectively. Simulations have shown that such closed loops are possible and may contribute to the conductance [132]. While h/e-periodic oscillations for paths around antidots are also observed in the second lattice with 600 nm, the higher frequency features are present only in the 400 nm superlattice. The dependence of amplitudes on the temperature was also investigated for the gate voltage range shown in (a). An exemplary case for $V_g = -0.7\,V$ is plotted in Fig. 6.11(d). No change whatsoever in amplitudes could be found for temperatures up to 600 mK. It should be noted that h/e-periodic oscillations in an ensemble of phase coherent ring structures is highly unusual. In an array that is larger than the phase coherence length l_ϕ, the h/e-periodic contributions are expected to average out. As discussed in Sec. 3.2.3, only $h/2e$-periodic AAS oscillations should remain. This may be a consequence of the helical edge channels in 2DTIs but can not be conclusively shown from the present data.

Non-inverted quantum well

The tunability of HgTe quantum wells from the topological to the trivial regime by means of the quantum well thickness makes a controlled reference experiment possible. Identical antidot lattices are patterned in a non-inverted 5.7 nm thick HgTe quantum well. The sample consists of a Hall bar and two antidot lattices with the same lattice constants of 400 and 600 nm. The devices were characterized in the same manner as the inverted sample. The longitudinal resistance $\rho_{xx}(V_g)$ and charge carrier densities n_s are plotted in Fig. 6.12(a). Extrapolation of n_s allows an estimation of the lower CB edge at $V_g \approx -1\,V$. Unlike in the previous device, tuning E_F through the gap into the VB was not possible. As in experiments with the inverted quantum well, the resistivity of the antidot lattice increases significantly for low n_s. Here, the effect of pinched off point contacts is seen in both the 400 and the 600 nm lattice. The effect is more moderate, compared to the inverted sample, which is in line with the lower increases in resistivity. Compared to the reference Hall bar, the resistivity increases by factors of roughly 3 in the 600 nm and by 9 in the 400 nm lattices. This is not surprising, because the effect is assumed to stem from a depletion of bulk 2DES states in the constrictions between antidots and does not rely on features of an inverted band structure.

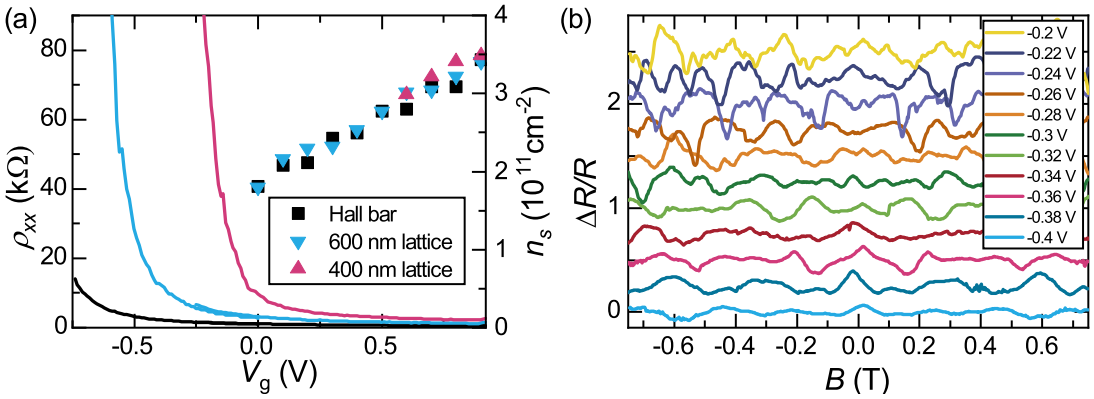

Figure 6.12: Characterisation and interference effects of the reference sample in a 5.7 nm HgTe QW. (a) ρ_{xx} and $n_s(V_g)$ of two antidot lattices and a Hall bar. $\rho_{xx}(V_g)$ deviates at higher n_s for smaller lattice constants, due to point contacts being pinched off. Charge carrier densities n_s, extracted from QHE and SdH measurements, coincide for patterned and unpatterned devices. (b) Normalized magnetoresistance $\Delta R/R$ of the trivial 400 nm antidot lattice at V_g from -0.2 V to -0.4 V. Curves are offset for clarity.

The hypothesis for this experiment was that chiral edge channels around the antidots pick up a phase in magnetic fields and lead to magnetoresistance oscillations. Such oscillations should therefore only be visible in inverted quantum wells. However, the magnetoresistance of investigated antidot lattices in the non-inverted reference sample show similar behaviour. Traces recorded in the region of point contact pinch off are plotted in Fig. 6.12(b) and exhibit signs of h/e-periodic features. Although they are not as pronounced and clear as in the topological antidot lattices, they are undoubtedly present. Temperature-dependent measurements show unchanging amplitudes up to 600 mK, in both the inverted and non-inverted cases. These observations make an attribution to QSH edge channels difficult as they contradict the initial assumption, that an Aharonov-Bohm effect in antidot lattices is only possible with chiral edge channels when the Fermi energy E_F is in the gap. They also raise questions about the mechanisms behind the observed oscillations and role, or lack thereof, of chiral edge channels.

7

Topological nanowires

In this chapter, experiments on nanowires fabricated from strained 80 nm HgTe thin films are presented. First, an overview of investigated nanowires is given in Sec. 7.1. Initial transport experiments under in-plane magnetic fields are presented in Sec. 7.2 with a focus on the phase-coherence length of the topological surface states. Chapter 7.3 highlights the predicted transport signatures in topological HgTe nanowires. Next, the 1D subband structure is probed for proof of topological surface states via magnetoconductance and subband-induced oscillations in Sec. 7.4. A simple electrostatic model is used to quantitatively differentiate between spin-resolved and spin-degenerate states. A discussion of possible errors in the application of the model is presented in Sec. 7.5. In Sec. 7.6, the theoretical background of the non-ideal geometry is discussed, while Sec. 7.7 presents further experiments with ensembles of parallel nanowires. Chapter 7.8 deals with the Hall effect, QHE and SdH oscillations in out-of-plane field configuration measurements. Finally, attempts towards quantum point contacts are discussed in Sec. 7.9.

The results in Chapters 7.2 through 7.6 have been published in Ref. [31].

7.1 Initial considerations

For the sake of simplicity, nanowires are typically described in theory with a radially symmetric cross sections [64, 87]. Although, their real geometry depends on fabrication methods. While carbon nanotubes are radially symmetric [133] and some core/shell nanowire systems exhibit a hexagonal structure [134, 135], nanowires etched from thin-films in a top-down approach are far from having a highly symmetrical cross section. Wet-chemical etching further complicates the geometry by introducing slanted sides and a varying width along the wire axis. A typical example of a wet-etched strained HgTe nanowire is shown in Fig. 7.1. The wet-chemical process is largely isotropic, so that rounded corners are unavoidable. All nanowire devices are fabricated from capped 80 nm strained HgTe thin films.

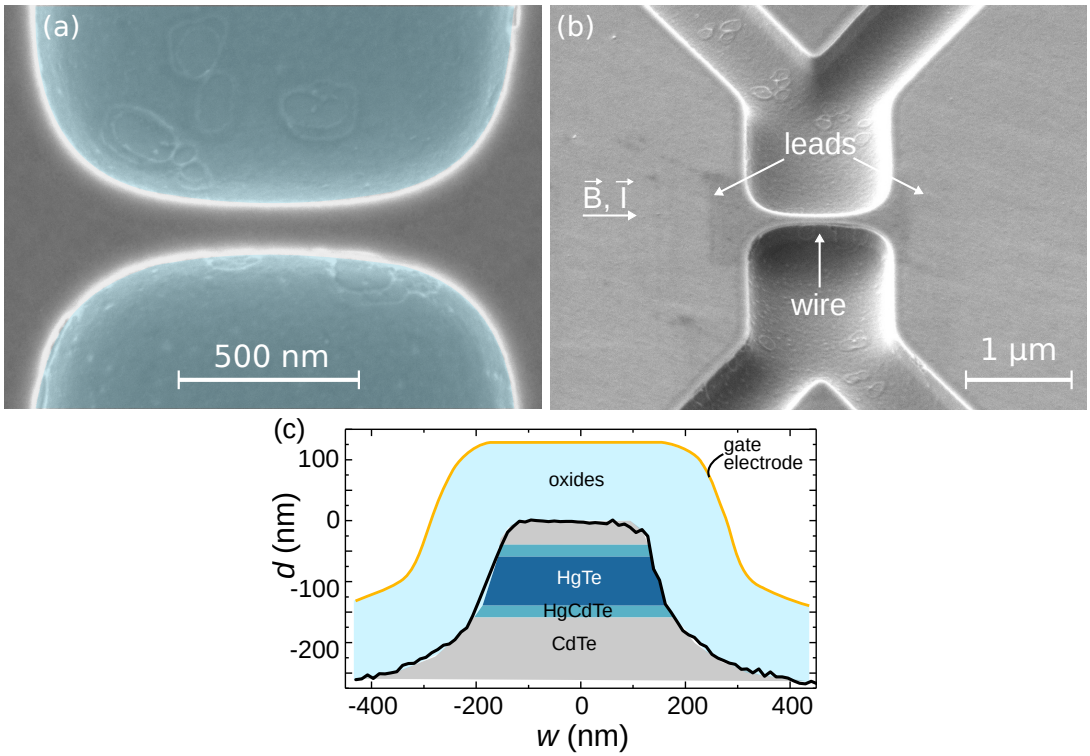

Figure 7.1: SEM-micrographs of nanowire device s38w2 from (a) above and (b) at a tilt angle of 50 °. The nanowire has a length of $l = 1.3\,\mu\text{m}$ and a median width of $\bar{w} = 163\,\text{nm}$ at its most narrow point. (c) Schematic cross section of a wet-chemically etched nanowire. The sketch is based off of an AFM profile (black line) and known layer thicknesses from MBE-growth.

A detailed description can be found in Sec. 4.1, characterization measurements in App. A.2.

A schematic of a typical cross section is shown in Fig. 7.1(c), which is modelled from an AFM profile (black line) of a nanowire before deposition of the gate oxides. The layers of the heterostructure are colour coded. The cross section of the HgTe layer is visibly affected by the slanted side surfaces and as a result is nearly trapezoidal. The top-view profile exhibits rounded corners. Exact measurements of the wire widths are taken from SEM-micrographs, such as in Fig. 7.1(a). The width of the top HgTe surface is measured at the wires' most narrow section. The position at the bottom surface is visible from the colour gradient at the $Cd_{0.7}Hg_{0.3}Te$/HgTe interface in tilted SEM-micrographs, such as Fig. 7.1(b). Measurements of both widths are necessary, as the cross-sectional areas A deviate significantly if only the top is taken into account. From these measurements a median width $\overline{w}$ is calculated, meaning that the cross section is approximated by a rectangle.

Table 7.1: Essential geometrical parameters of the investigated nanowires. The height of all wires is given by the 80 nm thick HgTe layer. The median width and length of the wires are denoted by $\overline{w}$ and l. The wire circumference P and the expected period for ϕ_0 periodic oscillations $\Delta B_{h/e}$ were computed for topological surface states residing 5 nm below the HgTe interface.

device	$\overline{w}$ (nm)	l µm	P (nm)	$\Delta B_{h/e}$ (T)
s38w1	310	1.33	740	0.197
s38w2	163	1.33	446	0.386
s39w2	600	1.33	1320	0.100
s39w1	990	1.33	2100	0.060
s48w1	178	1.06	476	0.351
s48w2	294	1.95	708	0.208
s48w3	287	2.97	694	0.212
s53w1	265	1.0	650	0.232
s53w2	287	1.5	694	0.213
s53w3	283	2.0	686	0.216
s58w1	150	0.7	420	0.422
s58w2	230	0.7	600	0.257

In this simplified model of the cross section, the area A is unchanged while the circumference P deviates slightly from the physical value. The error in P from the trapezoidal circumference P_{tra} is typically within 3 %. The consequences of this simplification on analysis are discussed in Sec. 7.5. While the calculated value for the expected period of AB-oscillations $\Delta B_{h/e}$ is not affected by this approximation, it is modified by the assumption that topological surface states are located several nanometres within the bulk. Typically, values of up to 10 nm are assumed in literature [52, 55]. A value of 5 nm falls well within this range and is assumed for all devices in Table 7.1.

The wet-chemical etching process brings other constraints like rounded profiles with it, which influenced the sample design. On the one hand, the nanowires were planned to be long enough so that a constant cross section is present for a portion of the constriction, seen in Fig. 7.1(a). On the other hand, the devices need to be shorter than the elastic mean free path length l_e of $2 - 3$ µm in the 80 nm strained HgTe wafers so that transport is at least in the quasi-ballistic regime. With this in mind, devices with lengths l of 1 to 3 µm were initially built. Later, shorter constrictions with lengths of 400 nm were fabricated. They are discussed in Sec. 7.9.

7.2 Phase-coherence length

Initial measurements on nanowire constrictions focused on the extraction of the phase-coherence length l_ϕ to gain an understanding of the transport regime, i.e. if transport is phase coherent. Additionaly, dominating h/e-oscillations ($h/2e$) would indicate ballistic (diffusive) transport in the nanowire [64]. Figure 7.2(a) shows the conductance G as a function of a magnetic field B along the nanowire axis for temperatures between 40 to 300 mK. The traces show a clear h/e-periodicity, indicated by the horizontal bar. This hints at non-diffusive transport, where the elastic mean free path l_e is on the order of the wire length and larger than the wire circumference P. The conductance $G(B)$ is expected to exhibit a $h/2e$-periodicity in the diffusive limit [64]. The fact that conductance fluctuations are also visible in Fig. 7.2(a) shows that residual disorder scattering is present in these nanowire structures. By analysing the temperature dependence of $G(B)$, the phase coherence length l_ϕ can be extracted from the decay of the oscillation amplitude ΔG. For ballistic transport, an exponential decay is expected [80],

$$\Delta G \propto exp\left(-\frac{P}{l_\phi(T)}\right). \tag{7.1}$$

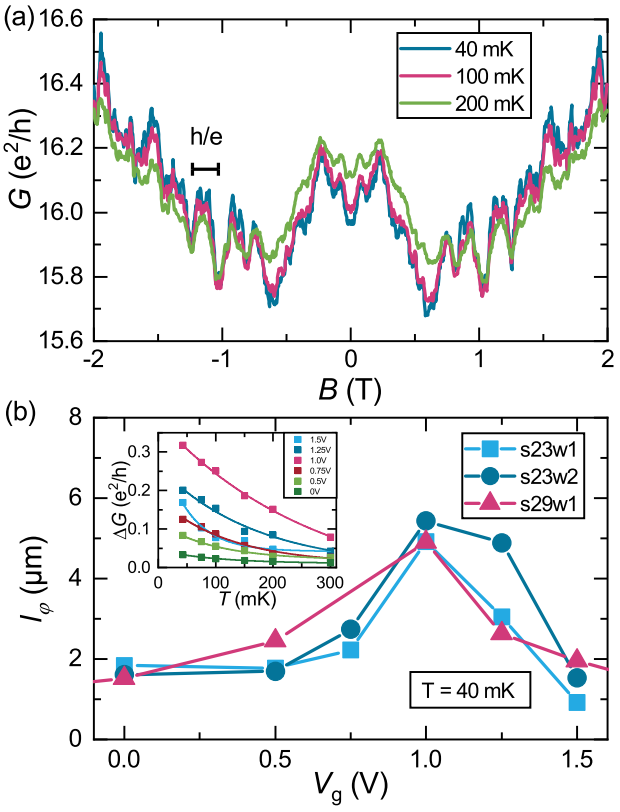

Figure 7.2: (a) Magnetoconductance oscillations from nanowire s23w1 taken at different temperatures T. The h/e-periodicity $G(B)$ is indicated by the black bar, while the amplitudes $\Delta G(T)$ decrease exponentially with increasing temperature T. $\Delta G(T)$ of device s23w1 is shown for a number of gate voltages V_g, along with their respective fits, in the inset of (b). The main part of panel (b) shows the gate voltage dependence of the phase coherence length $l_\phi(V_g)$ for devices s23w1, s23w2 and s29w1.

Such temperature dependent measurements were carried out on three devices. The resulting phase-coherence lengths l_ϕ are plotted as a function of V_g in Fig. 7.2(b). For all investigated samples, l_ϕ takes minimal values in the range from 1 to 2 µm. Maximum values go beyond 5 µm and are found for gate voltages of $V_\mathrm{g} = 1\ V$, which corresponds to a Fermi level position E_F in the bulk energy gap. The gap position is in agreement with measurements on macroscopic Hall bars made from the same material, cf. Refs. [51], [25], or App. A.2 of this work. Enhanced phase coherence lengths l_ϕ for E_F in the bulk gap are in line with expectations, as backscattering is reduced and scattering into bulk states is not possible.

7.3 Magnetoconductance oscillations

While the previous chapter shows that the surface states indeed produce coherent states around the circumference of the nanowires, here the experimental signatures, predicted by Bardarson *et al.* [64, 91] and discussed in Sec. 3.3.1, are investigated. The analysis shown in this section was carried out for a number of devices, but is presented representatively for nanowire s38w1. Further data sets are included in App. A.3 to A.5 and show consistent behaviour. The data, shown in Fig. 7.3, was treated with the following methods: The small hysteretic behaviour of the superconducting magnet around $B = 0$ was removed from the conductance $\Delta G(B)$ first. Next, a smoothly varying background $G_\mathrm{sm}(B)$ was subtracted using a Savitzky-Golay filter [136], such that only frequencies smaller than $f_B = 0.5/\phi_0$ are cut off. The resulting conductance correction $\Delta G(V_\mathrm{g}; \phi)$ is shown as a colour plot in Fig. 7.3(a). The data set was recorded with a gate voltage spacing of $\Delta V_\mathrm{g} = 0.01\,\mathrm{V}$. The corresponding data from device s38w2, treated in the same way, is shown as a selection of single magnetoconductance traces for larger magnetic fluxes in Fig. 7.3(b). The data exhibits dominant ϕ_0-periodic oscillations, as well as a distinct switching behaviour along lines of constant flux. The rhomboid structure, which results from the phase switching, will be analysed in the next section.

The h/e-periodicity is verified by fast Fourier transform analysis. The FFTs were computed using a Chebyshev window and an averaging method, where the magnetoconductance trace is split into sections. The final result is an average of the separate sections' FFTs. The procedure is discussed further in App. C. For this purpose, a data set of magnetoconductance traces up to $20\,\phi_0$ was recorded in the case of device s38w1 to improve FFT accuracy. The period of the oscillations is expected to be independent of the gate voltage V_g, which justifies an average over all FFT spectra. Figure 7.4 shows the V_g-averaged FFT in units of $1/\phi_0$ for device s38w1. The spectrum exhibits a distinct peak in the frequency range near

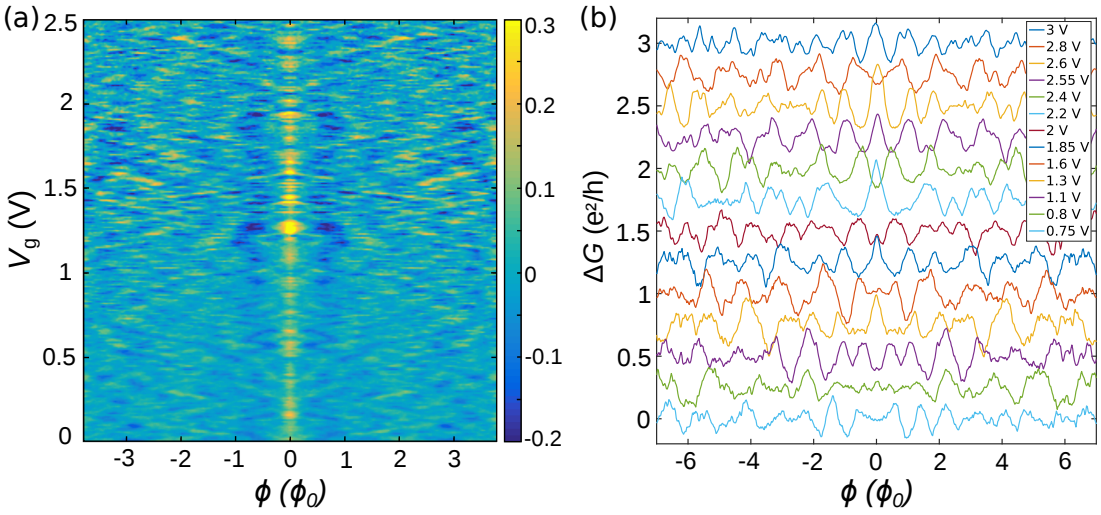

Figure 7.3: Quantum conductance corrections of a strained HgTe topological nanowire. (a) Conductance correction as function of magnetic flux and gate voltage $\Delta G(V_g; \phi)$ in units of e^2/h from device s38w1 shown as a colour plot. The data set shows a rhomboid structure that results from the ϕ_0-periodicity and switching of the AB phases with V_g. (b) A selection of representative magnetoconductance curves from device s38w2, covering a flux range of $\pm 7\phi_0$, is shown. The traces are offset for clarity and exhibit clear h/e-periodic behaviour, as well as a switching of the phase with varying V_g.

$1/\phi_0$. The magnetic flux through the ring is calculated from the magnetic field B and cross section A, $\phi = BA$. As discussed in Sec. 7.1, the area of the cross section A is calculated using a square approximation of the trapezoidal geometry. In the case of device s38w1, the median width of 310 nm was used along with the assumption that the topological surface states are located 5 nm below the HgTe interface. This general assumption is the result of calibrations of the nanowire dimensions using V_g-averaged FFT spectra. The spectra were calculated as a function of the frequency in the magnetic field f_B. From the resulting h/e-peak, an effective cross sectional area A_{eff}, and effective width and height, can be determined via $\phi_0 = BA = Bwh$. Analysis of multiple devices shows that the effective cross section A_{eff} is consistently smaller than the physical dimensions for all investigated devices. The effect corresponds on average to surface states lying roughly 5 nm within the HgTe bulk, with deviations of some nanometres from wire to wire. This interpretation is justified by theoretical calculations (Supplemental of Ref. [55]), which place the centre of the surface state wave function up to 10 nm below the interface. The resulting peak in Fig. 7.4 is located at $0.87/\phi_0$ and falls well within the expected region for an h/e-periodic signal. Here, the lower bound is given by the geometrical dimensions of the nanowire cross section and the upper bound is calculated for the case where the wave function of the surface states lies 8 nm within the wire.

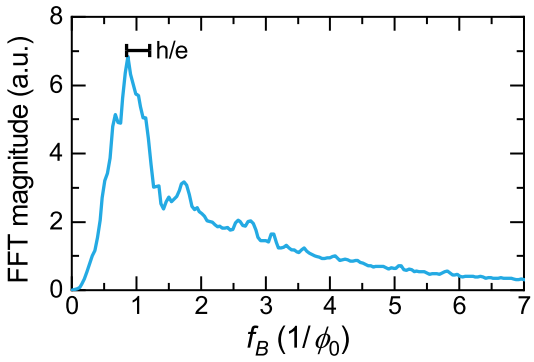

Figure 7.4: V_g-averaged fast Fourier spectrum calculated from nanowire magnetoconductance oscillations of device s38w1, with a distinct peak near to $1/\phi_0$. The black bar denotes the expected range of the peak to occur for the given wire geometry.

Typical amplitudes of conductance corrections are between $0.1 - 0.3\,e^2/h$ and thus smaller than the predicted value of a e^2/h [64]. This is on the order of other experimental studies of topological nanowires. Amplitudes of less than $0.05\,e^2/h$ in Bi_2Te_3 nanowires [28], $0.1 - 0.2\,e^2/h$ in Bi_2Se_3 wires [137, 138], and roughly $0.5\,e^2/h$ in $Bi_{1.33}Sb_{0.66}Te_3$ wires [27] have been reported. The deviation from the expected value is attributed to the device geometry and remnant disorder, which leads to backscattering. Since observed oscillations are predominantly ϕ_0-periodic, instead of $\phi_0/2$, it can be assumed that transport is at least quasi-ballistic. The effects of disorder are considered in transport simulations in Sec. 7.6 and discussed further for topological nanowires in Ref. [139].

Another consequence of disorder is a WAL-contribution, which is superimposed on the oscillatory signal around zero magnetic field. The effect is predominantly visible in longer wires, with a decrease of effect amplitudes towards shorter nanowires. Devices with $l_e < l$ are not in the ballistic regime, so that disorder induced scattering plays a role. In wet-etched nanowires with $l < 1.5\,\mu m$, which are the focus of this work, WAL is therefore mostly suppressed. In longer wires, as well as dry-etch devices[1], WAL contributions are found to dominate the signal around $B = 0$.

7.4 Subband-induced conductance oscillations

The transport signatures predicted for topological nanowires in a magnetic field parallel to the nanowire axis are discussed in Sec. 3.3.1. They are ϕ_0-periodic magnetoconductance oscillations, a switching of the phase as a function of gate voltage V_g and a perfectly transmitting mode at $\phi/\phi_0 = 0.5$. Some or all of these features have been observed in a number of material systems, such as Bi_2Te_3 [28], Bi_2Se_3 [30, 137], $Bi_{1.33}Sb_{0.66}Te_3$ [27] and HgTe [29]. The h/e-periodic oscillations by themselves are, however, not proof that the system is topological, but only

[1] See work by S. Weishäupl (2014) [29].

that transport is surface dominated. The non-trivial origin of the band structure can be shown by detecting the topologically protected linear mode as reported for Bi_2Se_3 in Ref. [30]. The Dirac point of strained HgTe and other 3DTI systems is however located in the valence band, so that the linear mode cannot be singled out for transport. And without direct access to the quantized conductance of the linear mode, the Aharonov-Bohm oscillations and V_g-dependent phase switching alone are insufficient proof of the topological nature of the nanowires surface states. While the first two features have been discussed in the previous chapters, the crucial question remains how to distinguish between topological and trivial surface states in 3DTI nanowires with an inaccessible Dirac point. The fact that every switching event of the Aharonov-Bohm phase, i.e. every transition from minimum to maximum at $\phi = 0$, is associated with the opening of another subband gives experimental access to the subband structure.

A quantitative analysis of the expected $\Delta G(V_g)$-oscillations requires a highly resolved data set, a careful extraction of data, as well as a model for a quantitative comparison. Although the sought after information is the V_g-dependence of the conductance correction ΔG, a direct measurement of $\Delta G(V_g)$ has proven unsuccessful. The reason is the background in $G(V_g)$, which is large in comparison to the conductance corrections and makes it difficult to remove $\Delta G_{sm}(V_g)$. Extracting the oscillations becomes a much simpler procedure when measuring $G(B)$, which was done with a resolution of $\Delta V = 0.01\,\mathrm{V}$ between magnetoconductance curves. Background subtraction of $G_{sm}(B)$ was performed in the same manner as mentioned in Sec. 7.3 and discussed further in App. C. The conductance $\Delta G(V_g)$ is then extracted via line cuts taken from the data set in Fig. 7.3(a) at integer and half-integer values of ϕ/ϕ_0. An average over all positive and negative integer multiples of ϕ_0, i.e. $\pm\phi_0, \pm 2\phi_0$ and $\pm 3\phi_0$ for device s38w1, is calculated to suppress the influence of aperiodic conductance fluctuations. The result is the blue curve in Fig. 7.5(a). Accordingly, the orange curve is calculated by averaging the line cuts at positive and negative half-integer multiples, i.e. $\pm 0.5\phi_0, \pm 1.5\phi_0$ and $\pm 2.5\phi_0$. The line cut at $\phi = 0$ was omitted due to a WAL-like background profile that makes subtraction difficult.

The two resulting traces $\Delta G(V_g)$ display antiphase oscillations as expected. Each minimum of $\Delta G(V_g)$ corresponds to a Fermi level at the edge of a subband since the corresponding higher density of states causes enhanced scattering. For this reason, the gate voltage distance ΔV_g between two minima can be mapped to the subband spacing. The conductance oscillation spacing is extracted by marking pairs of matching minima in $\Delta G(V_g; (j + 0.5)\phi_0)$ and maxima in $\Delta G(V_g; j\phi_0)$, thus making use of the anticorrelation between integer and half-integer fluxes. Each pair is assigned an arbitrary integer subband index $N - N_0$. To increase accuracy further, the corresponding pairs of maxima in $\Delta G(V_g; (j + 0.5)\phi_0)$ and minima in $\Delta G(V_g; j\phi_0)$ are assigned a half-integer subband index. The subband index is inevitably relative in nature as the precise number of filled subbands N_0

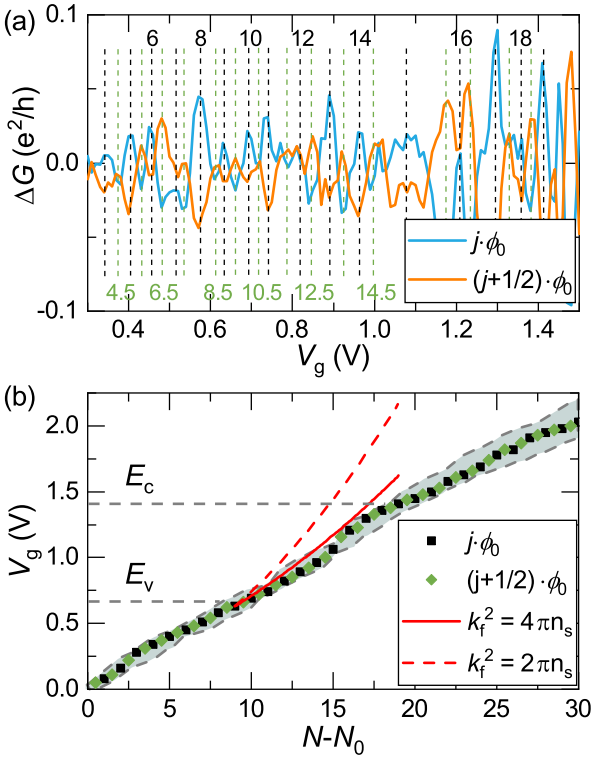

Figure 7.5: Analysis of subband induced magnetoconductance oscillations. (a) Conductance correction ΔG as a function of V_g for integer (blue) and half-integer (orange) values of ϕ/ϕ_0. The traces were obtained by averaging line-cuts along constant ϕ_0 from the data shown in Fig. 7.3(a). Pairs of matching minima and maxima in the anti-correlated traces are marked by vertical dashed lines and assigned a subband level index $N - N_0$. (b) The gate voltage position of the conductance maxima from (a) as a function of index N (with an arbitrary offset N_0). The grey area behind the data points contains the deviation of the subband positions when introducing an error of up to $\pm 20\,\%$ in the calculation of ϕ_0. For a more in depth discussion see Sec. 7.5.

at the reference gate voltage V_0 is unknown for systems with a Dirac point in the VB.

The relation between the nanowire band structure and $\Delta G(V_g; \phi)$ can be made by using the relation of a single effective carrier density n_{eff} to its capacitance C_{eff}[2],

$$(n_{\text{eff}} - n_0)\, e = C_{\text{eff}}(V_g - V_0), \tag{7.2}$$

where V_0 is the reference gate voltage and n_0 the corresponding carrier density. The use of an effective carrier density and capacitance will be justified in Sec. 7.6. The Fermi wave vector k_F is given by

$$k_F = \sqrt{(4\pi/g_s) n_{\text{eff}}} \tag{7.3}$$

with the spin degeneracy factor $g_s = 1$ for spin-resolved TSS and $g_s = 2$ for spin-degenerate trivial surface states. Taking into account the constant subband splitting $E/(\hbar v_F) = \Delta k_l = 2\pi/P$, the Fermi wave vector at a subband opening can be written as

$$k_F = k_0 + (N - N_0)\Delta k_l \text{ with } k_0 = \sqrt{(4\pi/g_s) n_0}. \tag{7.4}$$

[2]Capacitances are given per area in units of F/m^2 in this work.

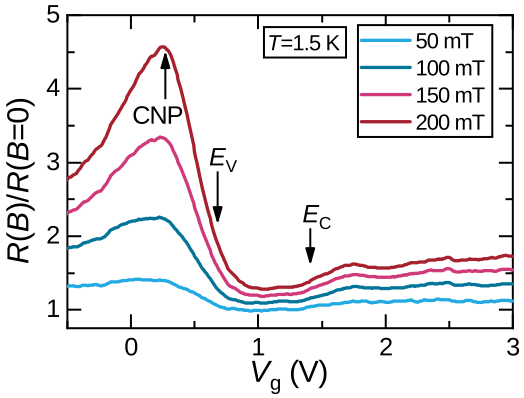

Figure 7.6: Normalized longitudinal resistance plotted against the gate voltage for device s38w1. The upper and lower bounds of the bulk band gap and the position of the CNP are indicated by arrows and were determined by comparison to experiments with the same material [51].

By combining the equations 7.2, 7.3, and 7.4, the relation between gate voltage and subband level index N reads,

$$V_\mathrm{g} - V_0 = \frac{g_s e}{4\pi C_\mathrm{eff}} \left[2k_0(N - N_0)\Delta k_l + (N - N_0)^2 \Delta k_l^2 \right]. \tag{7.5}$$

It shows that the distance between two conductance minima, when tuning V_g, is defined by the effective capacitance C_eff and the wire circumference P, as $\Delta k_l = 2\pi/P$.

Since Eq. 7.5 is derived for a single charge carrier type, the model is only valid when V_g is located in the bulk energy gap. Outside the gap, bulk electrons or holes with different degeneracy factors contribute to transport and the Fermi wave vector k_F of the system becomes unclear. The location of the gap must be determined before applying Eq. 7.5 to the data in Fig. 7.5. Its position can be estimated from a general wafer characterization, such as in App. A.2, but due to minor shifts, it should be confirmed by measurements of the investigated sample. Here, the V_g-position of the gap is determined from gate traces of nanowire s38w1 at different magnetic fields. The curves, shown in Fig. 7.6, are normalized to their $R(B = 0)$ values. The resistance maximum, which becomes clearer in small magnetic fields, is usually ascribed to the charge neutrality point (CNP) [51]. The valence and conduction band edges are obtained through comparison to experiments with macroscopic Hall bars on the same wafer published in Refs. [25, 51]. The band edges are obtained from the increases magnetoresistivity from coexisting carrier types at these points in the band structure. They are indicated by arrows at $V_\mathrm{g}^{E_\mathrm{v}} = 0.65\,\mathrm{V}$ and $V_\mathrm{g}^{E_\mathrm{c}} = 1.4\,\mathrm{V}$, respectively, in Fig. 7.6.

Before applying Eq. 7.5 to the extracted data in Fig. 7.5, the effective capacitance C_eff of the system is required. In macroscopic devices, it is possible to experimentally extract the capacitance from $n_s(V_\mathrm{g})$ with Eq. 7.2. However, this is not possible in mesoscopic 3DTI nanowires as the contribution from side surfaces becomes significant and the 1D confinement disturbs the LL structure. For a more in depth discussion see Sec. 7.8. Instead, numerical calculations of the

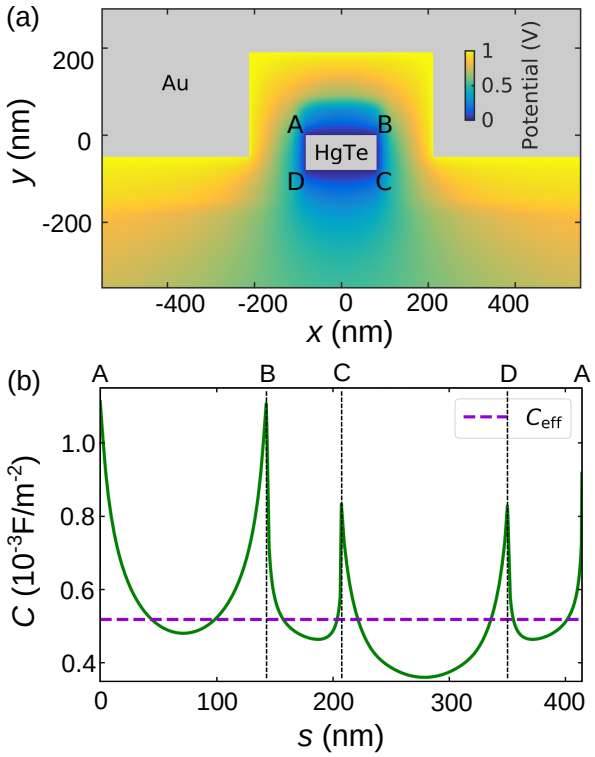

Figure 7.7: Numerical simulation of the capacitance for nanowire device s38w2 (adapted from [31]). (a) Electrostatic potential $u(x, y)$ in the plane of the nanowire cross section. (b) Capacitance profile $C(s)$ along the perimeter of the nanowire obtained from (a). The effective capacitance is given by $C_{\text{eff}} = \langle\sqrt{C(s)}\rangle^2$. An analogous simulation for device s38w1 yields $C_{\text{eff}} = 3.897 \cdot 10^{-4}\,\text{F/m}^2$.

capacitance C_{eff} were provided by M.H. Liu [31]. The partial-differential equation (PDE) solver FEnICs [140] was used to numerically solve the Poisson equation. The model includes the full stack of the heterostructure as well as the oxide layers. Dielectric constants of $\epsilon_r = 3.5$ for the 30 nm SiO_2 layer and $\epsilon_r = 9.1$ for the 100 nm Al_2O_3 layer were used [141]. For $Hg_{0.7}Cd_{0.3}Te$ and CdTe cap layers of dielectric constants of $\epsilon_r = 13.0$ and $\epsilon_r = 10.2$, respectively, were used [142, 143]. A comparison of the experimentally determined filling rate $C/e = \partial n_s \partial V_g$ with a filling rate calculated with a simple plate capacitor model verifies these assumptions. The model yields a theoretical filling rate of $2.29 \cdot 10^{11}\text{cm}^{-2}\text{V}^{-1}$, while experimental values of $2...2.25 \cdot 10^{11}\text{cm}^{-2}\text{V}^{-1}$ are common [see App. A.2]. For the presently discussed device, an experimental value of $2.00 \cdot 10^{11}\text{cm}^{-2}\text{V}^{-1}$ was extracted. The electrostatic simulation models the surface states as metallic surfaces instead of accounting for a contribution of the quantum capacitance [144]. For a more in depth discussion that justifies this choice, see Sec. 7.5.

The filling rate along the wire perimeter $C(s)$ is calculated from the gradient of the electric potential $u(x, y)$, shown in Fig. 7.7, as simulated by the numerical PDE solver. The resulting capacitance profile is plotted in Fig. 7.7(b), along with its mean value of C_{eff}. For the representatively discussed nanowire s38w1, a value of $3.987 \cdot 10^{-4}\,\text{F/m}^{-2}$ was computed.

With all quantities available, the derived model can be applied to the extracted conductance oscillations. The curves for the spin-resolved and spin-degenerate

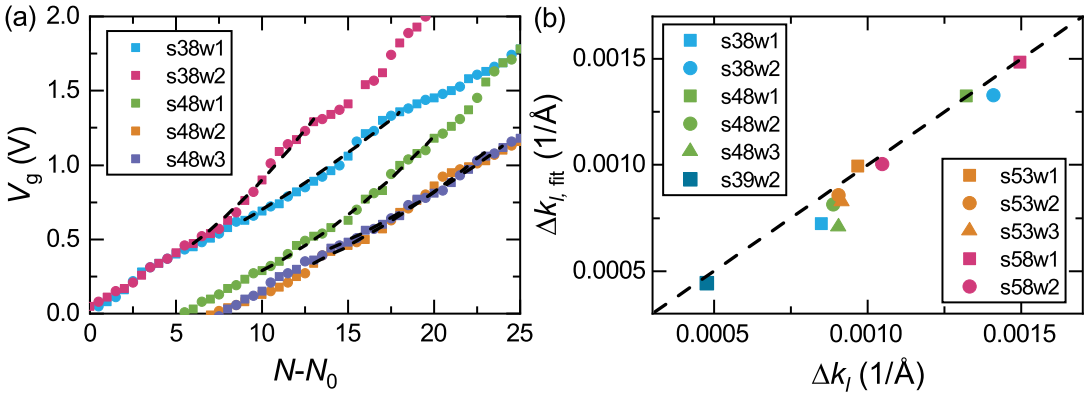

Figure 7.8: Analysis of the subband spacing. (a) $V_g(N - N_0)$ dependencies for all devices investigated in in-plane fields with their respective best fits based on Eq. 7.5 within the bulk band gap. Δk_l was the only fit parameter. Integer $N - N_0$ are shown as squares, half-integer as circles. In (b), the best-fit values of $\Delta k_{l,\mathrm{fit}}$ are plotted against the $\Delta k_l = 2\pi/P$, calculated from the wire circumference P as determined from SEM-micrographs. The dashed lines marks the ideal case of $\Delta k_{l,\mathrm{fit}} = \Delta k_l$.

cases, shown in Fig. 7.5(b), were calculated from Eq. 7.5 with V_0 and N_0 set to the values at the VB edge. In the case of nanowire s38w1, $V_g^{E_v}$ is found to be at 0.65 V, leading to $N_0 = 9$. In the gate voltage interval of the bulk gap, the data is best described by the model for spin helical surface states (solid lines). The model for trivial surface states (dashed line), which yields a steeper slope due to spin-degeneracy, fails to describe the experimental data. The approximation of the nanowire cross section as a square introduces a small error in the calculation of the circumference P. This error is shown to be negligible, when trying to distinguish between helical and trivial surface states, by applying the spin-resolved model with the circumference of the trapezoidal geometry P_{tra} (solid blue line).

The analysis was carried out for a number of devices with different cross sections A. These include different lengths l, as well as different substrates. Data from wires built from (100)-oriented substrates are shown in App. A.4. For a comprehensive list see Table 7.1 in Sec. 7.1. For each device the circumference P, which defines the subband splitting $\Delta k_l = 2\pi/P$, was extracted from the SEM-micrographs. Additionally, the nanowire circumference P can be extracted by fitting the data points. The best fits of the spin-resolved model, in their respective bulk gap regions, are shown in Fig. 7.8(a) for the first five investigated devices. Using their respective effective capacitances C_{eff}, experimental values for $\Delta k_{l,\mathrm{fit}}$ can be calculated. Figure 7.8(b) shows the extracted $\Delta k_{l,\mathrm{fit}}$ plotted versus Δk_l for all analysed nanowires with widths up to $\bar{w} = 600$ nm. The largest nanowire s39w1 ($\bar{w} = 990$ nm) is not included due to diminishing oscillation amplitudes, which in turn does not allow for reliable analysis. The plot shows that data points follow $\Delta k_l = \Delta k_{l,\mathrm{fit}}$, which confirms that the method of analysis is

appropriate.

7.5 Discussion of possible sources of error

The method of analysis from the previous chapter crucially relies on a quantitative comparison. Therefore, a closer look has to be made into the accuracy of quantities critical to the analysis, such as the calculation of the magnetic flux quantum ϕ through the wire, the VB edge position $V_g^{E_v}$, the simulated capacitance C_{eff}, and the circumference P. The question is, for example, how would errors in the determination of the band extrema positions and the nanowire dimensions, and consequently the magnetic flux ϕ/ϕ_0, influence the conclusions drawn from the model fits?

The analysis of subband level positions could depend significantly on the value of ϕ_0, as it determines where the line cuts are taken. To determine if it influences the conclusions drawn from the data, the analysis from the previous chapter is repeated with artificial deviations from ϕ/ϕ_0 of up to $\pm 20\,\%$. The ϕ-scale on Fig. 7.3(a) is recalculated with the deviation, line cuts at integer and half-integer multiples are extracted and the positions of subband levels are determined as before. The resulting data points are plotted in Fig. 7.9(a) for deviations in ϕ/ϕ_0 of $20\,\%, 10\,\%, -10\,\%$, and $-20\,\%$. The corridor, that the data set forms, is marked by a grey area. The general behaviour is preserved with all introduced deviations

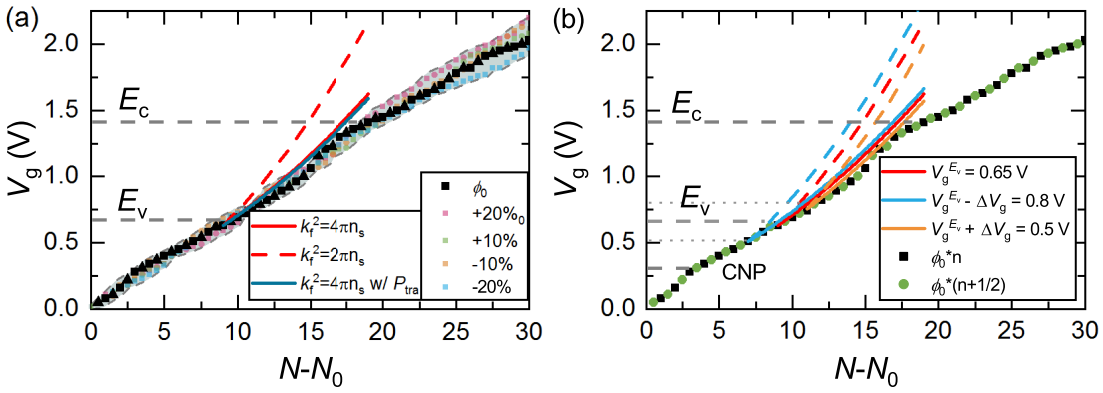

Figure 7.9: Discussion of possible errors in model curves. (a) Analysis in Fig. 7.5 was repeated with artificially introduced errors of up to $\pm 20\,\%$ in ϕ/ϕ_0 and plotted along with the initial data. The fit of the spin-resolved model is not affected. (b) The same subband analysis plotted with model curves beginning at different N_0 of ± 2 corresponding to a deviation of $\Delta V_g \approx 0.15\,\text{V}$ (marked by dotted lines) in the estimation of the VB edge. The curves for spin helical surface states remain the better fit.

and the model for spin-resolved surface states remains the more adequate. It should be noted that at fluxes of a few ϕ_0, a 20 %-deviation leads to data points, which originally entered into the averaged $\Delta G(V_\mathrm{g}, j\phi_0)$-trace, now being included in the half-integer $\Delta G(V_\mathrm{g}, (j+0.5)\phi_0)$-curve. This means that such assumptions are very strong, as entirely different parts of the $\Delta G(V_\mathrm{g}, \phi)$ colour plot can enter into analysis. A second point is, that Eq. 7.5 is only valid for an insulating bulk. Therefore the model can only be applied in the bulk band gap region of the band structure. Figure 7.9(b) shows that even an error of up to $\pm 0.15\,\mathrm{V}$ in $V_\mathrm{g}^{E_\mathrm{v}}$, which translates to a shift of ± 2 in N_0, has no effect on the conclusion. This shows that the method is robust against errors in the ϕ/ϕ_0-scale and $V_\mathrm{g}^{E_\mathrm{v}}$.

Another possible source of errors are the geometric simplifications to the nanowire cross section, discussed in Sec. 7.1. While this has no effect on the computed value of ϕ_0, as the rectangular area A is chosen such that $\phi_{0,\mathrm{tra}} = \phi_{0,\mathrm{round}}$, deviations in the circumference P and the effective capacitance C_eff are present. The influence of the simplified geometry on the model fits is visualized by the spin-resolved model curve (blue) in Fig. 7.9(a), calculated with the wire circumference of the trapezoidal cross section P_tra. The deviation is minimal and may be neglected.

Capacitance simulations are influenced by ignoring the rounded profile of the nanowire cross section, as well as edge effects from the finite nanowire length. The first case has been considered by additional electrostatic simulations, car-

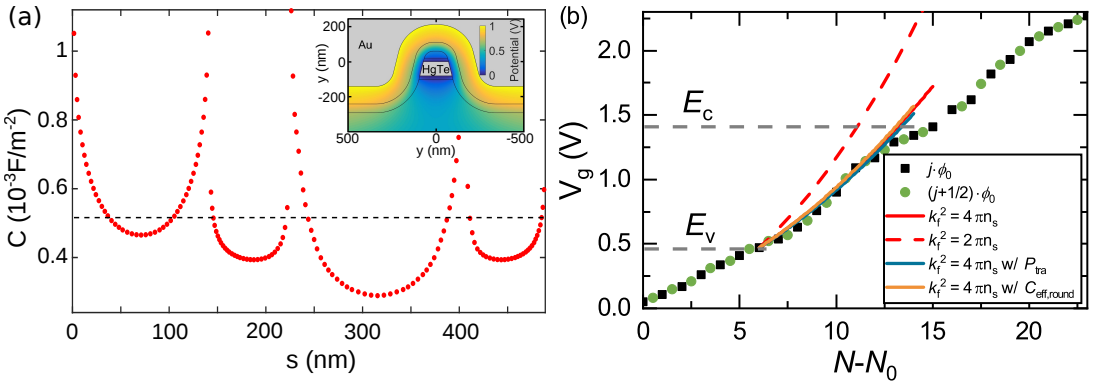

Figure 7.10: Influence of simplified geometry on analysis. (a) Simulation of nanowire s38w2's electrostatics using a model that accounts for the effects of wet-chemical etching, i.e. roundness and slanted sides. The effective capacitance C_eff changes to $5.035 \cdot 10^{-4}\,\mathrm{F/m^2}$ (from $5.208 \cdot 10^{-4}\,\mathrm{F/m^2}$ in the rectangular approximation; kindly provided by M.-H. Liu). (b) Analysis analogous to Fig. 7.5 was carried out for device s38w2. Model curves for the spin-degenerate (dashed, red) and the spin-resolved (red) model are plotted using the capacitance from the rectangular approximation. The deviation of the simplified geometry is visualized by plotting the effective capacitance from the rounded model $C_{\mathrm{eff,\ round}}$ (orange). The spin-resolved model calculated with the trapezoidal circumference P_tra (blue) is shown for comparison.

ried out by M.-H. Liu. Figure 7.10(a) shows $C(s)$ for nanowire s38w2 based on a profile that includes rounded edges from wet etching as well as the trapezoidal cross section. The profile is based on AFM profiles of real nanowires, as shown in Fig. 7.1(c). The general behaviour follows that of the simpler model in Fig. 7.7(a), with only a small correction of about 3 % to the extracted effective capacitance C_{eff}. The influence on model curves is shown in Fig. 7.10(b), where the same subband analysis as in Sec. 7.4 is presented for device s38w2. In addition to the models for spin-resolved (red) and spin-degenerate cases (dashed, red), curves that consider the trapezoidal geometry of the nanowires are plotted. Substituting $C_{\text{eff, round}}$ in the spin-resolved curve (orange) results in a small shift, while including the circumference of the trapezoidal geometry leads to another small shift in opposite direction.

Further errors are expected from simplifications in the electrostatic model, which considers a wire of infinite length. An estimation can be made by comparing the nanowire to calculations made for an analogous problem in Ref. [145]. In this work, fringe fields of two concentric metallic cylinders with length l, inner radius r_i, and outer radius r_a are calculated. Deviations from the infinite case are given as a function of $r_a - r_i$ and l. Modelling wire s38w1 as a cylindrical capacitor with $r_i = \overline{w}/2 = 155\,\text{nm}$ and $r_a = \overline{w}/2 + d_{oxide} = 325\,\text{nm}$, results in a ratio of $(r_a - r_i)/l = 0.13$ and allows a rough estimate of the error. For the parameters of nanowire s38w1, fringe fields are expected to increase the capacitance by roughly 10 % according to Ref. [145]. For longer wires this error is even smaller.

Further electrostatic simulations were made using *COMSOL* to confirm this estimate. The model takes into account both the rounded profile and the finite

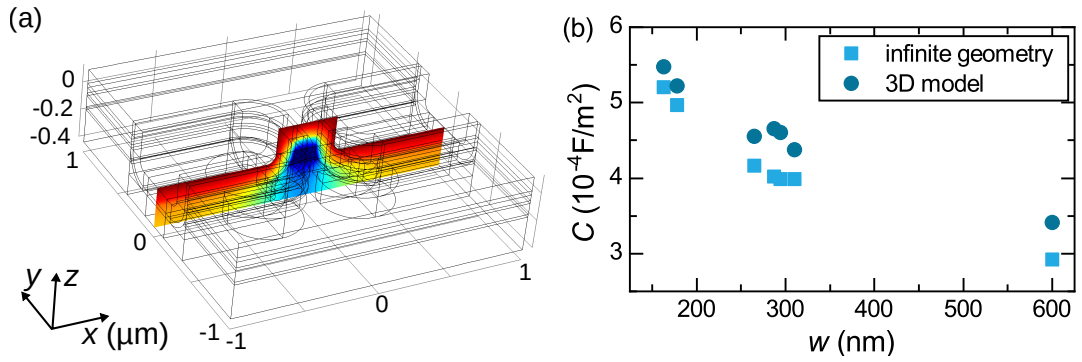

Figure 7.11: Electrostatic simulations of the full 3D geometry of strained HgTe nanowires. (a) The *COMSOL* model is shown for dimensions of device s58w1. The slice through the wire centre visualizes the potential drop from 1 V (red) to 0 V (blue) between topgate and TI surface as a colour gradient. (b) The capacitances C are plotted as function of wire width w for all devices that were built with the standard oxide stack of 30 nm SiO_2 and 100 nm Al_2O_3. Deviations remain below 10 %, with exact values depending on wire width w and length l.

length of the devices. A parametrized 3D model was created that includes all dielectric layers of the wafer and the subsequently deposited oxides. The model is shown in Fig. 7.11(a) with parameters of device s58w1. The procedure follows the overall approach of simulations for infinite length by M.-H. Liu [31] described in Sec. 7.4. A voltage of 1 V is applied at the topgate, while the surface of the TI nanowire acts as the ground potential. After calculation of the potential landscape, the surface electron density is extracted along the perimeter of wire's narrowest section and averaged. The systems capacitance C is calculated with the relation $C/e = \partial n_s/\partial V_\mathrm{g}$. In Fig. 7.11(b), the resulting capacitances are compared to results from previous simulations in the simplified geometry. They confirm above estimates that the infinite model underestimates capacitances by up to 10 %. The exact deviation depends on the length, etch depth and oxide thickness of the nanowire.

The simplified and 3D electrostatic models consider the topological surface states as metallic states and neglect contributions from the quantum capacitance of systems with a finite density of states [144]. This simplification of the model is nonetheless negligible, because the quantum capacitance C_Q contributes to the total capacitance C reciprocally, as given by

$$\frac{1}{C} = \frac{1}{C_1} + \frac{1}{C_2} + ... = \frac{1}{C_\mathrm{geo}} + \frac{1}{C_\mathrm{Q}} \,, \tag{7.6}$$

where C_geo is the geometrical capacitance. The geometrical capacitance will dominate the sum for $C_\mathrm{geo} \ll C_\mathrm{Q}$, which is often the case for large oxide thicknesses. The contribution of the quantum capacitance is only expected to become significant for an oxide thickness on the scale of a few nanometres. A rough estimate can be calculated from the density of states, given by $D = |E|/(2\pi\hbar^2 v_F^2)$. A typical value for v_F from literature is $0.43 \cdot 10^6$ m/s [54,146], so that $|E| = \hbar v_\mathrm{F} k_\mathrm{F} = 32$ meV at the VB edge. Here a charge carrier density, typical for E_F at the VB edge in macroscopic HgTe samples, of $n_s = 1 \cdot 10^{15}$ cm^{-2} is assumed. This results in a quantum capacitance of $e^2 D = 1.02 \cdot 10^2$ F/m^2, which is roughly by a factor 20 larger than the classical capacitance simulated for the investigated devices. The total capacitance in the case of device s38w2 is given by $C = (1/C + 1/e^2 D)^{-1} = 4.95 \cdot 10^{-4}$ F/m^2. Neglecting the quantum capacitance contribution therefore underestimates the total capacitance by $< 5\,\%$.

The analysis in the previous chapter is carried out with the assumption that the topological surface states are located roughly 5 nm within the HgTe bulk. This additional dielectric layer is neglected in the above models. A rough estimate can be obtained with a plate capacitor model that includes the additional dielectric. Calculations show that neglecting this deviation in our simple model leads to a capacitance $< 2\,\%$ larger.

In summary, the simplified electrostatic model includes errors by neglecting several aspects of the system. The largest error likely stems from neglecting fringe

fields due to the finite length of the nanowire and underestimates the capacitance by up to 10 %. All other simplifications of the infinite model, like neglecting the quantum capacitance, additional HgTe as a dielectric, and the rounded profile lead to overestimations of the capacitance by about 5 %, < 2 %, and 3 %, respectively. The overall deviation from modelled capacitance to an actual system is therefore rather small. In summary, the discussion of the models possible sources of error confirms the analysis of subband-induced oscillations with a capacitance from the simplified electrostatic model as a valid approach. Larger errors, that could make this model unsuitable, are expected for very thin oxide layers (quantum capacitance) and very short nanowires (fringe effects).

7.6 Simulations and theoretical considerations

The work on topological HgTe nanowires, presented in the previous chapters, was carried out in conjunction with theoretical investigations by R. Kozlovsky *et al.*, motivated by open questions that could not be resolved with experiments alone. Questions that arose are: Why are oscillation amplitudes smaller than e^2/h, even though a much cleaner signal could be expected for nanowires fabricated from high-mobility strained HgTe? How does gating the nanowires from the top only influence its properties? What are the implications in regards to the carrier density distribution for the topological surface states and their band structure? And, does the analysis of subband-induced oscillations in Sec. 7.4 remain valid with such deviations from the idealized theoretical model in Ref. [64] and Sec. 3.3.1? These questions were considered by R. Kozlovsky *et al.*, with results published in Ref. [31]. The main points, relevant for interpretation of experimental data, are summarized in this section. Parameters of device s38w2 were used as a basis for theoretical discussions. As previous sections focus on another device, the corresponding data set is included in App. A.3 for the sake of completeness.

For a more comprehensible discussion of inhomogeneous gating, a simplified model, which considers only top and bottom surfaces of the nanowire, is useful.

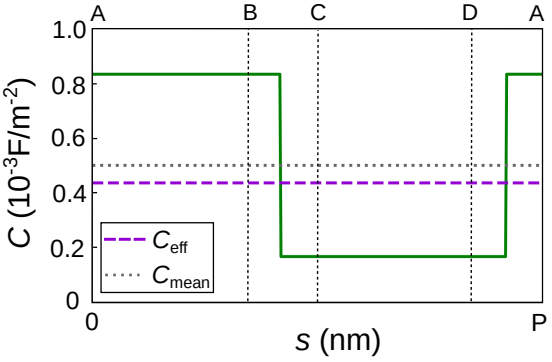

Figure 7.12: Step-like capacitance model for gate nanowires (adapted from [31]). The sides surfaces (segments BC and DA) are neglected and the capacitance profile $C(s)$ is given only by the values C_{top} and C_{bot}. The effective capacitance is given by $C_{\mathrm{eff}} = \langle\sqrt{C(s)}\rangle^2$, where $\langle ...\rangle$ is the mean along the circumference.

This translates to a step-shaped capacitance profile $C(s)$, pictured in Fig. 7.12, that is defined by the two values C_{top} and C_{bot}. The ratio of $C_{\mathrm{top}}/C_{\mathrm{bot}} = 5$ was chosen for didactic purposes. The band structure of a system is given by a Dirac cone that is split into subbands by the confinement to 1D. The enveloping Dirac cones for the two surfaces coincide for $V_{\mathrm{g}} = 0$. For $V_{\mathrm{g}} \neq 0$, the difference in capacitances leads to a relative shift between the bands on top and bottom surfaces. The shift of the two enveloping Dirac cones relative to each other is shown in Fig. 7.13(a). The distance of the two Dirac points are given by $E_{\mathrm{top}} = \hbar v_{\mathrm{F}} \sqrt{4\pi n_{\mathrm{top}}}$ and $E_{\mathrm{bot}} = \hbar v_{\mathrm{F}} \sqrt{4\pi n_{\mathrm{bot}}}$, while the Fermi energy is given by the average

$$E_{\mathrm{F}} = (E_{\mathrm{top}} + E_{\mathrm{bot}})/2 = \hbar v_{\mathrm{F}} \sqrt{\pi V_{\mathrm{g}}/e} \left(\sqrt{C_{\mathrm{top}}} + \sqrt{C_{\mathrm{bot}}} \right) \tag{7.7}$$

The numerical band structure calculations, using the Hamiltonian described in Sec. 3.3, are shown in Fig. 7.13(c) for fluxes of $\phi = 0$, $\phi_0/4$, and $\phi_0/2$. Just

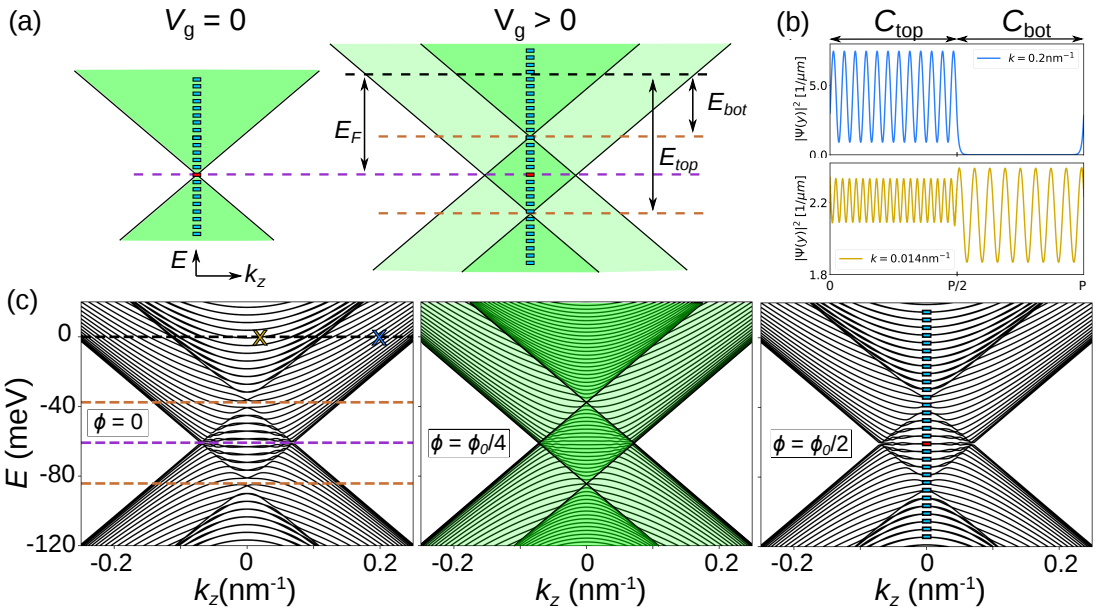

Figure 7.13: Gate-dependent band structure of a topological nanowire in the simplified model (adapted from [31]). (a) Schematic illustration of the band structure for zero (left) and finite (right) gate voltage V_{g}. In the latter case, bands are shifted relative to each other. Blue boxes mark equidistant subband minima. (b) Probability distributions of two representative states marked in (c, left panel) by crosses of respective colours. (c) Numerically calculated band structures for magnetic fluxes of $\phi = 0$, $\phi_0/4$ and $\phi_0/2$ at $V_{\mathrm{g}} = 1\,\mathrm{V}$. The positions of the shifted Dirac points (yellow) and the Fermi level (black) are marked by dashed lines in the left panel. In the middle panel areas corresponding to flux-sensitive states (i.e. that wrap around the wire) are marked dark green and flux-insensitive states in light green.

like in the theory for idealized nanowires, the band structure is flux dependent and ϕ_0-periodic. The angular momentum-degeneracy of the subbands and the linear modes at $\phi_0/2$ are preserved, although they are no longer linear over the full energy range. A closer look reveals that, even with shifted Dirac points, the subband spacing at $k_z = 0$, marked by blue boxes in the right panel, remains unaffected. The resulting band structure includes two different types of states. States marked in light green stem from a single Dirac cone and are, therefore, localized on a single surface. Consequently, they are flux-insensitive. States in the dark green regions stem from both Dirac cones. They extend around the entire wire perimeter, which makes them flux-sensitive. Examples of wave functions for both types of states are shown in Fig. 7.13(b). States that extend around the full wire perimeter (yellow) regardless of potential barriers from the capacitance profile are possible due to Klein tunnelling. For $k_z = 0$, they perpendicularly impact the potential barrier formed by the step-shaped capacitance. For states with a linear dispersion, this leads to perfect Klein tunnelling [147].

The same band structure calculations can be made for a realistic capacitance profile. Figure 7.14 shows results obtained for nanowire s38w2 with the capacitance profile $C(s)$ shown in Fig. 7.7(b) in Sec. 7.4. The picture has become more complicated since now all four surfaces are considered. However, all insights from the above discussion of the simplified model are still valid in the realistic model. Again, both the ϕ-dependence of the band structure with protected modes at $\phi_0/2$ and the equidistant subband spacing at $k_z = 0$ are preserved. The subband minima position remains at $k_z = 0$. The Fermi energy position is given by $E_\mathrm{F} = \hbar v_\mathrm{F}\sqrt{4\pi V_\mathrm{g} C_\mathrm{eff}/e}$, where $C_\mathrm{eff} \equiv \langle\sqrt{C(s)}\rangle^2$. It should be noted that C_eff is not the mean value. $C_\mathrm{mean} = \langle C(s)\rangle$ deviates from C_eff by the variance of $C(s)$, which is typically negligible in cases with realistic n_s-distributions ($C_\mathrm{eff}/C_\mathrm{mean} = 0.985$ for s38w2 [31]).

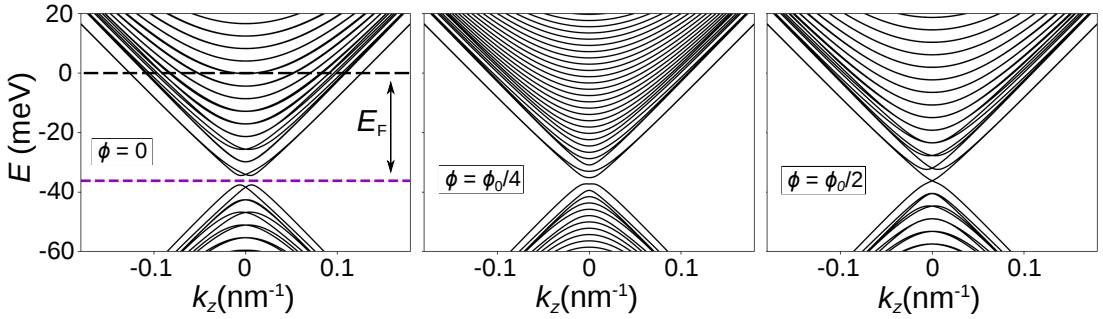

Figure 7.14: Band structure for a nanowire with dimensions of device s38w2 calculated for $V_\mathrm{g} = 0.3\,\mathrm{V}$ and a realistic capacitance profile $C(s)$ shown in Fig. 7.7(b). The band structure is shown for fluxes of $\phi = 0$, $\phi_0/4$, and $\phi_0/2$ from left to right (adapted from [31]). Properties such as flux-sensitivity and the protected modes remain present.

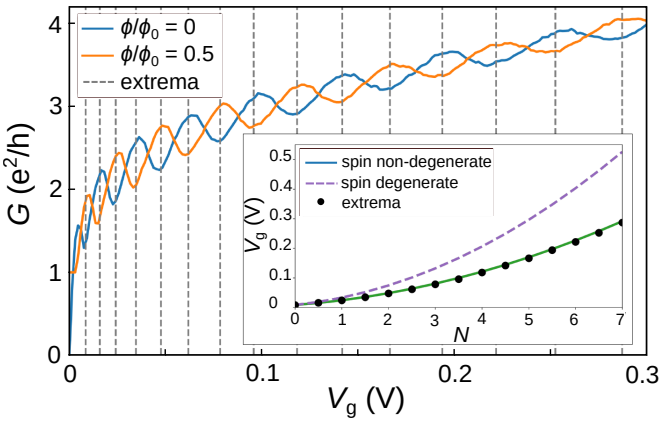

Figure 7.15: Simulated (disorder-averaged) conductance G as a function of V_g for the geometry and C_{eff} of device s38w2. The traces are shown for $\phi = 0$ (blue) and $\phi_0/2$ (orange). Corresponding minima/maxima pairs are indicated by vertical dashed lines. Their V_g-positions are plotted against an index N in analysis analogous to Sec. 7.4 in the inset, with model curves for spin-degenerate and non-degenerate cases.

The above band structure calculations show that the experimental signatures of topological nanowires and the core features of their band structures, discussed in Sec. 3.3, are robust against even major deviations in the device geometry. In a final step, the analysis of subband-induced oscillations in Sec. 7.4 is validated by a simulation of the conductance as a function of V_g. The calculation takes into account the residual disorder present in HgTe nanowires, but is done for a large number of disorder configurations resulting in the smooth curves in Fig. 7.15. The conductance G shows the same dependence on V_g as in the ideal theory in Sec. 3.3. When E_F is near a disorder-broadened band, the large density of states (van-Hove singularity) leads to enhanced backscattering. A decrease in conductance G is observed, before the mode fully opens and G increases again. In short, disorder leads to oscillations in $G(V_g)$ instead of step-like increases for every opened subband. The anti-correlated behaviour of the $\phi = 0$ and $\phi = \phi_0/2$-cases can be analysed just as the experimental data, because the equidistant subband spacing is preserved. The V_g-positions of corresponding minima/maxima pairs are plotted as a function of N in the inset of Fig. 7.15 along with model curves for spin-degenerate and spin-resolved cases. The curves are calculated from the same underlying Eq. 7.5 and effective capacitance C_{eff} as in analysis of the experimental data. Not surprisingly, the data points follow the model for spin-resolved states. Nonetheless, the use of an effective capacitance C_{eff} is justified in retrospect for use in analysis of the experiments despite the complicated capacitance profile $C(s)$ of investigated HgTe nanowires.

The case of trivial surface states with a quadratic dispersion was also considered. Even though Klein tunnelling should be absent, the consequences for the experimental regime accessible in HgTe nanowires, i.e. E_F far away from the Dirac point, are too small to influence the general behaviour in $\Delta G(V_g)$ other than the spin-degeneracy factor. Trivial states are expected to show the same parabolic

behaviour in analysis, but follow the spin-degenerate model equation.

Apart from confirming the presence of key band structure features in the investigated HgTe nanowires and justifying the analysis of the experimental data, the theoretical study gave further insights. Experiments with backgated nanowires, for instance, where initially considered so that the inhomogeneous carrier density distribution could be modified. The fabrication of backgated devices comes with a lot of experimental problems, regardless of if one chooses substrate thinning or doped substrates as an approach. Details are discussed in Ref. [104]. In any case, the theoretical investigations by Kozlovsky *et al.* have made such experiments obsolete, due to the finding that Klein tunneling allows extended states despite a inhomogeneous carrier density distribution. Introducing a backgate to tune the inhomogeneity should therefore have no significant influence.

7.7 Ensemble averaging

In the classical case of AB rings in 2DESs, averaging over several disordered interferometers, called ensemble averaging, can be used to average out mesoscopic noise in diffusive or quasi-ballistic devices [79]. However, ensemble averaging also leads to a suppression of h/e-periodic oscillations. This results from different regions of the ensemble array no longer being correlated when the array becomes larger than the inherent phase coherence length. The random phase distribution of AB oscillations causes their contributions to average out over the full array. This is not the case for AAS oscillations so that the amplitude of $h/2e$-periodic

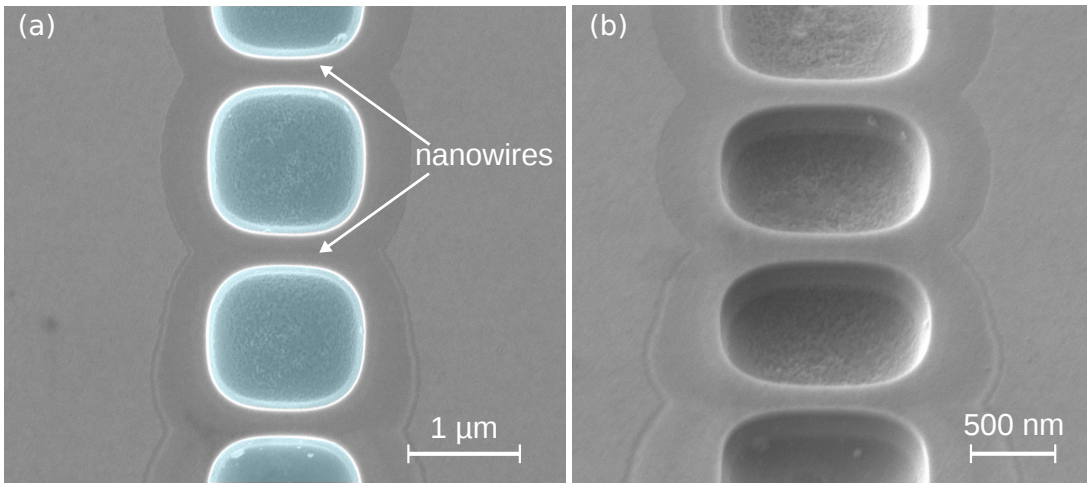

Figure 7.16: SEM-micrographs of an array of three parallel nanowires with average widths of 316, 322, and 310 nm (from top to bottom) viewed from (a) above and (b) at an angle of 50 °. The images were taken before deposition of the topgate stack.

conductance corrections remains unaffected [85]. The origin of h/e-periodic magnetoconductance oscillations in TI nanowires is rooted in the variation of the band structure by a magnetic flux. In previous chapters, it was shown that transport is ballistic on the order of the wire circumference P and at least quasi-ballistic on the scale of the wire length. Here, the influence of ensemble averaging on these devices is investigated.

Two devices with three (s47w1) and seven (s47w2) parallel nanowires were fabricated to test this hypothesis. The $n = 3$ ensemble is shown in SEM-micrographs in Fig. 7.16 and will be discussed in the following. The three nanowires have average widths between $\bar{w} = 310$ and 322 nm. Flux and gate voltage dependent conductance corrections $\Delta G(\phi_0; V_\mathrm{g})$, as shown in Fig. 7.17(a), were analysed analogously to Sec. 7.3 and 7.4. The data set was treated with the same methods as above, including removal of the magnet hysteresis, subtraction of a smoothly varying background $G_\mathrm{sm}(B)$ and calculation of ϕ in units of ϕ_0. For the latter, the average of all three wire widths $\bar{w}_\mathrm{avg} = 307$ nm was used. Additionally, the conductance was normalized to the number of nanowires n in the sample, denoted as G_n. The topological surface states were presumed to reside 5 nm within the HgTe cross section as before. The data set exhibits characteristic h/e-periodic

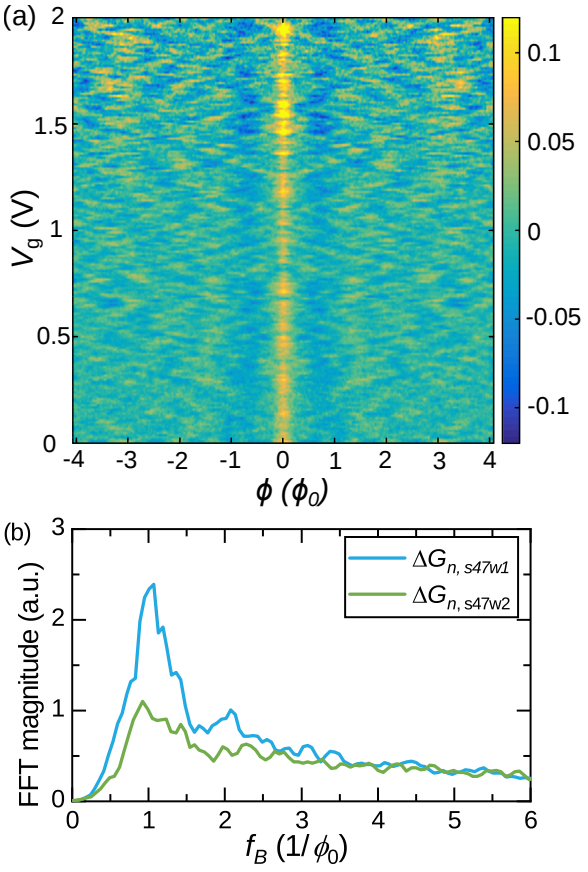

Figure 7.17: Quantum conductance corrections of a nanowire ensemble. (a) The normalized conductance correction ΔG_n from device s47w1 shown in a colour plot as a function of magnetic flux ϕ and gate voltage V_g. (b) V_g-averaged FFT spectra of magnetoconductance traces up to 12 ϕ_0 in the same gate voltage range as (a) for both investigated multi-wire devices.

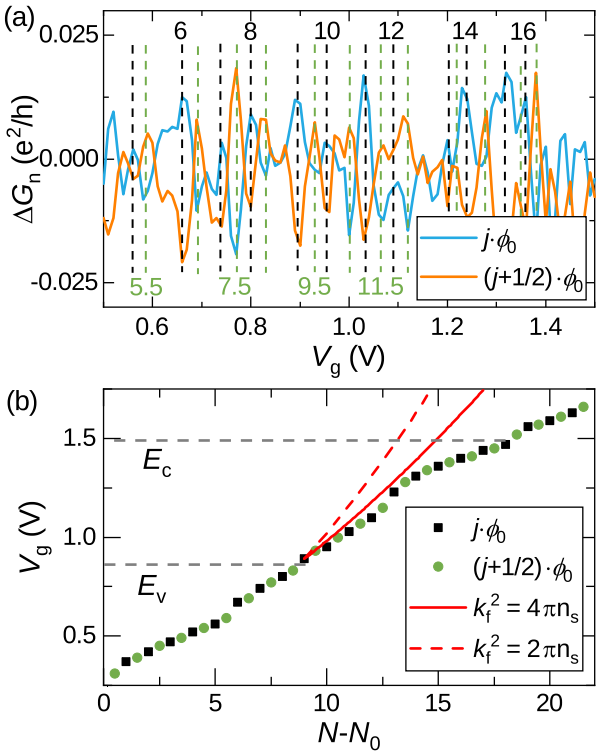

Figure 7.18: Subband analysis of an ensemble of three parallel nanowires. (a) The normalized conductance correction ΔG_n is shown as a function of V_g for integer and half-integer flux. Corresponding minima/maxima pairs are marked by dashed lines and assigned subband indices $N - N_0$. (b) $V_g(N - N_0)$ is plotted with black, dashed lines denoting the valence and conduction band edges. Model curves, valid only in the bulk gap, calculated for the spin-resolved (red) and spin-degenerate (dashed, red) cases are plotted alongside. The band edge positions E_c and E_v were extracted from measurements of a Hall bar located on the same sample.

oscillations and a switching of the phase with gate voltage V_g as in single nanowire devices. Additional measurements up to $\phi = 12\,\phi_0$ were carried out to improve accuracy of the Fourier spectra, which confirm the predominantly h/e-periodic magnetoconductance oscillations in both devices. The V_g-averaged spectrum, shown in Fig. 7.17(b), shows a large peak at a period of ϕ_0 with a smaller feature at $\phi_0/2$. The AB-type oscillations are, however, not suppressed in comparison to higher order oscillations, such as $\phi_0/2$. Instead, amplitudes from all frequencies are suppressed in the normalized signal. Analysis of the subband-induced conductance oscillations, as in Sec. 7.4, was also carried out. Here, the measured conductance is normalized to the number of nanowires in the ensemble. As before, $\Delta G_n(V_g)$ is plotted for integer and half-integer fluxes and examined for pairs of matching minima and maxima [see Fig. 7.18(a)]. Each pair is assigned a subband index $N - N_0$, and its V_g-position is plotted in Fig. 7.18(b). Model calculations for spin-resolved (red) and spin-degenerate (red, dashed) cases are shown, with a reasonable fit between the spin-resolved case and the data. The model for spin-degenerate surface states strongly deviates from the observed subband progression, as expected from previous experiments in single nanowires. Measurements on the $n = 7$ device showed an even stronger suppression of the quantum conductance corrections as can be seen from the reduced FFT magnitudes for $\Delta G_{n,\mathrm{s47w2}}$ in Fig. 7.17(b). In addition to a suppressed peak at $f_B = 1/\phi_0$, all indications of signals for higher order oscillations ($2/\phi_0, 3/\phi_0$, etc.) are nearly

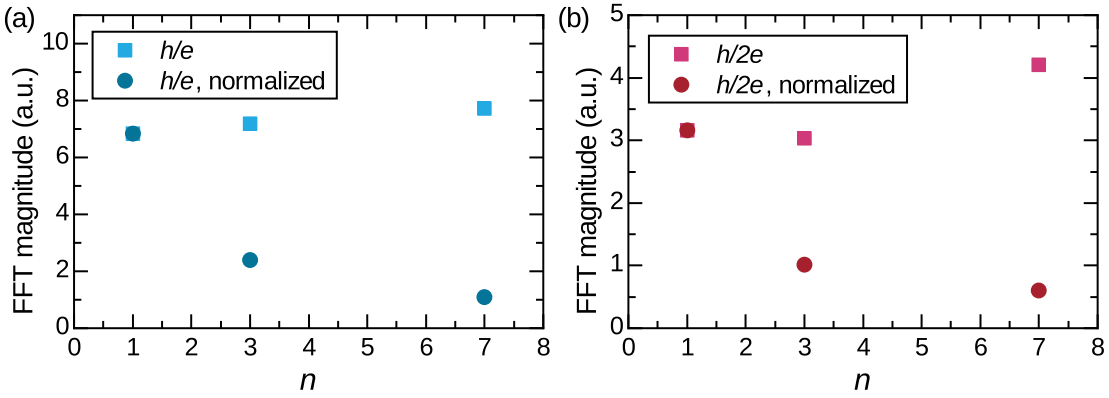

Figure 7.19: Maximum FFT peak values for the investigated arrays with $n = 1,\ 3$, and 7 parallel wires are shown for (a) h/e- and (b) $h/2e$-periodic signals. Values derived from the absolute conductance ΔG (square) as well as the normalized conductance ΔG_{n} (round) are shown.

indistinguishable from the FFT background.

Figure 7.19 compares FFT peak amplitudes for devices with 1, 3, and 7 parallel nanowire constrictions. For the single nanowire, data from device s38w1 was used due to the nearly identical dimensions. When deriving the amplitudes of higher order $h/2e$-oscillations from the conductance correction of the array ΔG, they remain roughly constant with increasing number of wires n. Amplitudes in the normalized signal ΔG_n decrease accordingly. This behaviour is not unusual, as the signal amplitude remains unaffected by an increase of n even in the case of AAS-oscillations [85, 148]. For h/e-periodic signals, the behaviour is similar. Again, the h/e-signal decreases in the normalized case. And amplitudes in the signal of the full array ΔG are nearly constant with varying n, with a slight tendency towards an increase with higher n. Theory, however, predicts a decrease of the oscillation amplitude of an array proportional to $n^{-1/2}$ for AB oscillations in diffusive or quasi-ballistic arrays, where the array is larger than l_ϕ [79, 85, 86]. In the HgTe nanowires, the phase coherence l_ϕ reaches peak values of over 5 µm as determined in Sec. 7.2. The investigated nanowire ensembles have widths of $w_{\mathrm{array}} = 3.5\,\mu\mathrm{m}$ and 10 µm for the cases of $n = 3$ and $n = 7$, respectively. While the dimensions of the three-wire-array are on the order of l_ϕ, a coherent state across all three wires is highly unlikely. It would require a coherent path across both top and bottom surfaces of the 3DTI, i.e. $l_\phi > 2w_{\mathrm{array}}$. For the $n = 7$ device, coherent behaviour is ruled out entirely.

The roughly constant amplitudes of h/e-oscillations in the arrays, relative to $h/2e$, suggests that the TI nanowires are nearly ballistic (on the scale of the wire circumference P). The $h/2e$-periodic signals are not a consequence of disorder-induced AAS-type time-reversed paths. Instead, they can be attributed to higher

order AB oscillations, due to the large phase coherence length on the order of the circumference P. The lack of a cleaner oscillatory signal in the arrays can be explained by small differences in the nanowire dimensions, wafer and electrostatic inhomogeneities[3]. These would entail deviations of n_s, and thereby of the E_F-position, which lead to phase shifts in the oscillatory contributions from each wire in the ensemble. A variation of nanowire widths, present in both investigated devices, leads to multiple frequencies overlapping. Furthermore, the subband spacing Δk_l depends on the circumference P and therefore varies slightly for each nanowire. The Fermi energy E_F can then be positioned differently in neighbouring nanowires, e.g. in between subbands (at $k_z = 0$) for one and in a subband for another nanowire. AB oscillations from differently sized nanowires in an array would therefore produce oscillations with different frequencies but also varying phases at $\phi = 0$. The intended enhancement of conductance corrections, only possible for perfectly matching nanowire geometries, becomes difficult to realize experimentally. It can be concluded that the accuracy in the investigated ensembles was not sufficient.

7.8 Shubnikov-de Haas, Hall and quantum Hall effect

Topological nanowires represent an interesting case in that they are 3D objects with 2D surface states that feature a 1D band structure. This brings forth a number of effects usually not observed within the same system. Previous chapters discuss effects in parallel magnetic field configurations. Here, the magnetic field is applied perpendicular to the nanowire and the sample plane. For the analysis in previous chapters, access to the capacitance C of the system was required. Usually, it can be obtained experimentally by measuring the charge carrier density n_s as a function of gate voltage V_g and extracting it via the relation $\partial n_s/\partial V_\mathrm{g} = C/e$. The initial motivation for out-of-plane field configurations was therefore to

[3]Opposed to ensemble averaging effects in disordered semiconductor loop arrays.

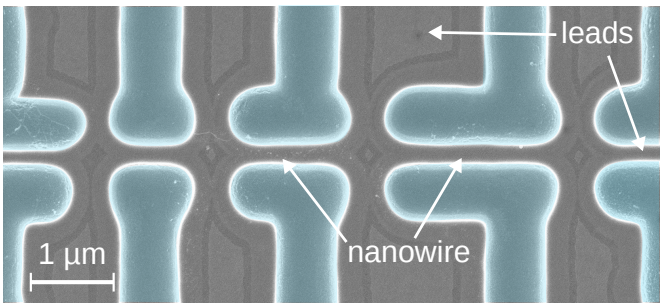

Figure 7.20: SEM-micrograph of a representative nanowire Hall bar. The depicted device (s53) consists of wires with lengths of 1 (s53w1), 1.5 (s53w2), and 2 µm (s53w3) and widths of around 280 nm. The potential probes are between 420 and 440 nm wide.

investigate SdH oscillations, the Hall effect, and QHE in nanowires. The latter two require nanowires with different a design, i.e. one that includes voltage probes. Such a nanowire Hall bar is shown in Fig. 7.20. Measurements were carried out with both types of nanowires.

Indeed, oscillations are visible in the longitudinal signal of the HgTe nanowires for both n- and p-type conduction. Figure 7.21 shows Landau level fan charts from four nanowire constrictions with lengths of 1.3 µm and widths $\bar{w}$ varying between 163 and 990 nm. The second derivative of magnetoconductance traces for fixed V_g are shown in the form of colour maps. Yellow depicts a positive and

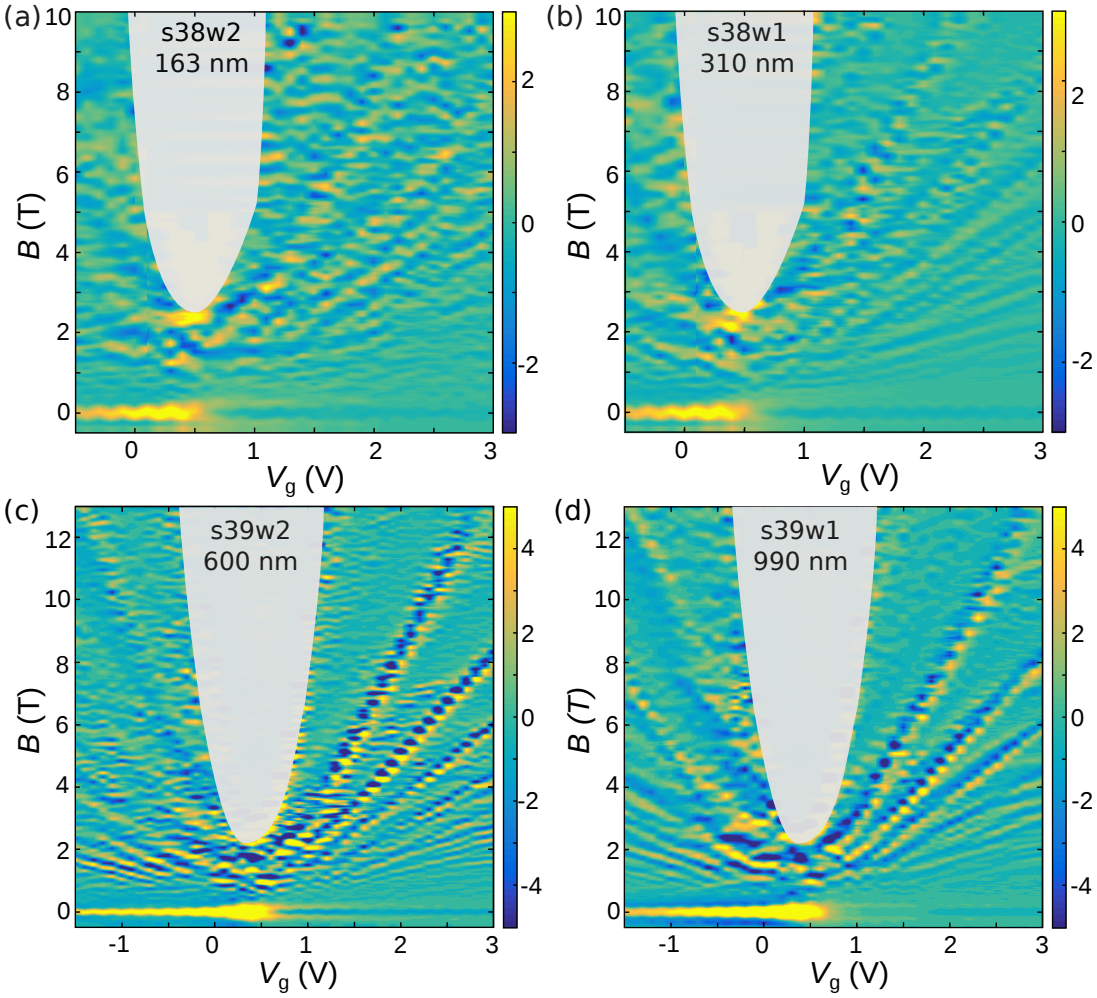

Figure 7.21: Landau level fan from topological nanowires. The colour maps show the smoothed second derivative of the longitudinal resistance $\partial^2 R_{xx}/\partial B^2$ as a function of B and V_g for wires with widths of (a) 163, (b) 310, (c) 600, and (d) 990 nm. All devices are 1.3 µm long. The grey areas mark unusable data, where the resistance of the samples diverges and current collapses.

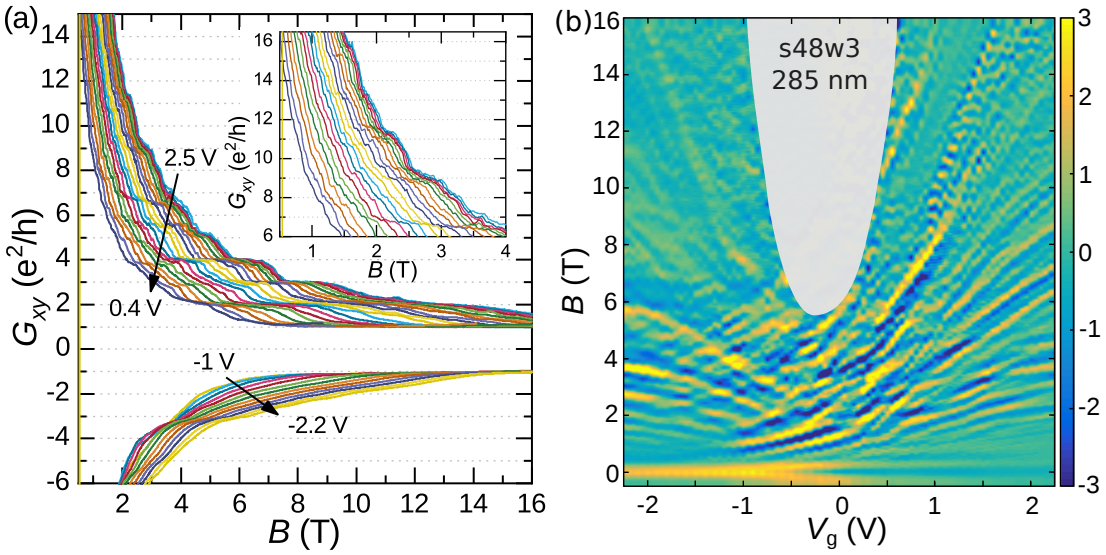

Figure 7.22: Quantum Hall effect in nanowire Hall bars. (a) $G_{xy}(B)$ from device s48w3 is plotted for a range of gate voltages ($V_g = 2.5...0\,V$). (b) Landau level fan chart from device s48w3 shown as the second derivative $\partial^2 R/\partial B^2$ for increased visibility of features throughout the parameter range. The region where the sample resistance diverges due to a combination of small n_s and large B is greyed out.

blue a negative curvature in the signal, with green representing no curvature. The diagonal lines of blue and yellow therefore correspond to resistance maxima, i.e. Landau levels. The green areas in between correspond to Landau gaps. This is best visible in the data set from the widest investigated nanowire in Fig. 7.21(d). In thinner nanowires [Fig. 7.21(a) through (c)], the features become less and less pronounced and Landau fans become non-linear. Consequently, analysis of single magnetoconductance traces does not yield the typical $1/B$-periodicity expected from SdH oscillations. Therefore, the charge carrier density can not be extracted using known relations. The origin of the oscillations in the constrictions, as opposed to the leads before and after, was confirmed by measurements on devices with a nanowire Hall bar design [see Fig. 7.20]. In such samples, pronounced QH plateaus are present in the Hall conductance, which feature the same sequences, including the deviations from a $1/B$-periodicity. Representative data from a nanowire Hall bar is shown in Fig. 7.22, where the Hall conductance is plotted in (a) and a corresponding colour plot of quantum oscillations in the longitudinal signal in (b). The Hall conductance G_{xy} features pronounced plateaus at quantized integer values of e^2/h. For negative V_g between -1.0 and $-2.2\,V$, a filling factor sequence of $\nu = -1, -3, -5$ is visible from plateaus at corresponding conductance values. For positive gate voltages $V_g > 0.4\,V$ the behaviour is not as straightforward. At high fields, conductance plateaus are found for filling factors $\nu = 1...4$, whereas the sequence continues with odd integers only, i.e. $\nu = 5, 7, 9, 11$, for $B < 5\,T$. Further plateaus at $\nu = 13$ and 15 are hinted at

in the data. These sequences stem from the presence of two topological surfaces, as described in Sec. 3.1.4 for the macroscopic case.

The deviation from the $1/B$-periodicity of SdH oscillations can be explained by considering the effect of the small sample width and the quantizing magnetic field on the band structure. Calculations that consider the formation of Landau levels in a 1D band structure are found in literature for carbon nanotubes [89], constrictions in classical 2DESs [149] and generic topological nanowires [139]. The general behaviour is that with increasing magnetic field, the subbands will form flat Landau levels with an rising subband spacing. This is refered to as magnetic depopulation of subbands [149, 150]. The quantization is however not fully developed due to the lateral constriction. This means the deviation will increase for decreasing sample widths. Additionally, the formation of Landau levels also becomes weaker at higher energies, i.e. subbands with higher angular momentum quantum number l. Figure 7.23 shows band structure calculations for a gated HgTe nanowire in a quantizing magnetic field, where the full electrostatic model is included. The dashed lines mark analytical positions of Landau levels originating from top (blue) and bottom (green) surface. A pronounced energy shift between Landau levels from the top and bottom surfaces is seen in the simulation. The energy position of the levels do match expected analytical values, however. As described, the width of the flat bands decreases with increasing angular momentum quantum number l. This effect becomes stronger for decreasing nanowire width w. The vertical red lines mark the $\boldsymbol{k}$-space width of a corresponding Landau level in a classical 2DES, which depends on the sample width w. Towards higher energies E, a mismatch between the analytical case for 2DESs and the width of the Landau levels in 3DTI nanowires is observed. This means that the analytical formula for the carrier density per LL n_{LL} will no longer be accurate. Another consequence of inhomogeneous carrier density distribution is a bending of the Landau levels. The pronounced dips in the bands are a general feature of 3DTI systems [71, 139]. In conclusion, the picture of well defined δ-peaks for LLs

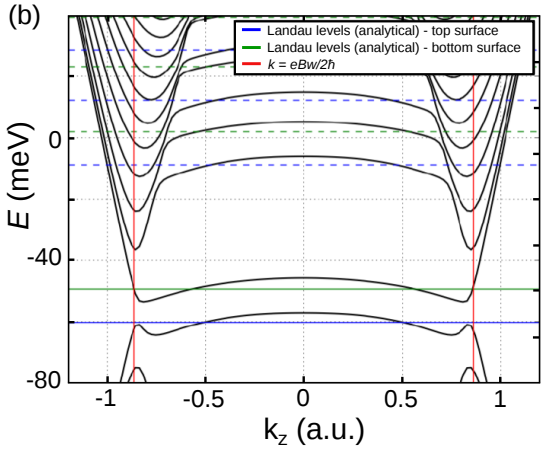

Figure 7.23: Band structure simulations for a 142 nm wide HgTe nanowire in an out-of-plane magnetic field (kindly provided by R. Kozlovsky [132]). The calculation for a field of $B = 8\,\mathrm{T}$ and $V_\mathrm{g} = 1.5\,\mathrm{V}$ takes into account the full capacitance profile of the electrostatic model from Sec. 7.4. Landau level positions are shown in dashed blue (green) for the top (bottom) surface, with the full lines marking the $\nu = 0$ Landau level.

in the DOS $D(E)$ is no longer valid. Bands are broadened over a sizeable energy range, so that protected edge channels are difficult to find. Conductance minima are consequently also expected to be less well defined.

Another common method to determine n_s is the classical Hall effect, as measured in nanowire Hall bars. However, the spatial positioning of the topological surface states again prevents access to the total charge carrier density n_s. In the simple picture, top and bottom surfaces of the nanowire are pierced by a perpendicular magnetic field and contribute to a Hall signal. The side surfaces are exposed to an in-plane field only and do not produce a Hall voltage. Even magnetic fields applied along both perpendicular axis to the wire, either by tilting the sample 45° or via a vector magnet, would not immediately resolve the dilemma. In such a setup, all interfaces would be exposed to perpendicular field components, but would require additional contact pairs to probe the Hall voltage from the side surfaces. It should be noted that measurements of the classical Hall conductance in nanowires can be found in literature [151–154]. All these reports are from experiments on topologically trivial systems, where carriers are distributed throughout a conducting bulk. The most appropriate comparison to HgTe nanowires can be made to the experiment in hexagonal InAs nanowires with metallic side contacts [151]. Apart from a conducting bulk, InAs nanowires feature trivial surface states, which are presumed to not contribute to transport. The hexagonal cross section allows for perpendicular field components in all facets and an extraction of the Hall voltage through careful consideration of the geometry. However, none of the cited works investigate conducting states confined to a nanowire surface, especially with surfaces perpendicular to the external field and Hall probes, as in the present case. An example for a system with conducting surfaces are carbon nanotubes, but no reports of Hall voltage measurements have been found.

7.9 Towards quantum point contacts

Quantum point contacts are predicted to be an important building block for more sophisticated devices, that enable the spectroscopy of Majorana fermions and topological superconductivity [155, 156]. The design of topological nanowire constrictions, investigated in the previous chapters, already closely resembles point contacts. Transitioning to point contact constrictions is therefore only a matter of scaling down the device size, with the goal of reaching a transmission of a few modes.

In order to observe a quantized conductance, one needs to reach the experimental regime, where only a few subbands are occupied in the energy gap. To this end, an estimated cross section on the order of $50 \times 50\,\mathrm{nm}$ is required, which can be deduced from the energy distance of the Dirac point to the VB edge

Table 7.2: Essential geometrical parameters of the fabricated point contact constrictions. The height of all wires is given by the 50 nm thick HgTe layer. The median width and length of the wires are denoted by $\overline{w}$ and l. The wire circumference P and the expected period for ϕ_0 periodic oscillations $\Delta B_{h/e}$ were computed from the device dimensions as extracted from SEM-micrographs.

device	$\overline{w}$ (nm)	l (µm)	P (nm)
s61w2	24	0.4	148
s61w1	37	0.4	174
s63w1	56	0.4	212
s63w2	68	0.4	238

(32 meV; see Sec. 7.5), the bulk energy gap (15 to 20 meV; Ref. [54, 146]), and the subband spacing ($E = \hbar v_\mathrm{F} \Delta k_l = 8.9$ meV for $P = 200$ nm). In this example, an estimated three (five) occupied subbands would be expected at the lower (upper) end of the bulk energy gap. Also, a constriction length of < 300 nm, as in initial QPC experiments in GaAs [93, 95, 129], is preferable to ensure fully ballistic transport. With the previously used 80 nm wafers, the device height is limited by the dimensions of the HgTe layer and device lengths have a lower limit from under-etching. The targeted device dimensions are not attainable with this wafer, so that a new wafer with a thinner 50 nm HgTe layer was grown at the A.V. Rzhanov Institute for Semiconductor Physics, Novosibirsk to overcome these limitations. A first generation of point contacts, with a length of 400 nm and median widths of $\bar{w} = 24...68$ nm, was fabricated. A representative device is shown in Fig. 7.24 and parameters of discussed samples are listed in Table 7.2.

There are currently no known measurements of 50 nm strained HgTe wafers on

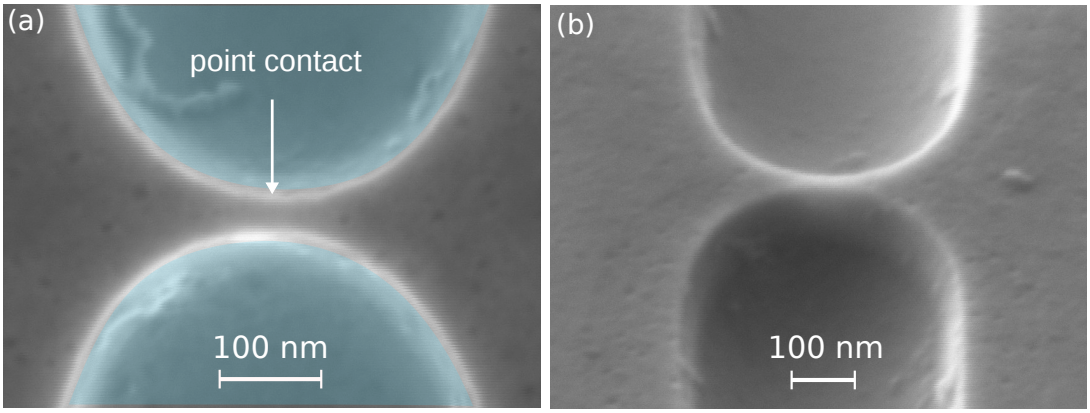

Figure 7.24: SEM-micrographs of the representative point contact device s63w1 in (a) top-view and (b) tilted view at 50 °. The constriction has a length of $l = 400$ nm and a median width of $\bar{w} = 56$ nm at the HgTe layer.

(013)-substrates, so that a full transport characterization was carried out. The overall quality of the material is comparable to its 80 nm counterpart. In the 50 nm wafer, electron mobilities reach up to $\mu = 580 \cdot 10^3 \mathrm{cm}^2/\mathrm{Vs}$. In the bulk gap, mean free path lengths l_e of 2 to 5 µm and Fermi wavelengths in the range of $\lambda_\mathrm{F} \approx 50\,\mathrm{nm}$ are found. The gap is located roughly between $V_\mathrm{g} = 0.90\,\mathrm{V}$ and 1.95 V. Detailed results are discussed in App. A.1.

In the following, data from device s63w1 will be discussed representatively. The presence of 1D subbands with a coherent state around the perimeter of the constriction was confirmed by the analysis of subband-induced oscillations, described in Sec. 7.4. The corresponding data analysis is shown in App. A.5. The point contact constriction has an average width of $\bar{w} = 56\,\mathrm{nm}$. A larger device with a width of 68 nm (s63w2) showed qualitatively similar behaviour. Smaller constrictions with widths $< 37\,\mathrm{nm}$ had conductances far below e^2/h and were, therefore, not investigated in more detail. Figure 7.25 shows temperature dependent gate traces $G(V_\mathrm{g})$ of point contact s63w1, recorded at a bias current of 2 nA. A conductance ranging from $G = 3$ to $4.5\,e^2/h$ is found in the gap between $V_\mathrm{g} = 0.9$ and 1.95 V. This agrees well with the estimated number of modes for a device of the present size. Large conductance fluctuations, likely from mesoscopic noise, are superimposed on the signal for $T = 50\,\mathrm{mK}$. Measurements were carried out at up to $T = 800\,\mathrm{mK}$ to suppress them. The blue trace is the average over traces at all measured temperatures, and was calculated to remove noise. At temperatures of 400 mK and higher, single curves no longer significantly deviate from the averaged curve. Although the visible oscillatory pattern is reproducible, the signal lacks pronounced quantized conductance steps. The measurements were repeated for lower bias currents to exclude any influence of heating effects. Bias currents as low as 100 pA were applied to fulfil the condition $U_\mathrm{4pt} < k_\mathrm{B}T/e$ for the four-point voltage. However, no noteworthy improvements were observed at $B = 0$.

A typical effect in quantum point contacts is that a small magnetic field perpendicular to the sample plane will stabilize conductance plateaus in the longitudinal

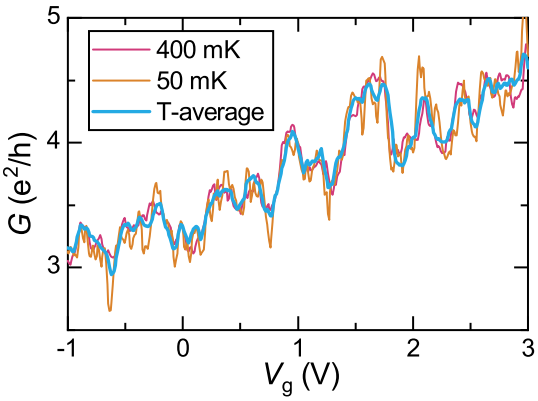

Figure 7.25: Conductance traces of device s63w1 at $B = 0$. A temperature-averaged (50 mK to 800 mK) trace is shown (blue) along with curves for 50 and 400 mK. The data was recorded at $B = 0$ and with a bias current of 2 nA.

signal by suppressing backscattering in or near the point contact [95]. To this end, measurements in perpendicular magnetic fields were carried out. The traces, taken at fields up to $B = 2.2\,\mathrm{T}$, are plotted in Fig. 7.26(a) for a bias current of $I = 100\,\mathrm{pA}$. The conductance G decreases with increasing B. The effect is strongest for $V_\mathrm{g} < V_\mathrm{g}^{E_\mathrm{v}}$, but is present in the entire plotted V_g-range. At small magnetic fields of 0.6 and 0.8 T (green curves) resemblances of a plateau near $2.5\,e^2/h$ appear. A clear sequence of quantized conductance steps is still absent. In large fields, this changes. For $B > 1.6\,\mathrm{T}$, a plateau appears between $V_\mathrm{g} = 0.9$ and 1.5 V near $1.7\,e^2/h$. And at $B = 2\,\mathrm{T}$ and larger, a pronounced plateau is observed at e^2/h. In a semi-classical picture, the transition can be attributed to the diameter of cyclotron orbits becoming smaller than the constriction width, i.e. $2r_c < w$ [129].

There are however many possible reasons as to why no zero-field quantized conductance is observed. Among them are overall quality of the material, the rounded geometry of the constrictions, and distribution in 3D of the charge carriers. First experiments on QPCs by van Wees *et al.* [93] used GaAs/AlGaAs 2DESs with an electron mobility μ_e of $850 \cdot 10^3\,\mathrm{cm}^2/\mathrm{Vs}$, a mean free path length of $l_e = 9\,\mu\mathrm{m}$ and a Fermi wavelength on the order of $\lambda_\mathrm{F} \approx 40\,\mathrm{nm}$. These parameters are all comparable to the 50 nm strained HgTe wafer, assuming the current fabrication processes do not significantly worsen transport properties in nanostructures. Another possibility may be due to the confinement potential. Classical GaAs QPCs devices are created using split-gates that deplete the 2DES underneath them, which leads to a smooth potential transition [92, 93]. Such constrictions are called adiabatic [96], in that their potential is smooth on the order of the Fermi wavelength λ_F. It has been reported that the smooth con-

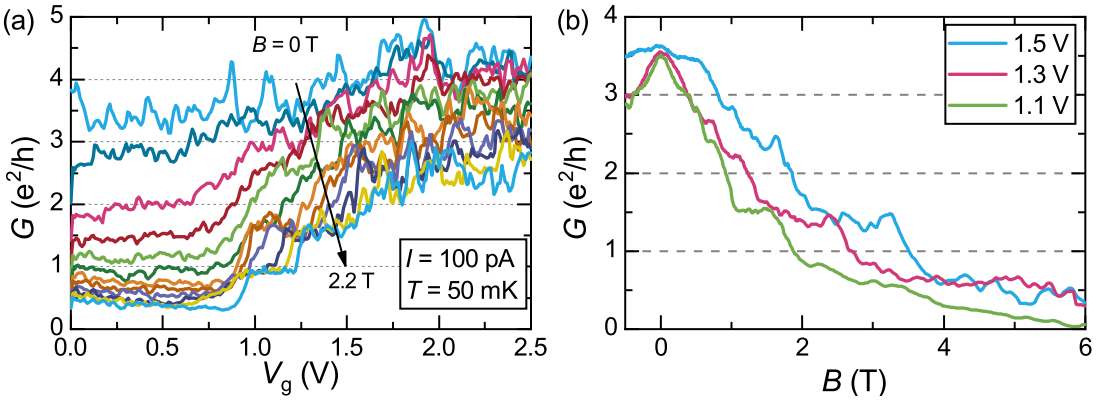

Figure 7.26: Magnetic depopulation in point contact device s63w1. (a) $G(V_\mathrm{g})$ for magnetic fields from $B = 0$ to 2.2 T in steps of 0.2 T and a bias current of 100 pA. Quantized plateaus at $B > 2\,\mathrm{T}$ are a sign of Landau level formation in the constriction. (b) Conductance traces $G(B)$ for three gate voltages (1.1, 1.3, and 1.5 V) in the bulk gap. 1D subbands are depopulated as the magnetic field B increases.

finement potential benefits the quantization of conductance [129]. In present devices, the electron gas is constricted by etching the material, which leads to a round, smooth constriction profile. But it also creates a hard-wall potential for the surface states. This limitation cannot be circumvented due to the nature of the surface states. Additionally, the inhomogeneous charge carrier density distribution along the perimeter of the cross section, discussed in Sec. 7.4 and 7.6, may hinder formation of quantized modes.

Despite the lack of a quantized conductance, signs of a depopulation of the 1D subbands in magnetic fields are present. This can be seen on the one hand by the decrease of G and ultimately the appearance of plateaus with increasing magnetic field B in Fig. 7.26(a). The second indication are visible plateaus in the magnetoconductance traces plotted in Fig. 7.26(b). The curves were recorded at gate voltages of $V_\mathrm{g} = 1.1$, 1.3, and 1.5 V, which are attributed to the bulk gap. The steps are not at expected integer multiples of e^2/h, but instead at disorder-induced non-integer values of 1.5 and $2.3\,e^2/h$. These can be attributed to the formation of Landau levels in the subband structure. Similar behaviour was first described in GaAs 2DES constrictions, c.f. Refs. [149, 150]. In the 2D case, a rising perpendicular magnetic field B causes the quadratic 1D subbands to flatten and have an increased subband spacing. Here, the mechanism is the same as illustrated with Fig. 7.23 in Sec. 7.8. In large perpendicular fields, the 1D band structure transitions to flat Landau bands and the formation of backscattering-protected states similar to QH edge channels. The subband spacing increases with B, so that the number of occupied bands at E_F and thereby the conductance G decreases. The increasing subband spacing also improves transmission of the occupied bands at E_F and thereby permits a quantized conductance contribution per subband.

8

Summary

In summary, the wet-chemical etching approach to sample fabrication enabled a thorough study of topological boundary states in HgTe-based 2D and 3D topological insulators. In this thesis, distinct Landau levels from bulk hole, TSS, and bulk electron states were studied in macroscopic devices. In addition to previous studies of the QHE in strained HgTe (c.f. Refs. [51,52,54] and [25]), coexisting n- and p-type Landau levels were observed at millikelvin-temperatures due to improvements in sample quality from a wet-chemical etching process. This confirms the presence of a trivial 2DHS in the 3DTI. The details of this coexistence are not yet understood and warrant further investigations.

Analysis of Aharonov-Bohm oscillations in a 3DTI ring structure showed the general feasibility of interference experiments in strained HgTe nanostructures with an optimized electronic setup. The phase coherence lengths of $l_\phi = 4...7$ µm extracted from the wet-etched device are large enough to make strained HgTe an interesting candidate for the investigation of other nanodevices, e.g. topological nanowires. The interference of chiral QH edge channels in the AB ring at quantizing magnetic fields could be explained with models known from AB rings in 2DESs [129]. The comparison shows that the bulk of the 3DTI strained HgTe remains fully insulating in nanostructures.

An alternative approach to experimentally probe QSH edge channels was attempted with a 2D antidot superlattice in a 2DTI. While periodic magnetoresistance oscillations are present in the inverted quantum well, the source of the unusual h/e-periodicity remains unclear. A conclusive attribution to helical edge channels is not possible, despite such theoretical findings by the Richter group, because of similar features found the topologically trivial reference sample. The occurrence of such oscillations in trivial antidot superlattice samples is unanticipated and warrants further investigations.

Nanowires of different geometries, fabricated from strained HgTe, were studied for magnetic fields along and perpendicular to the wire axis. The predicted transport signatures of TI nanowires [64], i.e. h/e-periodic Aharonov-Bohm oscillations and a switching of their phase with varying Fermi energy E_F, were observed. As they only prove surface transport, but not the topological nature of the states, the

1D subband structure was additionally probed. The spin-resolved nature of the topological surface states in 3DTI could be shown with a quantitative comparison to a simple model. The determined phase-coherence lengths of up to $l_\phi = 5$ µm confirm that the surface states form a coherent state around the perimeter of the nanowire. The robustness of the coherent state against more complicated nanowires cross sections can be explained with Klein tunnelling of the Dirac-like states. In ensemble averaged TI nanowire arrays, a lack of amplitude suppression was found for h/e-periodic oscillations. This is attributed to transport being nearly ballistic on the order of the circumference P, with only residual disorder remaining. In out-of-plane measurements at high magnetic fields, quantum oscillations, as well as quantized plateaus could be observed in nanowire Hall bars. A study of the oscillations in nanowires with different widths w showed a deviation from the $1/B$-periodicity expected for SdH oscillations due to the nanoscale sample dimensions. Finally, an attempt at quantum point contact constrictions was made. A new wafer and an optimized lithographic process made devices with only a few occupied subbands in the bulk energy gap possible. The presence of a 1D subband structure was confirmed. While a quantized conductance due to 1D confinement was not obtained, likely due to the confinement potential and inhomogeneous charge carrier distribution along the circumference, signs of a magnetic depopulation of subbands were observed.

The main result of this thesis is the realization of nearly ballistic topological nanowires on the basis of strained HgTe, along with probing their 1D subband structure with a novel approach. The obtained results, published in Ref. [31], lay the groundwork for further studies on such systems. Examples are topological nanowires with other, more intricate geometries such as varying cross sections, similar to 1D QH interferometers [128]. Of great interest in current research are devices which may potentially hosts Majorana quasiparticles, such as topological Josephson junctions based on induced superconductivity in HgTe nanowires [20]. In addition to previous experiments [157–159], here a transition from a topological to a trivial regime can be made by tuning the band structure via a magnetic flux. Further proposals for devices that allow spectroscopy of topological superconductivity with QPCs exist [155, 156]. An open question that needs to be resolved beforehand, is the lack of a quantization conductance in the current generation 3DTI point contacts.

A

Supplementary data

Data sets that are mentioned in, but disturb the flow of discussions in the respective chapters of the main text are collected in Appendix A.

A.1 Characterisation of strained 50nm HgTe wafer

The properties of the thinner 50 nm HgTe wafer (013)-oriented substrate have so far not been studied and do not necessarily have to match the well known 80 nm material. The results of a characterization of basic transport properties are shown in Fig. A.1 and discussed in the following. Using methods described in Cha. 5, the charge carrier densities of electrons n_s and holes p_s were extracted from measurements of Hall curves and Shubnikov-de Haas oscillations on a macroscopic Hall bar sample with a topgate stack identical to previously described experiments. Figure A.1(a) shows their dependence on the gate voltage V_g. For $V_\mathrm{g} < 1\,\mathrm{V}$, Hall curves are s-shaped due to the presence of both Dirac electrons and bulk holes. Fits with a two-carrier Drude model allow for the extraction of n_s^{Drude} and p_s^{Drude}. The position of the valence band edge at $V_\mathrm{g}^{E_\mathrm{v}} = 0.9\,\mathrm{V}$ is found by extrapolating p_s^{Drude}. For $V_\mathrm{g} > 1\,\mathrm{V}$, the Hall curves are linear. The extracted carrier density n_s^{Hall} is the total density of the system. Analysis of SdH oscillations yields different values for high and low-field oscillations. $n_s^{\mathrm{SdH,\ high}}$ values match those of the full system. Low-field oscillations yield $n_s^{\mathrm{SdH,\ low}}$, which represent the top surface only. This has been confirmed by magnetocapacitance measurements [25]. A change in the slope of the top surface charge carrier density n_s^{top} signifies the onset of the conduction band [51]. E_c is found to be at $V_\mathrm{g} = 1.95\,\mathrm{V}$. The total filling rate of $\alpha^{tot} = 2.18 \cdot 10^{11}\,\mathrm{cm^{-2}V^{-1}}$ matches the expected value from the plate capacitor model. The ratio of the filling rates for top and bottom surfaces is $\alpha^{top}/\alpha^{bot} = 57\,\%/43\,\%$.

Fig. A.1(b) shows the normalized magnetoresistance $R(B)/R(B=0)$ for small out-of-plane magnetic fields. At two gate voltages, an increased magnetoresistance is observed, which is caused by coexisting electrons and holes at the bulk band edges. The large feature around $V_\mathrm{g} = 0.5\,\mathrm{V}$ marks the charge neutrality

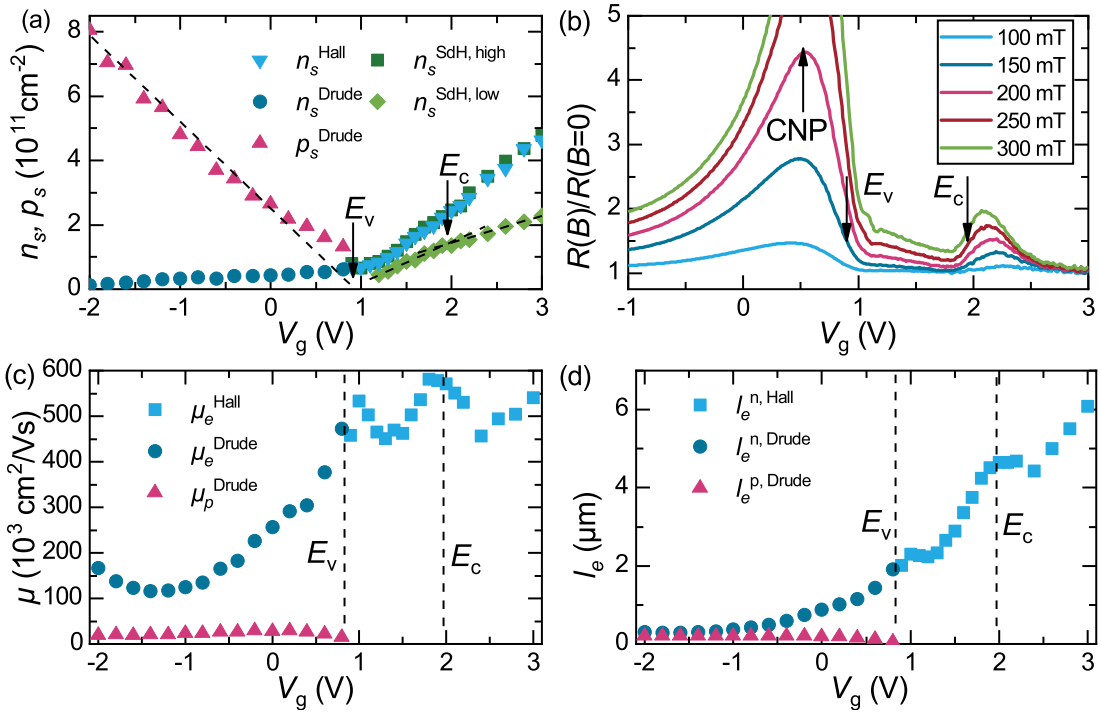

Figure A.1: Characterisation of the 50 nm strained HgTe wafer. (a) Charge carrier density n_s extracted from Hall bar measurements with linear Hall fits, the two-carrier Drude model and from high- and low-field SdH oscillations. The valence and conduction band edges are found at $V_g^{E_v} = 0.9\,\text{V}$ and $V_g^{E_c} = 1.95\,\text{V}$. (b) The normalized longitudinal resistance $R(B)/R(0)$ as a function of V_g. The high magnetoresistance features mark the CNP and the CB. The band edge positions E_c and E_v are marked with arrows. The corresponding mobilities μ_e and μ_p are shown in (c) and the mean free paths l_e^n and l_e^p in (d). Both μ_e and l_e^n are enhanced at two gate voltages, that coincide with the positions of E_v and E_c.

point, with E_v at its onset at 0.9 V. The onset of the second feature at 1.95 V marks the CB edge E_c. The extracted position of the bulk gap is consistent with analysis of charge carrier densities from Fig. A.1(a) and match the overall behaviour of 80 nm strained HgTe samples [51].

The respective mobilities of electrons μ_e and holes μ_p are plotted in Fig. A.1(c). The electron mobility μ_e has two maxima at 0.9 V and just below 2 V (marked by dashed lines), which indicate the lower and upper limits of the bulk gap. Maximum values lie between $500 \cdot 10^3$ and $600 \cdot 10^3\,\text{cm}^2/\text{Vs}$, which is higher than in the 80 nm wafers [51]. For $V_g < 0.9\,\text{V}$, μ_e quickly drops, with values as low as $100 \cdot 10^3\,\text{cm}^2/\text{Vs}$. In the CB regime, μ_e represents the average electron mobility of surface and bulk electrons, and begins to rise due to an increasing carrier density. Hole mobilities are low throughout and reach maximum values of only $28 \cdot 10^3\,\text{cm}^2/\text{Vs}$.

Mean free paths calculated from the mobilities in (c) via $l_e = \hbar/e\sqrt{2\pi n_s}\mu$ are shown in Fig. A.1(d). Bulk holes have a maximal mean free path of $l_e^p \approx 200\,\mathrm{nm}$. Again, values are much higher in the CB regime than in the VB for electron transport, with maximal values of $l_e^n = 6\,\mu\mathrm{m}$ at the edge of the investigated V_g-range at 3 V. In the bulk gap, mean free paths of 2 to 5 µm are observed.

A differentiation of mobilities and mean free paths into properties of bulk and Dirac electrons in the CB regime (or top and bottom surfaces in the bulk gap) is not possible like it is for charge carrier densities. The contributions of the different charge carrier types to the zero-field resistivity $\rho_{xx}(B = 0)$ would be required, but cannot be identified. The plotted values for μ_e and l_e^n were calculated with the case for $k_\mathrm{F} = \sqrt{2\pi n_s}$ and can therefore be regarded as a lower limit for the Dirac surface states. With mean free paths of $l_e > 2\,\mu\mathrm{m}$ for all gate voltages $V_\mathrm{g} > V_\mathrm{g}^{E_\mathrm{v}}$, the point contacts shown in Fig. 7.24 should be fully ballistic.

A.2 Characterisation of strained 80nm HgTe wafer

Capped wafers of 80 nm strained HgTe have been investigated thoroughly and key properties can be found in literature, c.f. Refs. [25, 51, 63]. To give a more detailed picture, characterization measurements from the Hall bar discussed in Sec. 5.1 are presented. The device is fabricated from wafer 120227, but results can be taken representatively for all investigated 80 nm strained HgTe wafers with the standard topgate stack of 30 nm SiO_2 and 100 nm Al_2O_3.

Figure A.2 shows a selection of essential transport properties of wafer 120227. In Fig. A.2(a), the charge carrier densities for electrons n_s and holes p_s is plotted for relevant gate voltages V_g. The filling rate is $\partial n_s/\partial V_\mathrm{g} = 2.2 \cdot 10^{11}\mathrm{cm}^{-2}\mathrm{V}^{-1}$, which agrees well with the theoretical value from the plate capacitor model. The CB edge is given by the change in filling rate of the low-field SdH oscillations at $V_\mathrm{g}^{E_\mathrm{c}} = 1.2\,\mathrm{V}$. The VB edge is found at $V_\mathrm{g}^{E_\mathrm{v}} = 0.25\,\mathrm{V}$. Due to the low carrier densities, the Fermi wavelength λ_F for surface electrons lies between 40 and 60 nm in the gap. The gate traces of the longitudinal and transversal resistivities are plotted in (b). The longitudinal resistivity $\rho_{xx}(V_\mathrm{g})$ has a characteristic feature where E_F enters the CB at $V_\mathrm{g}^{E_\mathrm{c}} = 1.2\,\mathrm{V}$. The Hall resistivity $\rho_{xy}(V_\mathrm{g})$ changes sign when E_F is tuned from n- to p-type conduction. Electron mobilities μ_e, plotted in Fig. A.2(c), are between $100 \cdot 10^3\,\mathrm{cm}^2/\mathrm{Vs}$ in the VB and over $400 \cdot 10^3\,\mathrm{cm}^2/\mathrm{Vs}$ in the gap. When E_F is in the CB, μ_e once again needs to be considered an average mobility of surface and bulk electrons. In this regime, it decreases to roughly $300 \cdot 10^3\,\mathrm{cm}^2/\mathrm{Vs}$. The mobilities of bulk holes are generally lower and are usually below $150 \cdot 10^3\,\mathrm{cm}^2/\mathrm{Vs}$ [24]. The mean free path lengths l_e^n of electrons are shown in Fig. A.2(d) and range from 1 to 4 µm in the investigated V_g-window,

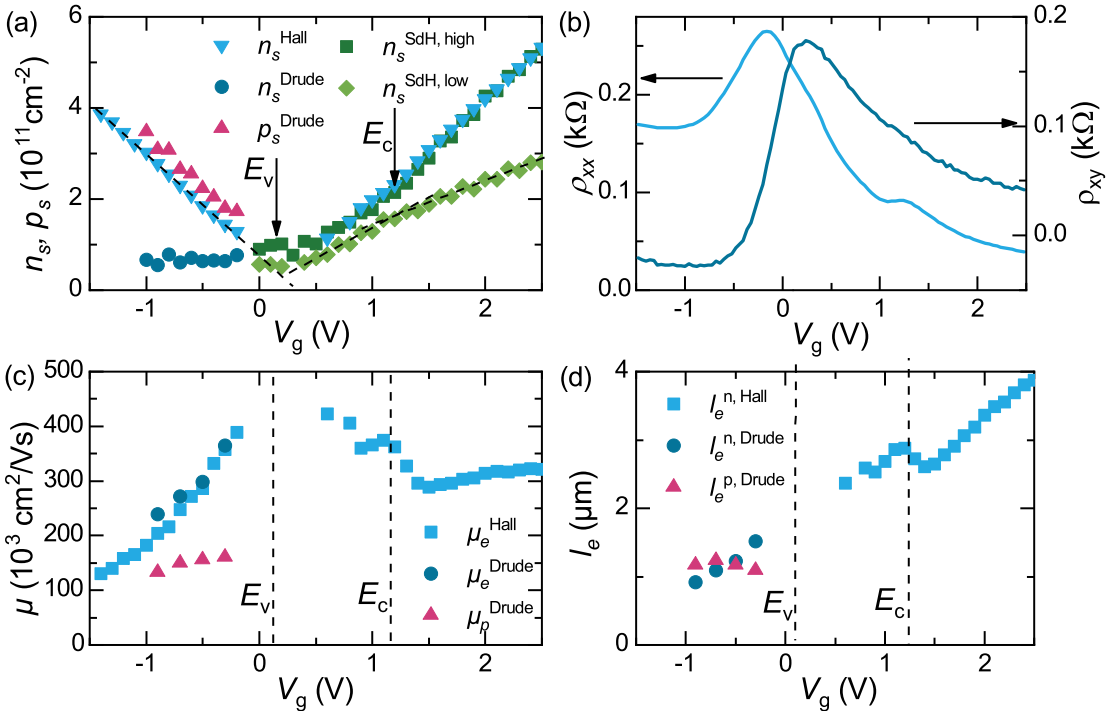

Figure A.2: Characterisation of an 80 nm strained HgTe wafer (120227). (a) Charge carrier densities n_s from linear Hall fits, the two-carrier Drude model and from high- and low-field SdH oscillations. The valence and conduction band edges are found at $V_g^{E_v} = 0.15\,\text{V}$ and $V_g^{E_c} = 1.2\,\text{V}$. (b) $\rho_{xx}(V_g)$ and $\rho_{xy}(V_g)$ are plotted for $B = 0$. In (c) and (d), the corresponding mobilities μ_e and μ_p and mean free paths l_e^n and l_e^p are shown.

with highest (lowest) values in the conduction (valence) band regime. In the bulk gap, values of 1.5 to 3 µm are seen.

A.3 Subband-induced oscillations in device s38w2

An analysis of subband-induced conductance oscillations is shown for device s38w2, whose parameters were used representatively in theoretical discussions by Kozlovsky *et al.* summarised in Sec. 7.6. Device s38w2, along with all other investigated HgTe nanowires, follows the principal trends and conclusions discussed in this work.

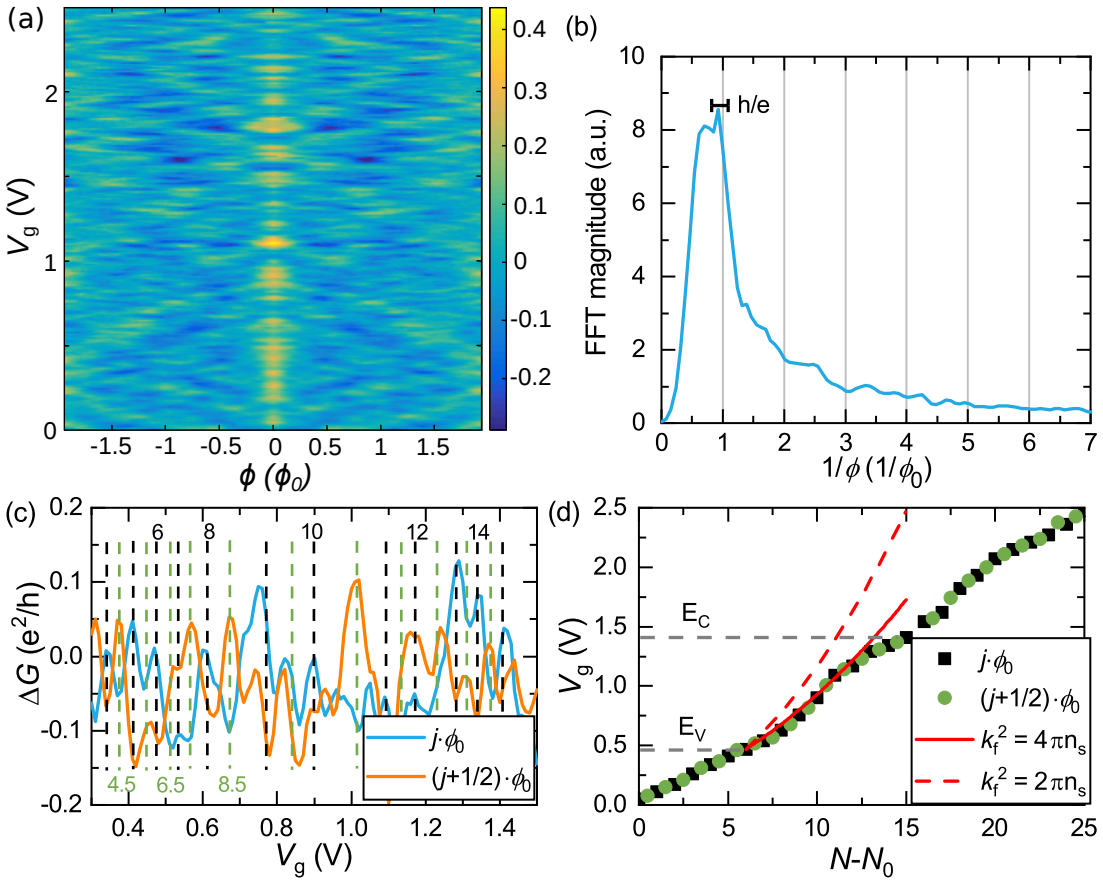

Figure A.3: (a) Color map of conductance corrections $\Delta G(V_g;\phi)$. (b) V_g-averaged FFT spectrum. (c) Extraction of subband spacing from $\Delta G(V_g)$ for integer and half-integer multiples of ϕ_0. Corresponding pairs of minima/maxima are marked by dashed lines. Their V_g-position is plotted against the subband index $N-N_0$ in (d), along with model curves (Eq. 7.5) for spin-resolved and spin-degenerate states. The experimental data is accurately described by the spin-resolved data.

A.4 Subband-induced oscillations in a nanowire on a (100) substrate

The experiments on strained HgTe nanowires in the main text consider devices fabricated from wafers with (013) surface orientation. Strained HgTe wafers with (100) surface orientation are also commonly used [54, 160]. To exclude any influence of the crystallographic surface orientation of the wafers, the experiments

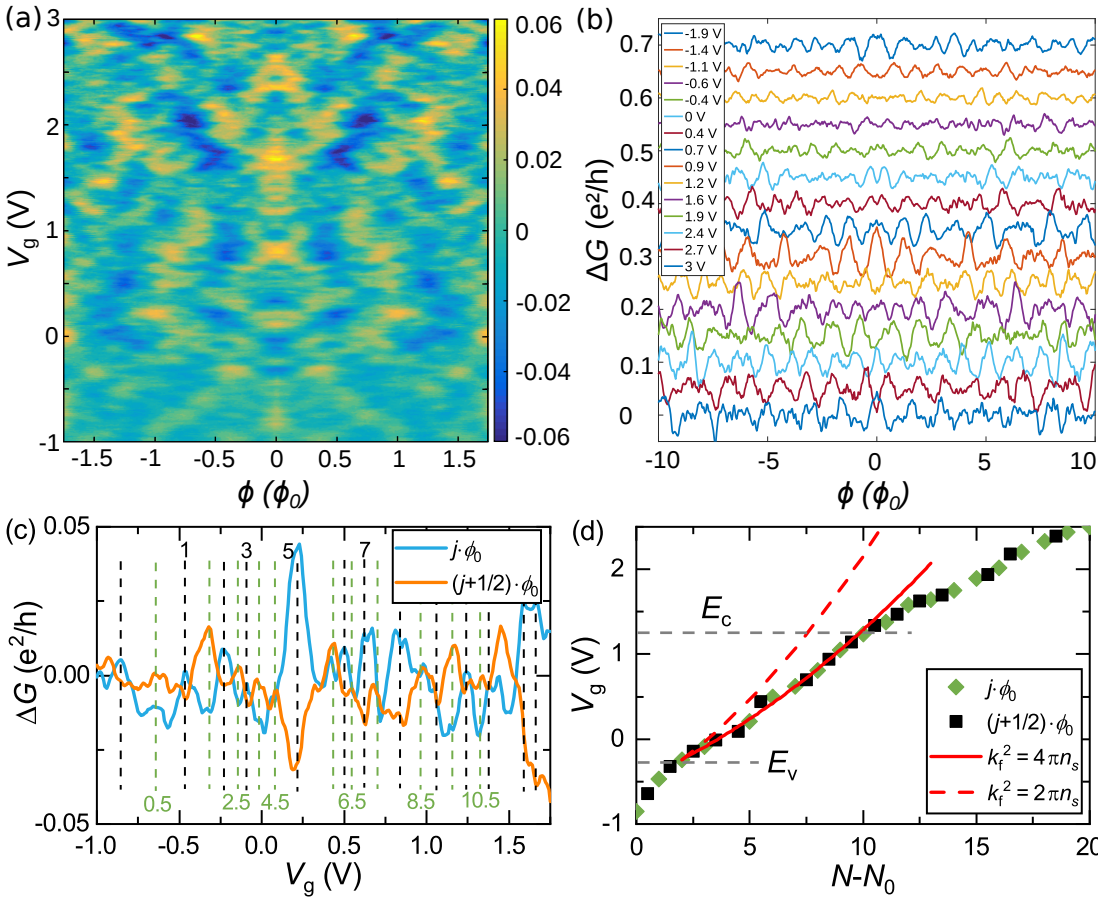

Figure A.4: Analysis of ϕ_0-periodic magnetoconductance- and subband-induced oscillations in a nanowire (device s58w1) on (100)-oriented substrate. (a) $\Delta G(V_g, \phi)$-map up to $1.75\phi_0$ at a high V_g-resolution of 10 mV. (b) Corresponding magnetoconductance traces at a selection of topgate voltages for fluxes up to $10\,\phi_0$. ϕ_0-periodic oscillations and switching behaviour are observed throughout both data sets. (c) The gate dependent conductance correction $\Delta G(V_g)$ is plotted for integer (blue) and half-integer (orange) multiples of ϕ_0. Corresponding pairs of minima and maxima are assigned a subband index. (d) The V_g-position of the subband indices is plotted and compared to spin-resolved and -degenerate cases of the model from Cha. 7.4 (Eq. 7.5). E_c and E_v denote the band edge positions, between which the model is valid.

were repeated with (100)-wafers. Two devices, namely s58w1 and s58w2, were built from wafer 170328 using the established processes. Apart from a thicker Al_2O_3-layer of 160 nm, their geometry and design is identical. The thicker dielectric layer was considered for all steps of the evaluation, including the electrostatic simulations. The data set along with analysis of the subband-induced oscillations is shown in Fig. A.4. Deviations from the established behaviour and the spin-resolved model for the 1D subband structure are not observed. An FFT spectrum of the AB oscillations, shown in Fig. A.5, confirms the h/e-periodicity. Peaks for higher-order oscillations are seen for $h/2e$ and $h/3e$.

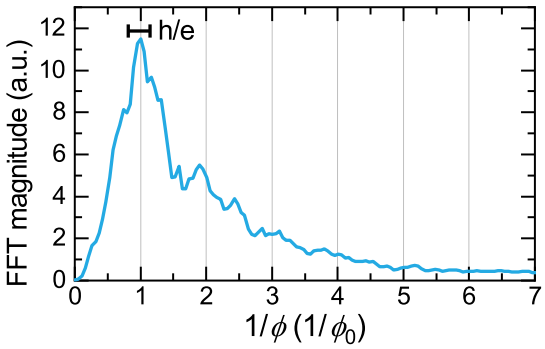

Figure A.5: V_g-averaged FFT spectrum computed from magnetoconductance traces spanning $> 9\phi_0$. The ϕ_0-periodic behaviour dominates, with minor contributions from higher-order $\phi_0/2$-periodic oscillations.

A.5 Subband-induced oscillations in a point contact device

Experiments in Sec. 7.9 cover topological nanowires, at the lower size limit of available fabrication processes. Measurements in magnetic fields parallel to the wire axis were performed to confirm the 1D band structure and topological nature of surface states in these devices. Analysis follows the methods described in Sec. 7.4 and agrees with the conclusions drawn therein.

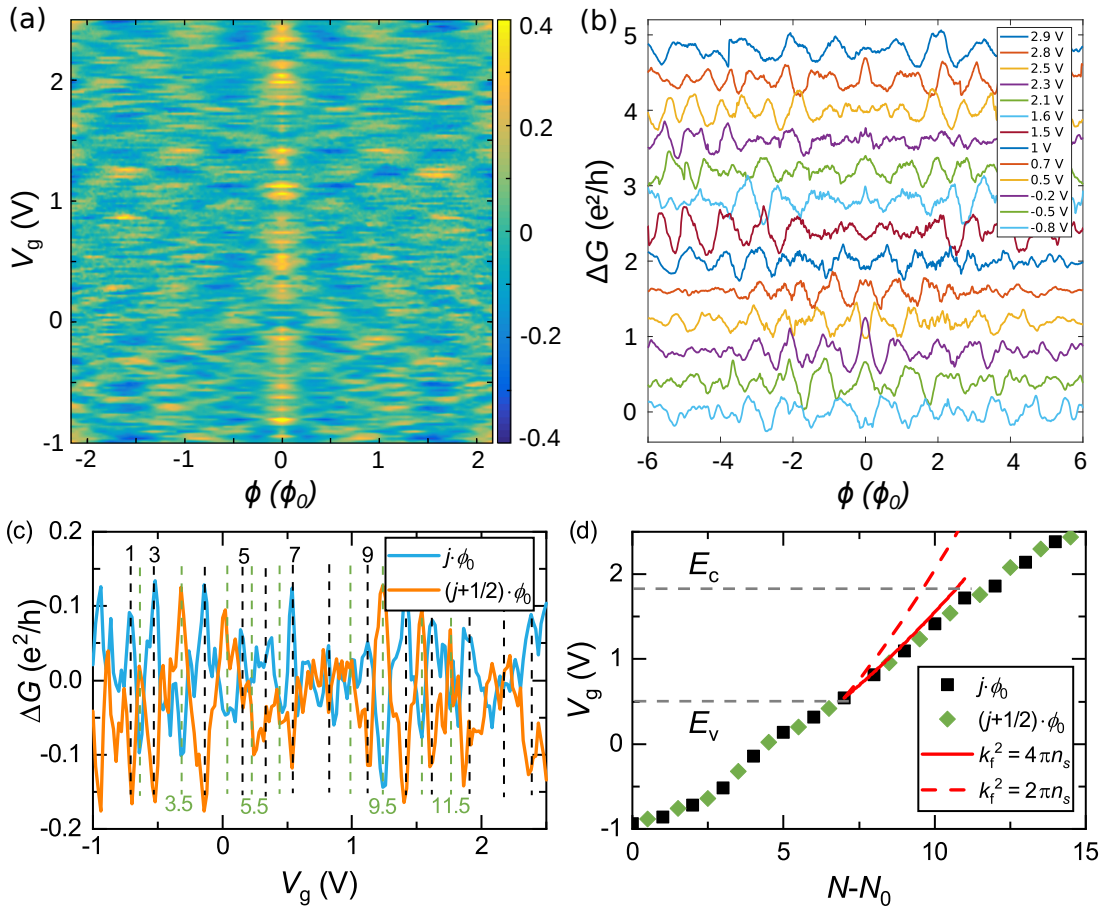

Figure A.6: Analysis of subband-induced oscillations in a representative QPC device (s63w1). (a) Conductance correction $\Delta G(\phi; V_g)$ visualized as a colour map. (b) Selection of magnetoconductance traces $\Delta G(\phi)$ with ϕ_0 periodic behaviour. (c) $\Delta G(V_g)$ extracted from (a) for integer and half-integer ϕ_0. Minima/maxima pairs are marked with dashed lines and assigned a subband index $N - N_0$. (d) The experimentally determined subband-positions are plotted and compared to model calculations for spin-resolved and spin-degenerate cases in the relevant bulk gap region.

B

Process documentation

The precise process parameters of lithographic, wet-chemical etch, oxide deposition and metallization processes described in Cha. 4 are listed in the following tables:

Material preparation

Standard cleaning

step description	parameters
acetone bath	1 min
acetone bath	1 min
isopropanol bath	1 min
dry	N_2

Splitting wafers

step description	parameters
protective resist	*Shipley S1813*, spin coating at 2000 rpm / 0 / 30 s, bake 3 min at 80 °C
scribe wafer	4×3.5 mm, scribe force 4-6 cm, repeat 2-3x
split wafer	split over glass edge with clean tape
standard cleaning	see above

Mesa

step description	parameters
standard cleaning	see above
spin coating	*S1813* photoresist at 6000 rpm / 6000 rpm/s / 30 s
bake	3 min at 80 °C
expose	80 s with mask *Novo* at 275 W
develop	30 s in *Microposit MF-26A* developer 30 s in DI water
wet-chemical etching	H_2O : ethylen glycol : Br_2 = 100 : 25 : 0.1, at 0 °C t min, shake every 30 s 5 s deionized (DI) water, dry with N_2
standard cleaning	see above

with etch times t varying for each wafer:
- 2 min 30 s on 8 nm HgTe wafer with $80 - 115$ nm cap
- 4 min 30 s on 8 nm HgTe wafer with 60 nm cap
- 3 min on 50 nm HgTe wafer with 60 nm cap

Nanostructures

step description	parameters
standard cleaning	see above
spin coating	PMMA 950K 4 % at 3000 rpm / 4000 rpm/s / 5 s and 8000 rpm / 1000 rpm/s / 30 s
bake	30 min at 80 °C
expose	EHT: 3 kV, aperture: 20 µm, area dose: D µC/cm^2
develop	90 s in MIBK : isopropanol = 1 : 3 30 s in isopropanol
wet-chemical etching	H_2O : ethylene glycol : Br_2 = 100 : 25 : 0.1, 0 °C t s
standard cleaning	see above
check with SEM	EHT: 3 kV, aperture: 30 μm
standard cleaning	see above

with area doses D and etch times t optimized for device type:
- 60 µC/cm^2 & 45 s for AB rings on 80 nm HgTe wafer with 60 nm cap
- 3.5 fC & 20 s for antidots on 8 nm HgTe wafer with 115 nm cap
- $50 - 60$ µC/cm^2 & 35 s for nanowires on 80 nm HgTe wafer with 60 nm cap
- 120 µC/cm^2 & 20 s for point contacts on 50 nm HgTe wafer with 60 nm cap

Topgate stack

Oxide layers

step description	parameters
standard cleaning	see above
PECVD	30 nm at 80 °C, 3×15 s
	at 710 sccm SiH_4, 170 sccm N_2O and 150 W
oxidization	wait 1 day between steps
ALD	100 nm at 80 °C, 0.015 s pulse, 66 s purge, 1000 cycles

Metallization - standard

step description	parameters
standard cleaning	see above
spin coating	*S1813* photoresist at 6000 rpm / 6000 rpm/s / 30 s
bake	3 min at 80 °C
expose	80 s with mask *Novo* at 275 W
develop	30 s in *Microposit MF-26A* developer
	30 s in DI water
thermal evaporation	no pre-sputtering
	Ti: 5 nm, 1.0 Å/s
	Au: 80 nm, 1.5 Å/s
lift-off	acetone at 60 °C for 3 h
	flush sample with acetone from syringe
	optical check in isopropanol bath
	dry with N_2

Contacts

step description	parameters
solder	6 W soldering iron at 7 V, 0.9 A
	lightly scratch oxide with needle
	$2-3$ quick dabs of In onto contact pad
chip carrier	mount sample with two-component silver epoxy
	EpoTek EE129-4, mix 1:1, bake 2h at 80 °C
bond	1st bond on chip carrier, 2nd on bare contact pad
	push loose Au-wire into In with tweezers

C

Data analysis methods

A number of data treatment techniques were used in the data analysis for this thesis. They are based on well established methods, such as the Savitzky-Golay filtering [136] and the fast Fourier transform algorithms. To speed up processing of large data sets, scripts were developed in MATLAB to handle full data sets at once instead of a curve-by-curve approach. The typical work flow of data processing was as follows: Data sets, measured with the Lab::Measurement framework [161], are imported into MATLAB using a data class structure begun by C. Butschkow. Processing methods can be applied to all curves (blocks) of a data set. Several functions were added to allow for flexible handling of data by creating and deleting columns, extracting arbitrary curves, and plotting full or subsets of curves. Data sets are then treated by removing the magnet hysteresis, removing a smoothly varying background, calculating Fourier spectra and interpolation of Landau fan plots as necessary. Details of the implementations are discussed in the following sections.

Hysteresis compensation of superconducting magnet

Superconducting magnets have an unavoidable hysteresis around $B = 0$ stemming from trapped vortices. This behaviour becomes harder to control by engineering in large magnets, such as in the 17 T magnet of the available *Oxford Instruments Kelvinox TLM* dilution refrigeration system. The exact hysteretic shift depends on measurement parameters, i.e. the highest previous applied field, but routinely reaches values of up to 31 mT in this setup. Shifts of this size influence data analysis, and make it necessary to treat data sets accordingly. While actual behaviour is more intricate, it has proven practical to compensate for the hysteretic artefacts by shifting the magnetic field scale so that zero-field features are aligned with $B = 0$. Increasingly smaller shifts, in a linearly declining fashion, are applied towards higher fields. Most recorded data sets feature signatures at $B = 0$, either by WAL, zeros of the Hall signal or oscillation patterns with extrema. Fig. C.1 presents three consecutive sweeps with raw data shown in (a) and treated traces in (b). Treatment of the data with this method sufficiently

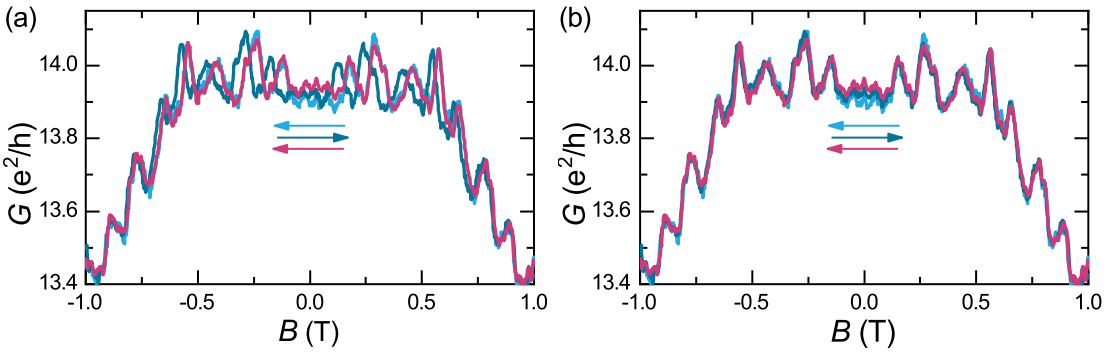

Figure C.1: Removal of hysteretic behaviour from h/e-periodic signals in a topological nanowire. (a) Raw and (b) treated traces are shown. The coloured arrows denote the respective sweep directions. Traces were recorded successively in the order *light blue, dark blue* and *red*.

removes hysteretic artefacts from the superconducting magnet system so that further analysis becomes possible.

Landau fan chart interpolation

The colour plots in Cha. 5 were recorded with a very high resolution at low fields. To avoid having to measure at such resolution throughout the plotted field range, which would have required several weeks, the pattern of Landau fan charts was

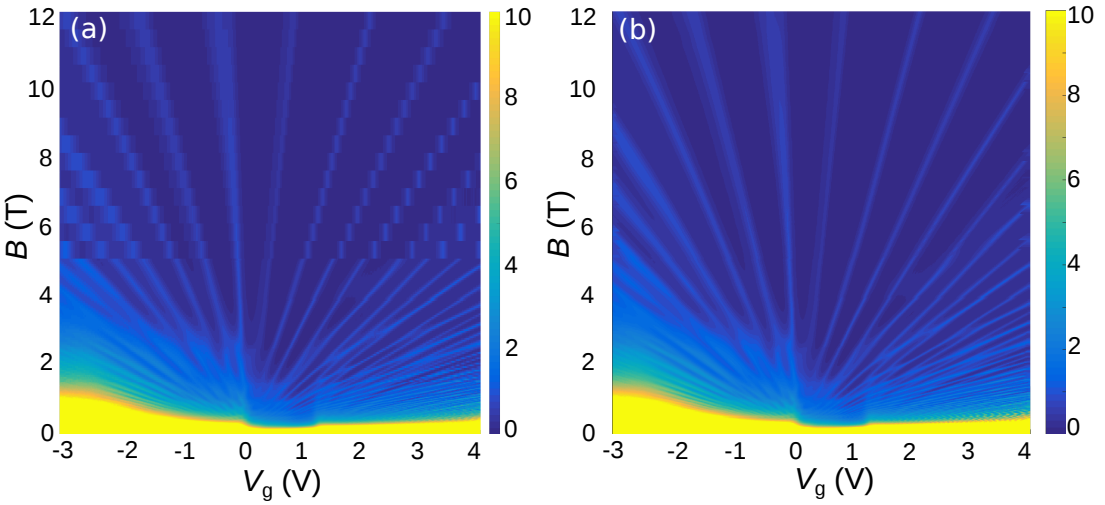

Figure C.2: Interpolation of data sets with Landau fans. The conductivity $\sigma_{xx}(e^2/h)$ is plotted as a function of V_g and B (a) before and (b) after interpolation of the data set.

exploited for interpolation of the data set. In the regime of high magnetic fields, measurements can then be carried out at a lower resolution, and interpolation can make up for the lack of visual quality. An algorithm written by D.A. Kozlov [51] was ported to MATLAB for this work.

The method exploits the linearity of Landau fan charts in $\sigma_{xx}(V_g, B)$-plots. For each region of VB, bulk energy gap and conduction band regime, a virtual charge point is defined. This point is given by the intersection of a Landau level with the axis at $B = 0$. Interpolated data points are then calculated from the raw data set along lines of linear slope going outward from the virtual charge points. Interpolation resolution can be arbitrarily chosen but is generally set as the highest experimental resolution in the data set. Data at small magnet fields is commonly measured with the highest resolution as Landau level features are then most dense. This means that in the region of small magnetic fields and intricate and complicated Landau level interplay, the data set is not affected.

Background removal

In transport experiments, the essentially interesting effects are often overlapped by other features in the magnetoconductance curve. When the scale of features that are to be analysed is clearly discernible from a smoothly varying background, they can be separated. This is done in the same way as smoothing a noisy signal to increase the signal-to-noise ratio, except for low frequency features.

The Savitzky-Golay filter can be summarized as a moving average by polynomial regressions. Its big advantage over other methods, such as local regressions, is the accurate reproduction of the signal features like extrema positions. This is important for the accurate analysis of periodic signals such as in Cha. 7.3. In this case, the Savitzky-Golay filter was applied using MATLAB's built-in implementation through the

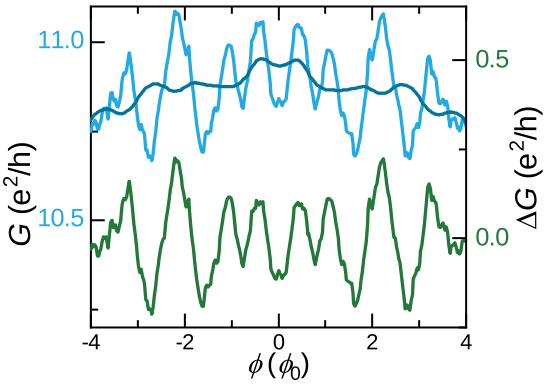

Figure C.3: Background subtraction with the Savitzky-Golay filter. A moving average of the raw curve (top, light blue) is calculated (top, dark blue). Subtraction yields the conductance correction ΔG (bottom, green).

```
smooth(Xdata, Ydata, span, 'sgolay')
```

function, where *span* is the size of the moving average interval. An example is shown in Fig. C.3 The smoothed curve was subtracted from the original data, so that higher frequency features remain unaffected. In the case Aharonov-Bohm oscillations, the choice for the *span* interval can influence the subsequent FFT spectra. A *span* that is too small will lead to oscillations with higher frequencies being filtered. This translates to cutting off low-frequency parts of the FFT spectrum and should be avoided. A choice for the *span* interval of $\Delta B_{\text{span}} > 2 \times \Delta B_{h/e}$, i.e. $\phi_{0,\text{cut-off}} < \phi_0$ has proven reliable.

Fast Fourier transform

For spectral analysis of Aharonov-Bohm oscillations in Cha. 6 and 7, Fourier transforms of discrete data sets were necessary. Since quantitative deductions were to be drawn, an accurate reproduction of periodic features was crucial. With this in mind, tests were made with regard to window functions and splitting the data set into intervals.

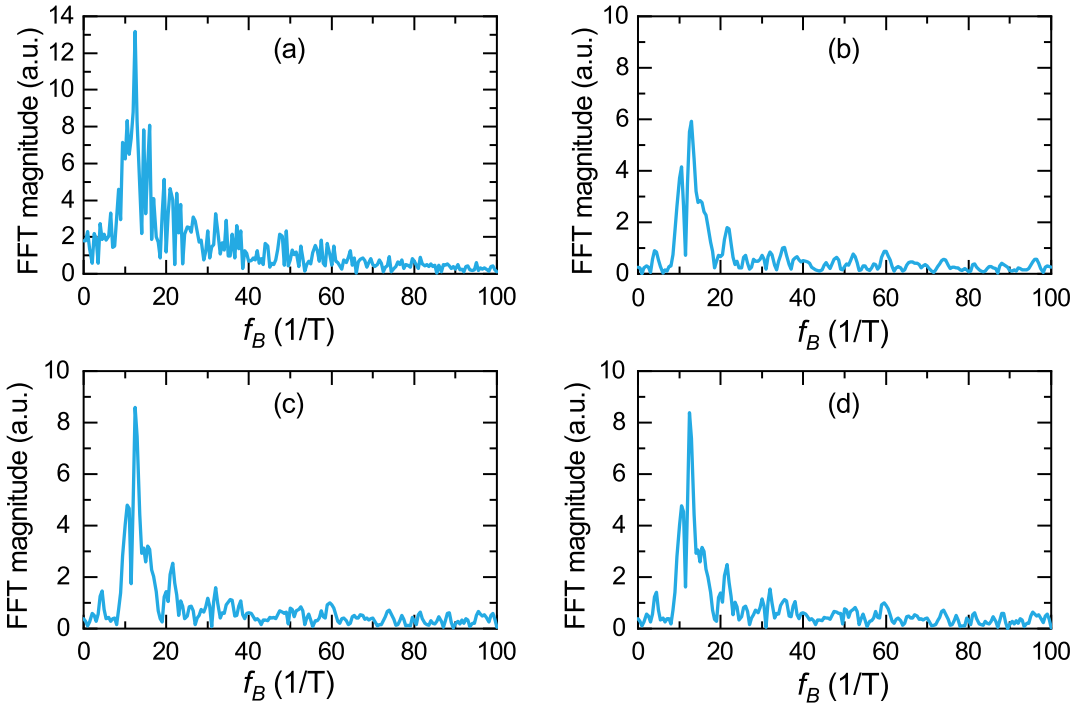

Figure C.4: Comparison of window functions for FFT on a h/e-periodic signal of a topological nanowire with: (a) no window (rectangular), (b) a FlatTop window, (c) a Chebyshev window, and (d) a Blackman-Harris window.

Window functions are needed to reduce side-lobe features in FFT spectra, which occur due to the finite length of the data sets. FlatTop, Chebyshev and Blackman-Harris were considered for their optimization in this regard. Tests show they perform equally well with minor differences in magnitude height [see Fig. C.4]. The Chebyshev window was chosen for its strong side-lobe suppression compared to the magnitude of the main signal.

A further detail implemented in the standard FFT analysis is calculating FFTs of a signal piece-by-piece. The magnetoconductance curve is split into a number of sections and the FFTs calculated for each of them. Finally, the average over all sections is calculated. This helps in reducing the influence of noise and conductance fluctuations on the resulting FFT spectra.

Bibliography

[1] C. Monroe and J. Kim. *Scaling the ion trap quantum processor.* Science **339**, 1164–1169 (2013).

[2] V. Dobrovitski, G. Fuchs, A. Falk, C. Santori, and D. Awschalom. *Quantum control over single spins in diamond.* Annual Review of Condensed Matter Physics **4**, 23–50 (2013).

[3] C. Kloeffel and D. Loss. *Prospects for spin-based quantum computing in quantum dots.* Annual Review of Condensed Matter Physics **4**, 51–81 (2013).

[4] M. H. Devoret and R. J. Schoelkopf. *Superconducting circuits for quantum information: An outlook.* Science **339**, 1169–1174 (2013).

[5] C. L. Kane and E. J. Mele. *Quantum spin Hall effect in graphene.* Physical Review Letters **95**, 226801 (2005).

[6] C. L. Kane and E. J. Mele. *Z_2 topological order and the quantum spin Hall effect.* Physical Review Letters **95**, 146802 (2005).

[7] M. König, S. Wiedmann, C. Brüne, A. Roth, H. Buhmann, L. W. Molenkamp, X.-L. Qi, and S.-C. Zhang. *Quantum spin Hall insulator state in HgTe quantum wells.* Science **318**, 766–770 (2007).

[8] J. M. Kosterlitz and D. J. Thouless. *Ordering, metastability and phase transitions in two-dimensional systems.* Journal of Physics C: Solid State Physics **6**, 1181–1203 (1973).

[9] L. Fu and C. L. Kane. *Superconducting proximity effect and Majorana fermions at the surface of a topological insulator.* Physical Review Letters **100**, 096407 (2008).

[10] C. Beenakker. *Search for Majorana fermions in superconductors.* Annual Review of Condensed Matter Physics **4**, 113–136 (2013).

[11] B. J. Wieder, F. Zhang, and C. L. Kane. *Signatures of Majorana fermions in topological insulator Josephson junction devices.* Physical Review B **89**, 075106 (2014).

[12] E. Majorana. *Teoria simmetrica dell'elettrone e del positrone.* Il Nuovo Cimento **14**, 171–184 (1937).

[13] E. Majorana and L. Maiani, "A symmetric theory of electrons and positrons," in *Ettore Majorana Scientific Papers*, 201–233, Springer Berlin Heidelberg.

[14] A. Y. Kitaev. *Unpaired Majorana fermions in quantum wires.* Physics-Uspekhi **44**, 131–136 (2001).

[15] A. Y. Kitaev. *Fault-tolerant quantum computation by anyons.* Annals of Physics **303**, 2–30 (2003).

[16] S. D. Sarma, M. Freedman, and C. Nayak. *Majorana zero modes and topological quantum computation.* npj Quantum Information **1**, 15001 (2015).

[17] S. Nadj-Perge, I. K. Drozdov, J. Li, H. Chen, S. Jeon, J. Seo, A. H. MacDonald, B. A. Bernevig, and A. Yazdani. *Observation of Majorana fermions in ferromagnetic atomic chains on a superconductor.* Science **346**, 602–607 (2014).

[18] R. Deacon, J. Wiedenmann, E. Bocquillon, F. Domínguez, T. Klapwijk, P. Leubner, C. Brüne, E. Hankiewicz, S. Tarucha, K. Ishibashi, H. Buhmann, and L. Molenkamp. *Josephson radiation from gapless Andreev bound states in HgTe-based topological junctions.* Physical Review X **7**, 021011 (2017).

[19] V. Mourik, K. Zuo, S. M. Frolov, S. R. Plissard, E. P. A. M. Bakkers, and L. P. Kouwenhoven. *Signatures of Majorana fermions in hybrid superconductor-semiconductor nanowire devices.* Science **336**, 1003–1007 (2012).

[20] A. Cook and M. Franz. *Majorana fermions in a topological-insulator nanowire proximity-coupled to an s-wave superconductor.* Physical Review B **84**, 201105 (2011).

[21] A. Roth, C. Brüne, H. Buhmann, L. W. Molenkamp, J. Maciejko, X.-L. Qi, and S.-C. Zhang. *Nonlocal transport in the quantum spin Hall state.* Science **325**, 294–297 (2009).

[22] B. A. Bernevig, T. L. Hughes, and S.-C. Zhang. *Quantum spin Hall effect and topological phase transition in HgTe quantum wells.* Science **314**, 1757–1761 (2006).

[23] L. Fu, C. L. Kane, and E. J. Mele. *Topological insulators in three dimensions.* Physical Review Letters **98**, 106803 (2007).

[24] D. A. Kozlov, Z. D. Kvon, N. N. Mikhailov, S. A. Dvoretskii, S. Weishäupl, Y. Krupko, and J.-C. Portal. *Quantum Hall effect in HgTe quantum wells at nitrogen temperatures.* Applied Physics Letters **105**, 132102 (2014).

[25] D. Kozlov, D. Bauer, J. Ziegler, R. Fischer, M. Savchenko, Z. Kvon, N. Mikhailov, S. Dvoretsky, and D. Weiss. *Probing quantum capacitance in a 3D topological insulator.* Physical Review Letters **116**, 166802 (2016).

[26] H. Peng, K. Lai, D. Kong, S. Meister, Y. Chen, X.-L. Qi, S.-C. Zhang, Z.-X. Shen, and Y. Cui. *Aharonov-Bohm interference in topological insulator nanoribbons*. Nature Materials **9**, 225–229 (2010).

[27] S. Cho, B. Dellabetta, R. Zhong, J. Schneeloch, T. Liu, G. Gu, M. J. Gilbert, and N. Mason. *Aharonov-Bohm oscillations in a quasi-ballistic three-dimensional topological insulator nanowire*. Nature Communications **6**, 7634 (2015).

[28] L. A. Jauregui, M. T. Pettes, L. P. Rokhinson, L. Shi, and Y. P. Chen. *Magnetic field-induced helical mode and topological transitions in a topological insulator nanoribbon*. Nature Nanotechnology **11**, 345–351 (2016).

[29] S. Weishäupl. *Quanteninterferenzeffekte in topologischen Isolatoren und magnetischen Halbleitern*. Universität Regensburg, Dissertation, 2014.

[30] S. S. Hong, Y. Zhang, J. J. Cha, X.-L. Qi, and Y. Cui. *One-dimensional helical transport in topological insulator nanowire interferometers*. Nano Letters **14**, 2815-2821 (2014).

[31] J. Ziegler, R. Kozlovsky, C. Gorini, M.-H. Liu, S. Weishäupl, H. Maier, R. Fischer, D. A. Kozlov, Z. D. Kvon, N. Mikhailov, S. A. Dvoretsky, K. Richter, and D. Weiss. *Probing spin helical surface states in topological HgTe nanowires*. Physical Review B **97**, 035157 (2018).

[32] S.-Q. Shen. *Topological insulators*. Springer Berlin Heidelberg, 2012.

[33] M. Franz and L. Molenkamp. *Topological Insulators*. Elsevier, 2013.

[34] D. Xiao, M.-C. Chang, and Q. Niu. *Berry phase effects on electronic properties*. Reviews of Modern Physics **82**, 1959–2007 (2010).

[35] K. von Klitzing, G. Dorda, and M. Pepper. *New method for high-accuracy determination of the fine-structure constant based on quantized Hall resistance*. Physical Review Letters **45**, 494–497 (1980).

[36] D. J. Thouless, M. Kohmoto, M. P. Nightingale, and M. den Nijs. *Quantized Hall conductance in a two-dimensional periodic potential*. Physical Review Letters **49**, 405–408 (1982).

[37] F. D. M. Haldane. *Model for a Quantum Hall Effect without Landau Levels: Condensed-Matter Realization of the "Parity Anomaly"*. Physical Review Letters **61**, 2015–2018 (1988).

[38] K. S. Novoselov. *Electric field effect in atomically thin carbon films*. Science **306**, 666–669 (2004).

[39] B. A. Bernevig and T. L. Hughes. *Topological insulators and topological superconductors*. Princeton University Press, 2013.

[40] M. Z. Hasan and C. L. Kane. *Colloquium: Topological insulators.* Reviews of Modern Physics **82**, 3045–3067 (2010).

[41] J. E. Moore and L. Balents. *Topological invariants of time-reversal-invariant band structures.* Physical Review B **75**, 121306 (2007).

[42] P. Capper. *Properties of Narrow-Gap Cadmium-Based Compounds.* IEE Proceedings - Optoelectronics **142**, 315- (1995).

[43] N. N. Berchenko and M. V. Pashkovskiĭ. *Mercury telluride - a zero-gap semiconductor.* Soviet Physics Uspekhi **19**, 462 (1976).

[44] Z. D. Kvon, E. B. Olshanetsky, D. A. Kozlov, E. Novik, N. N. Mikhailov, and S. A. Dvoretsky. *Two-dimensional semimetal in HgTe-based quantum wells.* Low Temperature Physics **37**, 202-209 (2011).

[45] D. A. Kozlov, Z. D. Kvon, N. N. Mikhailov, and S. A. Dvoretskii. *Quantum hall effect in a system of gapless Dirac fermions in HgTe quantum wells.* JETP Letters **100**, 724–730 (2015).

[46] D. A. Kozlov, Z. D. Kvon, N. N. Mikhailov, and S. A. Dvoretsky. *Weak localization of Dirac fermions in HgTe quantum wells.* JETP Letters **96**, 730–734 (2013).

[47] K. Suzuki, Y. Harada, K. Onomitsu, and K. Muraki. *Edge channel transport in the InAs/GaSb topological insulating phase.* Physical Review B **87**, 235311 (2013).

[48] L. Fu and C. L. Kane. *Topological insulators with inversion symmetry.* Physical Review B **76**, 045302 (2007).

[49] X. Dai, T. L. Hughes, X.-L. Qi, Z. Fang, and S.-C. Zhang. *Helical edge and surface states in HgTe quantum wells and bulk insulators.* Physical Review B **77**, 125319 (2008).

[50] J. Ruan, S.-K. Jian, H. Yao, H. Zhang, S.-C. Zhang, and D. Xing. *Symmetry-protected ideal Weyl semimetal in HgTe-class materials.* Nature Communications **7**, 11136 (2016).

[51] D. A. Kozlov, Z. D. Kvon, E. B. Olshanetsky, N. N. Mikhailov, S. A. Dvoretsky, and D. Weiss. *Transport properties of a 3D topological insulator based on a strained high-mobility HgTe film.* Physical Review Letters **112**, 196801 (2014).

[52] C. Brüne, C. Thienel, M. Stuiber, J. Böttcher, H. Buhmann, E. G. Novik, C.-X. Liu, E. M. Hankiewicz, and L. W. Molenkamp. *Dirac-screening stabilized surface-state transport in a topological insulator.* Physical Review X **4**, 041045 (2014).

[53] S.-C. Wu, B. Yan, and C. Felser. *Ab initio study of topological surface states of strained HgTe.* Europhysics Letters **107**, 57006 (2014).

[54] C. Brüne, C. X. Liu, E. G. Novik, E. M. Hankiewicz, H. Buhmann, Y. L. Chen, X.-L. Qi, Z. X. Shen, S.-C. Zhang, and L. W. Molenkamp. *Quantum Hall effect from the topological surface states of strained bulk HgTe.* Physical Review Letters **106** (2011).

[55] K.-M. Dantscher, D. A. Kozlov, P. Olbrich, C. Zoth, P. Faltermeier, M. Lindner, G. V. Budkin, S. A. Tarasenko, V. V. Belkov, Z. D. Kvon, N. N. Mikhailov, S. A. Dvoretsky, D. Weiss, B. Jenichen, and S. D. Ganichev. *Cyclotron-resonance-assisted photocurrents in surface states of a three-dimensional topological insulator based on a strained high-mobility HgTe film.* Physical Review B **92**, 165314 (2015).

[56] K. S. Novoselov, A. K. Geim, S. V. Morozov, D. Jiang, M. I. Katsnelson, I. V. Grigorieva, S. V. Dubonos, and A. A. Firsov. *Two-dimensional gas of massless Dirac fermions in graphene.* Nature **438**, 197–200 (2005).

[57] M. I. Katsnelson. *Graphene: carbon in two dimensions.* Materials Today **10**, 20–27 (2007).

[58] A. A. Taskin and Y. Ando. *Berry phase of nonideal Dirac fermions in topological insulators.* Physical Review B **84** (2011).

[59] A. A. Taskin, Z. Ren, S. Sasaki, K. Segawa, and Y. Ando. *Observation of Dirac holes and electrons in a topological insulator.* Physical Review Letters **107**, 016801 (2011).

[60] D. Hsieh, D. Qian, L. Wray, Y. Xia, Y. S. Hor, R. J. Cava, and M. Z. Hasan. *A topological Dirac insulator in a quantum spin Hall phase.* Nature **452**, 970–974 (2008).

[61] Y. Xia, D. Qian, D. Hsieh, L. Wray, A. Pal, H. Lin, A. Bansil, D. Grauer, Y. S. Hor, R. J. Cava, and M. Z. Hasan. *Observation of a large-gap topological-insulator class with a single Dirac cone on the surface.* Nature Physics **5**, 398–402 (2009).

[62] H. Zhang, C.-X. Liu, X.-L. Qi, X. Dai, Z. Fang, and S.-C. Zhang. *Topological insulators in Bi_2Se_3, Bi_2Te_3 and Sb_2Te_3 with a single Dirac cone on the surface.* Nature Physics **5**, 438–442 (2009).

[63] H. Maier, J. Ziegler, R. Fischer, D. Kozlov, Z. D. Kvon, N. Mikhailov, S. A. Dvoretsky, and D. Weiss. *Ballistic geometric resistance resonances in a single surface of a topological insulator.* Nature Communications **8**, 2023 (2017).

[64] J. H. Bardarson, P. W. Brouwer, and J. E. Moore. *Aharonov-Bohm oscillations in disordered topological insulator nanowires.* Physical Review Letters **105**, 156803 (2010).

[65] T. Ando, A. B. Fowler, and F. Stern. *Electronic properties of two-dimensional systems.* Reviews of Modern Physics **54**, 437–672 (1982).

[66] P. Y. Yu and M. Cardona. *Fundamentals of Semiconductors.* Springer Berlin Heidelberg, 2010.

[67] S. D. Sarma, S. Adam, E. H. Hwang, and E. Rossi. *Electronic transport in two-dimensional graphene.* Reviews of Modern Physics **83**, 407–470 (2011).

[68] P. Drude. *Zur Elektronentheorie der Metalle.* Annalen der Physik **306**, 566–613 (1900).

[69] T. Ihn. *Semiconductor Nanostructures.* Oxford University Press, 2009.

[70] L. Schubnikow and W. J. de Haas. *A new phenomenon in the change of resistance in a magnetic field of single crystals of bismuth.* Nature **126**, 500–500 (1930).

[71] Y.-Y. Zhang, X.-R. Wang, and X. C. Xie. *Three-dimensional topological insulator in a magnetic field: chiral side surface states and quantized Hall conductance.* Journal of Physics: Condensed Matter **24**, 015004 (2011).

[72] T. Heinzel. *Mesoscopic electronics in solid state nanostructures.* Wiley-VCH Verlag GmbH, second ed., 2006.

[73] D. Weiss, C. Zhang, R. R. Gerhardts, and G. Klitzing, K. von andWeimann. *Density of states in a two-dimensional electron gas in the presence of a one-dimensional superlattice potential.* Physical Review B **39**, 13020–13023 (1989).

[74] D. Weiss, M. L. Roukes, A. Menschig, P. Grambow, K. von Klitzing, and G. Weimann. *Electron pinball and commensurate orbits in a periodic array of scatterers.* Physical Review Letters **66**, 2790–2793 (1991).

[75] Y. Aharonov and D. Bohm. *Significance of electromagnetic potentials in the quantum theory.* Physical Review **115**, 485–491 (1959).

[76] W. Ehrenberg and R. E. Siday. *The refractive index in electron optics and the principles of dynamics.* Proceedings of the Physical Society. Section B **62**, 8–21 (1949).

[77] S. Datta, M. R. Melloch, S. Bandyopadhyay, R. Noren, M. Vaziri, M. Miller, and R. Reifenberger. *Novel interference effects between parallel quantum wells.* Physical Review Letters **55**, 2344–2347 (1985).

[78] S. Datta and S. Bandyopadhyay. *Aharonov-Bohm effect in semiconductor microstructures.* Physical Review Letters **58**, 717–720 (1987).

[79] C. Beenakker and H. van Houten, "Quantum transport in semiconductor nanostructures," in *Semiconductor heterostructures and nanostructures* (H. Ehrenreich and D. Turnbull, eds.), vol. 44 of *Solid State Physics*, 1 - 228, Academic Press, (1991).

[80] R. A. Webb, S. Washburn, C. P. Umbach, and R. B. Laibowitz. *Observation of h/e Aharonov-Bohm oscillations in normal-metal rings.* Physical Review Letters **54**, 2696–2699 (1985).

[81] G. Timp, A. M. Chang, J. E. Cunningham, T. Y. Chang, P. Mankiewich, R. Behringer, and R. E. Howard. *Observation of the Aharonov-Bohm effect for $\omega_c\tau > 1$.* Physical Review Letters **58**, 2814–2817 (1987).

[82] K. Ishibashi, Y. Takagaki, K. Gamo, S. Namba, S. Ishida, K. Murase, Y. Aoyagi, and M. Kawabe. *Observation of Aharonov-Bohm magnetoresistance oscillations in selectively doped GaAs-AlGaAs submicron structures.* Solid State Communications **64**, 573–576 (1987).

[83] D. Sharvin and Y. Sharvin. *Magnetic flux quantization in a cylindrical film of a normal metal.* JETP Letters **34**, 272–275 (1981).

[84] G. Bergmann. *Weak anti-localization - An experimental proof for the destructive interference of rotated spin 1/2.* Solid State Communications **42**, 815–817 (1982).

[85] C. P. Umbach, C. V. Haesendonck, R. B. Laibowitz, S. Washburn, and R. A. Webb. *Direct observation of ensemble averaging of the Aharonov-Bohm effect in normal-metal loops.* Physical Review Letters **56**, 386–389 (1986).

[86] S. Washburn and R. A. Webb. *Aharonov-Bohm effect in normal metal quantum coherence and transport.* Advances in Physics **35**, 375–422 (1986).

[87] H. Ajiki and T. Ando. *Aharonov-Bohm effect in carbon nanotubes.* Physica B: Condensed Matter **201**, 349–352 (1994).

[88] H. Ajiki and T. Ando. *Aharonov-Bohm effect on magnetic properties of carbon nanotubes.* Physica B: Condensed Matter **216**, 358–361 (1996).

[89] H. Ajiki and T. Ando. *Carbon nanotubes as quantum wires on a cylinder surface.* Solid State Communications **102**, 135–142 (1997).

[90] T. Ando and H. Suzuura. *Presence of perfectly conducting channel in metallic carbon nanotubes.* Journal of the Physical Society of Japan **71**, 2753–2760 (2002).

[91] J. H. Bardarson and J. E. Moore. *Quantum interference and Aharonov-Bohm oscillations in topological insulators*. Reports on Progress in Physics **76**, 056501 (2013).

[92] D. A. Wharam, T. J. Thornton, R. Newbury, M. Pepper, H. Ahmed, J. E. F. Frost, D. G. Hasko, D. C. Peacock, D. A. Ritchie, and G. A. C. Jones. *One-dimensional transport and the quantisation of the ballistic resistance*. Journal of Physics C: Solid State Physics **21**, L209–L214 (1988).

[93] B. J. van Wees, H. van Houten, C. W. J. Beenakker, J. G. Williamson, L. P. Kouwenhoven, D. van der Marel, and C. T. Foxon. *Quantized conductance of point contacts in a two-dimensional electron gas*. Physical Review Letters **60**, 848–850 (1988).

[94] B. J. van Wees, L. P. Kouwenhoven, H. van Houten, C. W. J. Beenakker, J. E. Mooij, C. T. Foxon, and J. J. Harris. *Quantized conductance of magnetoelectric subbands in ballistic point contacts*. Physical Review B **38**, 3625–3627 (1988).

[95] B. J. van Wees, L. P. Kouwenhoven, E. M. M. Willems, C. J. P. M. Harmans, J. E. Mooij, H. van Houten, C. W. J. Beenakker, J. G. Williamson, and C. T. Foxon. *Quantum ballistic and adiabatic electron transport studied with quantum point contacts*. Physical Review B **43**, 12431–12453 (1991).

[96] H. van Houten, C. Beenakker, and B. van Wees, "Chapter 2: Quantum point contacts," in *Semiconductors and Semimetals* (M. Reed, ed.), vol. 35, ch. 2, 9–112, Elsevier, (1992).

[97] L. P. Kouwenhoven, B. J. van Wees, C. J. P. M. Harmans, J. G. Williamson, H. van Houten, C. W. J. Beenakker, C. T. Foxon, and J. J. Harris. *Nonlinear conductance of quantum point contacts*. Physical Review B **39**, 8040–8043 (1989).

[98] S. Datta. *Electronic transport in mesoscopic systems*. Cambridge Studies in Semiconductor Physics and Microelectronic Engineering, Cambridge University Press, 1995.

[99] D. Widmann, H. Mader, and H. Friedrich. *Technologie hochintegrierter Schaltungen*, vol. 19. Springer Berlin Heidelberg, 2 ed., 1996.

[100] W. Menz and O. Paul. *Mikrosystemtechnik für Ingenieure*. Weinheim: John Wiley & Sons, 1 ed., 1992.

[101] P. Rai-Choudhury. *Handbook of microlithography, micromachining, and microfabrication, volume 2: Micromachining and microfabrication*, vol. PM39. Bellingham, USA: SPIE Press, 1997.

[102] P. Rai-Choudhury. *Handbook of microlithography, micromachining, and microfabrication, volume 1: Microlithography*, vol. PM40. Bellingham, USA: SPIE Press, 1997.

[103] J. Ziegler. *Transport in HgTe-based 2D topological insulators*. Universität Regensburg, Masterarbeit, 2013.

[104] M. Pleyer. *Untersuchung des nasschemischen Ätzprozesses von Nanostrukturen in HgTe*. Universität Regensburg, Bachelorarbeit, 2015.

[105] C. Betthausen. *Spin effects in high- and low-field magnetotransport experiments in semimagnetic $Cd_{1-x}Mn_xTe$ heterostructures*. Universität Regensburg, Dissertation, 2012.

[106] M. Illing, G. Bacher, A. Forchel, A. Waag, T. Litz, and G. Landwehr. *Fabrication and optical characterization of wet chemically etched CdTe/CdMgTe wires*. Journal of Crystal Growth **138**, 638–642 (1994).

[107] J. Dewar. *Liquid atmospheric air*. Proc. R. Inst. Gr. Br. **14**, 1–12 (1893).

[108] J. Dewar. *Scientific uses of liquid air*. Proc. R. Inst. Gr. Br. **15**, 815–829 (1895).

[109] H. Kamerlingh Onnes. *The liquefication of helium*. Proc. Roy. Acad. Sci. Amsterdam **11**, 168–185 (1908).

[110] H. London, G. R. Clarke, and E. Mendoza. *Osmotic pressure of He^3 in liquid He^4, with proposals for a refrigerator to work below 1°k*. Physical Review **128**, 1992–2005 (1962).

[111] P. Das, R. B. de Ouboter, and K. W. Taconis, "A realization of a London-Clarke-Mendoza type refrigerator," in *Low Temperature Physics LT9*, 1253–1255, Springer US, (1965).

[112] H. Kamerlingh Onnes. *The resistance of pure mercury at helium temperatures*. Commun. Phys. Lab. Univ. Leiden **12**, 1 (1911).

[113] C. E. Hunklinger. *Low-Temperature Physics*. Springer-Verlag Berlin Heidelberg, 1 ed., 2005.

[114] F. Pobell. *Matter and methods at low temperatures*. Springer-Verlag Berlin Heidelberg, 3 ed., 2007.

[115] D. J. Cousins, S. N. Fisher, A. M. Guénault, R. P. Haley, I. E. Miller, G. R. Pickett, G. N. Plenderleith, P. Skyba, P. Y. A. Thibault, and M. G. Ward. *An advanced dilution refrigerator designed for the new Lancaster microkelvin facility*. Journal of Low Temperature Physics **114**, 547–570 (1999).

[116] D. Neumaier. *Schwache Lokalisierung und andere Interferenzeffekte in Ferromagneten*. Universität Regensburg, Dissertation, 2009.

[117] C. Albrecht. *Quantenmechanische Transporteffekte in kurzperiodischen lateralen Übergittern*. Max-Planck-Institut für Festkörperforschung, Dissertation, 2000.

[118] R. Fischer. *Magnetocapacitance and transport measurements on HgTe-bassed 2D and 3D topological insulators*. Universität Regensburg, Masterarbeit, 2016.

[119] J. Zhu, C. Lei, and A. H. MacDonald. *Electronic properties of thin films of tensile strained HgTe*. ArXiv e-prints 1804.01662 (2018).

[120] J. G. Checkelsky, L. Li, and N. P. Ong. *Zero-energy state in graphene in a high magnetic field*. Physical Review Letters **100** (2008).

[121] Y. Xu, I. Miotkowski, and Y. P. Chen. *Quantum transport of two-species Dirac fermions in dual-gated three-dimensional topological insulators*. Nature Communications **7**, 11434 (2016).

[122] G. M. Gusev, D. A. Kozlov, A. D. Levin, Z. D. Kvon, N. N. Mikhailov, and S. A. Dvoretsky. *Robust helical edge transport at ν=0 quantum Hall state*. Physical Review B **96**, 045304 (2017).

[123] X. C. Zhang, I. Martin, and H. W. Jiang. *Landau level anticrossing manifestations in the phase-diagram topology of a two-subband system*. Physical Review B **74** (2006).

[124] G. Yu, D. J. Lockwood, A. J. SpringThorpe, and D. G. Austing. *Crossing and anticrossing of spin-split Landau levels in an $Al_xGa_{1-x}As/GaAs$ parabolic quantum well ferromagnet*. Physical Review B **76**, 085331 (2007).

[125] C. A. Duarte, G. M. Gusev, A. A. Quivy, T. E. Lamas, A. K. Bakarov, and J. C. Portal. *Landau-level crossing in two-subband systems in a tilted magnetic field*. Physical Review B **76**, 075346 (2007).

[126] F. Nichele, M. Kjaergaard, H. J. Suominen, R. Skolasinski, M. Wimmer, B.-M. Nguyen, A. A. Kiselev, W. Yi, M. Sokolich, M. J. Manfra, F. Qu, A. J. Beukman, L. P. Kouwenhoven, and C. M. Marcus. *Giant spin-orbit splitting in inverted InAs/GaSb double quantum wells*. Physical Review Letters **118**, 016801 (2017).

[127] G. Timp, P. M. Mankiewich, P. deVegvar, R. Behringer, J. E. Cunningham, R. E. Howard, H. U. Baranger, and J. K. Jain. *Suppression of the Aharonov-Bohm effect in the quantized Hall regime*. Physical Review B **39**, 6227–6230 (1989).

[128] B. J. van Wees, L. P. Kouwenhoven, C. J. P. M. Harmans, J. G. Williamson, C. E. Timmering, M. E. I. Broekaart, C. T. Foxon, and J. J. Harris. *Observation of zero-dimensional states in a one-dimensional electron interferometer.* Physical Review Letters **62**, 2523–2526 (1989).

[129] G. Timp, "Chapter 3: When does a wire become an electron waveguide," in *Semiconductors and Semimetals* (M. Reed, ed.), vol. 35, ch. 3, 113–190, Elsevier, (1992).

[130] S. Essert. *Mesoscopic transport in topological insulator nanostructures.* Universität Regensburg, Dissertation, 2016.

[131] M. Otteneder. *Magnetotransportmessungen an HgTe Quantentrögen.* Universität Regensburg, Bachelorarbeit, 2015.

[132] R. Kozlovsky, C. Gorini, and K. Richter, "Unpublished." (2018).

[133] J.-C. Charlier, X. Blase, and S. Roche. *Electronic and transport properties of nanotubes.* Reviews of Modern Physics **79**, 677–732 (2007).

[134] Ö. Gül, N. Demarina, C. Blömers, T. Rieger, H. Lüth, M. I. Lepsa, D. Grützmacher, and T. Schäpers. *Flux periodic magnetoconductance oscillations in GaAs/InAs core/shell nanowires.* Physical Review B **89**, 045417 (2014).

[135] M. Kessel, J. Hajer, G. Karczewski, C. Schumacher, C. Brüne, H. Buhmann, and L. W. Molenkamp. *CdTe/HgTe core-shell nanowire growth controlled by RHEED.* Physical Review Materials **1**, 023401 (2017).

[136] A. Savitzky and M. J. E. Golay. *Smoothing and differentiation of data by simplified least squares procedures.* Analytical Chemistry **36**, 1627-1639 (1964).

[137] J. Dufouleur, L. Veyrat, A. Teichgräber, S. Neuhaus, C. Nowka, S. Hampel, J. Cayssol, J. Schumann, B. Eichler, O. G. Schmidt, B. Büchner, and R. Giraud. *Quasiballistic transport of Dirac fermions in a Bi_2Se_3 nanowire.* Physical Review Letters **110**, 186806 (2013).

[138] J. Dufouleur, L. Veyrat, B. Dassonneville, E. Xypakis, J. H. Bardarson, C. Nowka, S. Hampel, J. Schumann, B. Eichler, O. G. Schmidt, B. Büchner, and R. Giraud. *Weakly-coupled quasi-1D helical modes in disordered 3D topological insulator quantum wires.* Scientific Reports **7**, 45276 (2017).

[139] E. Xypakis and J. H. Bardarson. *Conductance fluctuations and disorder induced $\nu = 0$ quantum Hall plateau in topological insulator nanowires.* Physical Review B **95**, 035415 (2017).

[140] A. Logg, K.-A. Mardal, G. N. Wells, *et al. Automated solution of differential equations by the finite element method*, vol. 84 of *Lecture Notes in Computational Science and Engineering*. Springer-Verlag Berlin Heidelberg, 2012.

[141] J. Robertson. *High dielectric constant oxides*. European Physical Journal Applied Physics **28**, 265–291 (2004).

[142] V. D. Prozorovskiĭ. *Static dielectric permittivity in gapless solid solutions $Hg_{1-x}Cd_xTe$*. Low Temperature Physics **26**, 853 (2000).

[143] I. Strzalkowski, S. Joshi, and C. R. Crowell. *Dielectric constant and its temperature dependence for GaAs, CdTe, and ZnSe*. Applied Physics Letters **28**, 350 (1976).

[144] S. Luryi. *Quantum capacitance devices*. Applied Physics Letters **52**, 501 (1988).

[145] B. Das and S. Chakrabarty. *Capacitance and charge distribution of two cylindrical conductors of finite length*. IEE Proceedings - Science, Measurement and Technology **144**, 280–286 (1997).

[146] M. Marchewka, J. Grendysa, D. Żak, G. Tomaka, P. Śliż, and E. Sheregii. *Massless Dirac fermions in semimetal HgCdTe*. Solid State Communications **250**, 104–107 (2017).

[147] P. E. Allain and J. N. Fuchs. *Klein tunneling in graphene: optics with massless electrons*. The European Physical Journal B **83**, 301–317 (2011).

[148] B. L. Altshuler and A. Aronov. *Magnetoresistance of thin films and of wires in a longitudinal magnetic field*. JETP Letters **33**, 499–501 (1981).

[149] K. F. Berggren, T. J. Thornton, D. J. Newson, and M. Pepper. *Magnetic depopulation of 1D subbands in a narrow 2D electron gas in a GaAs:AlGaAs heterojunction*. Physical Review Letters **57**, 1769–1772 (1986).

[150] H. van Houten, B. van Wees, J. Mooij, G. Roos, and K.-F. Berggren. *Magnetic depopulation of subbands and universal conductance fluctuations in quasi-one dimensional GaAs/AlGaAs heterostructures*. Superlattices and Microstructures **3**, 497–501 (1987).

[151] C. Blömers, T. Grap, M. I. Lepsa, J. Moers, S. Trellenkamp, D. Grützmacher, H. Lüth, and T. Schäpers. *Hall effect measurements on InAs nanowires*. Applied Physics Letters **101**, 152106 (2012).

[152] K. Storm, F. Halvardsson, M. Heurlin, D. Lindgren, A. Gustafsson, P. M. Wu, B. Monemar, and L. Samuelson. *Spatially resolved Hall effect measurement in a single semiconductor nanowire*. Nature Nanotechnology **7**, 718–722 (2012).

[153] J. P. DeGrave, D. Liang, and S. Jin. *A general method to measure the Hall effect in nanowires: Examples of FeS_2 and MnSi.* Nano Letters **13**, 2704–2709 (2013).

[154] O. Hultin, G. Otnes, L. Samuelson, and K. Storm. *Simplifying nanowire Hall effect characterization by using a three-probe device design.* Nano Letters **17**, 1121–1126 (2017).

[155] M. Wimmer, A. R. Akhmerov, J. P. Dahlhaus, and C. W. J. Beenakker. *Quantum point contact as a probe of a topological superconductor.* New Journal of Physics **13**, 053016 (2011).

[156] M. Kjaergaard, F. Nichele, H. J. Suominen, M. P. Nowak, M. Wimmer, A. R. Akhmerov, J. A. Folk, K. Flensberg, J. Shabani, C. J. Palmstrøm, and C. M. Marcus. *Quantized conductance doubling and hard gap in a two-dimensional semiconductor–superconductor heterostructure.* Nature Communications **7**, 12841 (2016).

[157] L. P. Rokhinson, X. Liu, and J. K. Furdyna. *The fractional a.c. Josephson effect in a semiconductor-superconductor nanowire as a signature of Majorana particles.* Nature Physics **8**, 795–799 (2012).

[158] J. Wiedenmann, E. Bocquillon, R. S. Deacon, S. Hartinger, O. Herrmann, T. M. Klapwijk, L. Maier, C. Ames, C. Brüne, C. Gould, A. Oiwa, K. Ishibashi, S. Tarucha, H. Buhmann, and L. W. Molenkamp. *4π-periodic Josephson supercurrent in HgTe-based topological Josephson junctions.* Nature Communications **7**, 10303 (2016).

[159] E. Bocquillon, R. S. Deacon, J. Wiedenmann, P. Leubner, T. M. Klapwijk, C. Brüne, K. Ishibashi, H. Buhmann, and L. W. Molenkamp. *Gapless Andreev bound states in the quantum spin Hall insulator HgTe.* Nature Nanotechnology **12**, 137–143 (2016).

[160] C. Thomas, O. Crauste, B. Haas, P.-H. Jouneau, C. Bäuerle, L. P. Lévy, E. Orignac, D. Carpentier, P. Ballet, and T. Meunier. *Revealing topological Dirac fermions at the surface of strained HgTe thin films via quantum Hall transport spectroscopy.* Physical Review B **96**, 245420 (2017).

[161] D. Schröer, A. Hüttel, D. Taubert, F. Olbrich, D. Kalok, H. Kraus, A. Dirnaichner, C. Butschkow, S. Geissler, A. Iankilevitsch, and S. Reinhardt, *Lab::Measurement.* www.labmeasurement.de, (2018).

Publication list

2018

Probing spin helical surface states in topological HgTe nanowires.
J. Ziegler, R. Kozlovsky, C. Gorini, M.-H. Liu, S. Weishäupl, H. Maier, R. Fischer, D. A. Kozlov, Z. D. Kvon, N. Mikhailov, S. A. Dvoretsky, K. Richter, and D. Weiss
Physical Review B 97, 035157 (2018).

2017

Ballistic geometric resistance resonances in a single surface of a topological insulator.
H. Maier, J. Ziegler, R. Fischer, D. A. Kozlov, Z. D. Kvon, N. N. Mikhailov, S. A. Dvoretsky, and D. Weiss
Nature Communications 8(1), 2023 (2017).

Photogalvanic probing of helical edge channels in two-dimensional HgTe topological insulators.
K.-M. Dantscher, D. A. Kozlov, M. T. Scherr, S. Gebert, J. Bärenfänger, M. V. Durnev, S. A. Tarasenkko, V. V. Belkov, N. N. Mikhailov, S. A. Dvoretsky, Z. D. Kvon, J. Ziegler, D. Weiss, and S. D. Ganichev
Physical Review B 95, 201103(R) (2017).

Quantum capacitance of a three-dimensional topological insulator based on HgTe.
D. A. Kozlov, D. Bauer, J. Ziegler, R. Fischer, M. L. Savchenko, Z. D. Kvon, N. N. Mikhailov, S. A. Dvoretsky, and D. Weiss
Low Temperature Physics 43, 430-436 (2017).

2016

Capacitance spectroscopy of a system of gapless Dirac Fermions in a HgTe Quantum Well.
D. A. Kozlov, M. L. Savchenko, J. Ziegler, Z. D. Kvon, N. N. Mikhailov, S. A. Dvoretskii, and D. Weiss
JETP Letters 104, 859-863 (2016).

Probing quantum capacitance in a 3D topological insulator.
D. A. Kozlov, D. Bauer, J. Ziegler, R. Fischer, M. L. Savchenko, Z. D. Kvon, N. N. Mikhailov, S. A. Dvoretsky, and D. Weiss
Physical Review Letters 116, 166802 (2016).

Acknowledgement

I would like to thank:

- Prof. Dr. Dieter Weiss for the allowing me to work on this topic, the instruction and supervision of this work, the countless discussions, and all the tips and tricks throughout these years. And for his support, that allowed me to participate at a number of conferences.
- Prof. Dr. Klaus Richter, Dr. Cosimo Gorini and Raphael Kozlovsky for the fruitful collaboration, the band structure calculations, and the countless discussions on the theory of topological nanowires and phase coherent effects. Prof. Dr. Ming-Hao Liu for the electrostatical simulations.
- Dr. Dmitry Kozlov for the many teaching moments on the correct measurement setup and for providing a steady supply of wafer material.
- Dr. J. Dufouleur for the helpful discussions on TI nanowires and fast Fourier transforms.
- Michael Weigl, Dieter Vogel, Alexei Ivankilevitch and Ralf Fischer for keeping the dilution refrigerator alive and well throughout the years.
- All of our technicians, Michael Weigl, Florian Birkner, Uli Gürster, Thomas Haller, and Cornelia Linz, for tips concerning sample fabrication and for keeping systems running.
- Dieter Riedl for his help in building and understanding the filtering equipment.
- The entire *Lab::Measurement* team for their work on the project. Dr. Stefan Geissler, Christian Butschkow, and Dr. Alexei Ivankilevitch for their help in understanding it and getting scripts to run. Christian Butschkow for his help with and previous work on a *MATLAB* framework. Johannes Stigloher for introducing me to *Jupyter* (and *Blender*). Automated measurements and data analysis became so much easier thanks to you all.
- Hubert Maier, Ralf Fischer, David Disterheft, Markus Ehlert, and all the students of the *Topo*-group throughout the years. Especially my Master- and Bachlor-students (Ralf Fischer, Lukas Burggraf, Lukas Epple, and Andreas Haag; Melanie Gottschalk, Max Otteneder and Thomas Huszak). Without all of your work, this wouldn't have been possible.
- Elke Haushalter and Claudia Moser (Rahm) for making everything outside of research run smooth by keeping the bureaucratic jungle far away.

- Tobias Preis and Tobias Völkl for the pleasant atmosphere in our office and the many interesting, and sometimes also funny and ridiculous, discussions.
- And finally, Dima, Tobias, Hannes, Basti, Martin, Ralf, and Hubert for proofreading. I owe you a bunch of commas each.